Design, Optimization and Comparison of Spoke-Type Synchronous Motor and Permanent-Magnet Assisted Synchronous Reluctance Motor in Home Appliance Applications

vorgelegt von
M. Sc.
Shouhui Ni
ORCID: 0000-0002-3453-3388

von der Fakultät IV - Elektrotechnik und Informatik
der Technischen Universität Berlin
zur Erlangung des akademischen Grades

Doktor der Ingenieurwissenschaften
-Dr.-Ing.-

genehmigte Dissertation

Promotionsausschuss:

Vorsitzenderin: Prof. Dr.-Ing. Sibylle Dieckerhoff
Gutachter: Prof. Dr.-Ing. Uwe Schäfer
Gutachter: Prof. Dr.-Ing. Rolf Schuhmann
Gutachter: Prof. Dr.-Ing. Shanming Wang

Tag der wissenschaftlichen Aussprache: 8. November 2021

Berlin 2021

Zusammenfassung

In den letzten Jahren ist ein interessanter Trend beim Design von Motoren mit hohem Wirkungsgrad und geringen Kosten die Entwicklung von Motoren mit geringem Seltenerd-Anteil und solchen ohne Seltenerdmagnete, da diese Materialien hohe Kosten verursachen und die Versorgungskette zeitweise instabil wurde. Zu den potenziellen Kandidaten zur Lösung des Problems zählen geschaltete Reluktanzmotoren, Synchron-Reluktanzmotoren und Synchronmotoren mit innenliegenden Ferritmagneten.

Diese Arbeit beschreibt eine Auslegung auf Basis des letztgenannten Prinzips. Für das Antriebssystem einer Waschmaschinen-Trommel wurden zwei Motortypen ausgewählt und erforscht, nämlich der Speichen-Synchronmotor und der Permanentmagnet-unterstützte Synchron-Reluktanzmotor. Der Speichen-Synchronmotor kann aufgrund der Flusskonzentrationseffekte der Struktur eine höhere Flussdichte im Luftspalt erreichen. Der Permanentmagnet-unterstützte Synchronmotor hat normalerweise eine stärkere magnetische Unsymmetrie, was einen größeren Unterschied zwischen den Induktivitäten in der d- und q-Achsen bewirkt und so zu einem höheren Reluktanz-Drehmoment führt.

Um einen fairen Vergleich der beiden Motortypen durchführen zu können, wurde ein automatisches Optimierungsverfahren ausgewählt, das auf parametrischen Finite-Elemente-Modellen und verschiedenen Optimierungsalgorithmen basiert. Die Bewertung der Systeme basiert auf zwei typischen Betriebspunkten. Einer davon hat ein höheres Drehmoment und eine niedrigere Drehzahl, während der andere ein niedrigeres Drehmoment und eine höhere Drehzahl hat. Randbedingungen wurden durch Hinzufügen von Straffunktionen zur Zielfunktion berücksichtigt, und anhand von unterschiedlichen Strafkoeffizienten priorisiert. Es wurden drei Optimierungsalgorithmen betrachtet: ein genetischer Algorithmus, die Nelder-Mead-methode und die Quasi-Newton-Methode, die jeweils einen stochastischen, einen deterministischen, aber differentialfreien und einen deterministischen Algorithmus unter Nutzung der Differentiale darstellen. Verschiedene Konfigurationen, die durch Kombinieren verschiedener Algorithmen entstehen, wurden getestet und miteinander verglichen. Schließlich wurde die Kombination des genetischen Algorithmus und Nelder-Mead-methode als endgültige Lösung für weitere Analysen ausgewählt.

Basierend auf diesem Optimierungsverfahren wurden sowohl ein Speichen-Synchronmotor als auch ein Permanentmagnet-unterstützter Synchron-Reluktanzmotor berechnet und endgültige Auslegungen für beide durchgeführt. Für die Speichen-

Synchronmotoren wurden verschiedene Rotoranordnungen unter den gegenläufigen Aspekten der mechanischen und der Entmagnetisierungs-Festigkeit bewertet. Berechnungen mit einschichtigen Wicklungen und zweischichtigen Wicklungen zeigen, dass letztere bessere Entmagnetisierungseigenschaften aufweist. Eine Konfiguration mit kürzerer Stator- und längerer Rotor-Blechpaketlänge wurde ebenfalls untersucht. Aufgrund mechanischer Probleme bei hoher Drehzahl, die durch einen größeren Abstand zwischen den beiden Lagern verursacht wurden, wurde diese Struktur bei der endgültigen Konstruktion nicht übernommen. Eine weiteres Design wurde für einen Permanentmagnet-unterstützten Synchron-Reluktanzmotor basierend auf einem analogen Optimierungsprozess erarbeitet. Vor der endgültigen Fertigung wurden die endgültigen Auslegungen nochmals hinsichtlich mechanischer Festigkeit, Entmagnetisierung, Drehmoment und Temperatur überprüft.

Beide Maschinen wurden auf einem Prüfstand untersucht. Es wurden Leerlauf, Kurzschluss und Lastprüfungen sowie je ein Erwärmungslauf durchgeführt. Die Ergebnisse validieren das Optimierungsverfahren und die Simulationen. Auf Basis der Ergebnisse von Experimenten und Simulationen wurde dann eine Zusammenfassung gegeben.

Abstract

In recent years, an interesting trend of the design of electrical motors has been the development of rare-earth-free motors or such of reduced rare-earth content with high efficiency and low cost as rare-earth material usually suffers from high cost and unstable supply. Potential candidates include switched reluctance motors, synchronous reluctance motors and interior permanent magnet synchronous motors with ferrite magnets.

In this thesis, research is focused on interior permanent magnet synchronous motors with ferrite magnets. Two types of motors were selected and designed for application in a drum drive for washing machines: the spoke-type synchronous motor and the permanent-magnet assisted synchronous reluctance motor. The spoke-type synchronous motor can achieve higher flux density in the air gap due to the flux concentrating effects of its structure. The permanent-magnet assisted synchronous reluctance motor usually render a higher saliency ratio, which means larger difference between the inductances in d- and q-axes leading to an increase of reluctance torque.

An automatic optimization procedure based on parametric finite element model and different optimization algorithms was established in order to perform a fair comparison of both types of motors. The evaluations of performance were based on two typical operating points: one with high torque and low speed and the other one with low torque and high speed. Various constraints have been taken into account by adding penalty functions into the objective function, classified into priority levels labeled with different penalty coefficients. Three optimization algorithms have been considered: a genetic algorithm, the Nelder-Mead method and the quasi-Newton method, representing a stochastic algorithm, a non-derivative based deterministic and a deterministic algorithm with derivative information, respectively. Different configurations formed by combining the named algorithms have been tested and compared. Finally, the combination of a genetic algorithm and the Nelder-Mead method was chosen for further analyses.

Based on the optimization procedure, both of spoke-type synchronous motor and permanent-magnet assisted synchronous reluctance motor were laid out, and final designs of them have been achieved. For the spoke-type synchronous motor, different rotor layouts have been discussed in aspects of mechanical strength and resilience against demagnetization. The difference between single- and double-layer windings have also been investigated, including the interesting result that the design with double-layer winding has better performance of anti-demagnetization than that with single-layer

winding. The effect of an extended rotor stack has also been investigated. Considering the further mechanical issues at high speed caused by larger distance between the two bearings, this design has however not been prosecuted in detail. For the permanent magnet-assisted synchronous reluctance motor, the design procedure followed the same optimization process. Before manufacturing, the final designs have been double-checked in aspects of mechanical, anti-demagnetization, torque, and thermal performance.

Finally, a test bench was set up. No load, short-circuit, load, and thermal tests have been carried out for both motors. The results validate the optimization procedure and simulations of this thesis. A summary was then given based on the comparison of the results of experiments and simulations.

Dedicated to my dear parents although they cannot understand English.

Acknowledgements

Table of Contents

List of Figures

List of Tables

Abbreviations

2D	2-dimensional
3D	3-dimensional
AC	alternating current
ADC	analog-to-digital converter
APDL	ANSYS Parametric Design Language
back-EMF	back-electromotive-force
BLAC	brushless alternating current
BLDC	brushless direct current
Conf.	configuration
DC	direct current
DL	double-layer
EMF	electromotive force
EV	electric vehicle
FE	finite element
FEA	finite element analysis
FEM	finite element method
FW	field weakening
GMR	giant magnetoresistance
IPM	interior permanent magnet
MMF	magnetomotive force
MTPA	maximum torque per ampere

Abbreviations

PCB	printed circuit board
PM	permanent magnet
PMASynRM	permanent-magnet assisted synchronous reluctance motor
PMSM	permanent magnet synchronous motor
pu	per unit
RM	synchronous reluctance motor
RMS	root mean square
SL	single-layer
SPM	surface-mounted permanent magnet
SRM	switched reluctance motor

Symbols

Δl	length of end region in both sides
Ψ_{dn}	flux linkage in d-axis at rated currents I_{dn} and I_{qn}
Ψ_d	flux linkage in d-axis
Ψ_p	flux linkage produced by permanent magnet
Ψ_{qn}	flux linkage in q-axis at rated currents I_{dn} and I_{qn}
Ψ_q	flux linkage in q-axis
$\alpha_{SL,m}$	mechanical angle between two sets of single-layer windings
δ_m	modified air gap length
δ_p	thickness of magnets for SPM motors, or 0 for IPM motors
δ	length of air gap
ϵ_i	coefficient of priority of ith constraint
ϵ	coefficient of priority
η_1	efficiency at operating point 1
η_2	efficiency at operating point 2
η_{av}	average efficiency
η_j	efficiency at j^{th} operating point
γ_1	phase angle between q-axis and stator current
λ_1	power factor at operating point 1
λ_2	power factor at operating point 2
λ_j	power factor at j^{th} operating point
λ_{min}	minimum value of power factor
μ_0	vacuum permeability
μ_{rp}	relative permeability of magnets
ν	kinematic viscosity of air
ω_2	electrical angular velocity at operating point 2
ω_j	electrical angular velocity at j^{th} operating point
ω_m	mechanical angular velocity
ω	electrical angular velocity
ρ	density of air

Symbols

$\sigma_{m,s}$	maximum equivalent strength of sth component
$\sigma_{y,s}$	yield strength of sth component
θ_{Es}	angle between $\underline{E}_{AB}$ and $\underline{U}_{sh}$
θ_E	phase angle of the line-to-line no load EMF of A-B $\underline{E}_{AB}$
θ_{IE}	angle between $\underline{I}_A$ and $\underline{E}_{AB}$
θ_{Is}	angle between $\underline{I}_A$ and $\underline{U}_{sh}$
θ_I	phase angle of current of phase A $\underline{I}_A$
θ_{b1}	extremity angle of first layer
θ_{b2}	extremity angle of second layer
θ_s	phase angle of output voltage of angle sensor on channel 1 $\underline{U}_{sh}$
ΔT_1	temperature rise at operating point 1
ΔT_e	temperature rise in thermal test
A_s	surface area of motor
a	number of parallel branches
B_1	flux density at operating point with maximum demagnetization
$B_{m,j,k}$	peak value of AC component of the flux density in k^{th} element in steel sheets
B_r'	new remanence after irreversible demagnetization
B_r	remanence of ferrite magnet
$B_{xy,max}$	maximum value of B_{xy}
B_{xy}	flux density component in the plane of sensor
B_x	flux density component in horizontal axis
B_y	flux density component in vertical axis
$C_{M,j}$	coefficient for friction losses at j^{th} operating point
d_c	diameter of the conductors without insulation
d_p	distance between angle sensor and permanent magnet
$E_{0,-Id}$	no load EMF after applying demagnetizing current $-I_d$
$E_{0,0}$	no load EMF before applying demagnetizing current
$\underline{E}_{AB}$	phasor of line-to-line no load EMF of A-B
$\underline{E}_{AO}$	phasor of no load EMF of phase A
E_d	EMF in d-axis

$E_{m,2D}$	magnetic energy of the model neglecting end effects
$E_{m,3D}$	magnetic energy of the model considering end effects
E_{m1}	magnetic energy in region I
E_{m2}	magnetic energy in region II
E_{m3}	magnetic energy in region III
E_q	EMF in q-axis
$F(x)$	objective function
$F'(x)$	derivative of objective function
$F''(x)$	second derivative of objective function
F_g	geometrical factor
F_p	MMF between rotor stack and stator stack representing the effect of permanent magnet
$f_{cost,b}$	base value of total cost function of material
f_{cost}	total cost of material
f_j	frequency at j^{th} operating point
$f_p(x)$	penalty function
$f_{p,i}$	penalty function for the ith constraint
$g(x)$	constraint function
g_0	base value of $g(x)$
H_1	magnetic field strength at operating point with maximum demagnetization
H_{r1}	magnetic field strength in region I
H_{r2}	magnetic field strength in region II
H_{r3}	magnetic field strength in region III
$\underline{I}_A$	phasor of current of phase A
$I_{RMS,j}$	RMS phase value of stator current
$I_{d,1}$	current in d-axis at operating point 1
$I_{d,2}$	current in d-axis at operating point 2
$I_{d2,1}$	current in d-axis corresponding to $V_{e,min}$ at operating point 2
I_{dn}	rated current in d-axis
I_d	current in d-axis
$I_{q,1}$	current in q-axis at operating point 1
$I_{q,2}$	current in q-axis at operating point 2
$I_{q2,1}$	current in q-axis corresponding to $V_{e,min}$ at operating point 2

Symbols

I_{qn}	rated current in q-axis
I_q	current in q-axis
$I_{s,1}$	RMS value of the stator current at operating point 1
I_s	RMS value of stator current
i	subscript used to represent sequence number of constraints
$J_{s,1}$	current density in stator winding at operating point 1
$J_{s,2}$	current density in stator winding at operating point 1
$J_{s,j}$	current density at the jth operating point in stator windings
$J_{s,max}$	maximum current density value of both operating points
j	subscript used to represent sequence number of operating points, which can be 1 or 2
K_c	eddy-current core losses coefficient
K_e	excess core losses coefficient
K_h	hysteresis core losses coefficient
$k_{SF,s}$	safety factor of sth component
k_{SF}	overall safety factor of a rotor
$k_{d,n}$	suppression factor corresponding to n^{th} space harmonic component
k_δ	Carter's coefficient
$k_{demag,-Id}$	safety factor of motor
k_{end1}	end factor only considering the effects of regions I and II
k_{end}	end factor
k_{error}	error flag representing unexpected errors
$k_{heat,j}$	maximum heat flux at two operating points
$k_{t,1}$	torque ripple coefficient at operating point 1
$k_{t,2}$	torque ripple coefficient at operating point 2
$k_{t,j}$	torque ripple coefficient at j^{th} operating point
$k_{t,max}$	maximum value of the torque ripple coefficients of both operating points
$k_{w,DL,n}$	winding factor for double-layer configuration corresponding to n^{th} space harmonic component

$k_{w,SL,n}$	winding factor for single-layer configuration corresponding to n^{th} space harmonic component
k_{width}	p. u. magnet width
k	subscript used to represent sequence number of elements in steel sheets
L_L	inductance of the adjustable resistors
L_d	inductance in d-axis
L_q	inductance in q-axis
l_e	length of laminated stack
l_{hw}	average depth of all conductors
l_p	length of each ferrite magnet
l_r	length of the rotor stack
l_s	length of stator stack
l_t	model length in tangential direction
l	subscript used to represent sequence number of iteration steps
mI_e	error of measured current
mT_1	error of estimated temperature rise at operating point 1
mT_e	error of measured temperature
m	phase number
N_s	number of turns
Nu	Nusselt number
n_v	dimension of variable vector
n	order of space harmonic components
$P_{Cu,j}$	copper losses at j^{th} operating point
$P_{Fe,j}$	iron losses at j^{th} operating point
$P_{f,j}$	friction losses at j^{th} operating point
$P_{loss,j}$	losses at j^{th} operating point
$P_{o,1}$	output power at operating point 1
$P_{o,2}$	output power at operating point 2
$P_{o,j}$	output power at j^{th} operating point
p_h	number of pole pairs of harmonic components
p	number of pole pairs
R_L	resistance of the adjustable resistors

Symbols

R_s	resistance of one phase of the stator winding
$Re_{\delta,j}$	Reynolds number at j^{th} operating point
r_g	average radius of air gap
r_m	medium radius of air gap
r_r	outer radius of rotor
r_s	outer radius of stator
s	subscript used to represent sequence number of components
$T_{av,j}$	average torque at j^{th} operating point in one electrical period
T_{e0}	measured initial temperature
T_e	measured temperature
$T_{max,j}$	maximum torque at j^{th} operating point in one electrical period
$T_{min,j}$	minimum torque at j^{th} operating point in one electrical period
$T_{o,1}$	output torque at operating point 1
$T_{o,2}$	output torque at operating point 2
Ta_m	modified Taylor number
t_1	equivalent operating period of operating point 1
t_2	equivalent operating period of operating point 2
$\underline{U}_{sh}$	phasor of output voltage of angle sensor on channel 1
$V_{RMS,j}$	RMS phase value of the stator voltage at j^{th} operating point
$V_{d,2}$	stator voltage in d-axis at operating point 2
V_d	voltage in d-axis
$V_{e,min}$	minimum value of V_e
V_e	absolute value of the difference of $V_{s,2}$ and V_{om}
V_{om}	RMS value of maximum allowable stator voltage
$V_{q,2}$	stator voltage in q-axis at operating point 2
V_q	voltage in q-axis
$V_{s,2}$	RMS value of stator phase voltage at operating point 2
V_{trans}	minimum required voltage for given output torque
$w_{in,min}$	minimum width of inner ring

w_{in}	width of inner ring
w_{p0}	base value defined in original rotor
w_{pa}	actual width of a permanent magnet
w_p	width of each ferrite magnet
X_i	parameter in the ith constraint
$X_{max,i}$	upper limit of X_i given in the ith constraint
$X_{min,i}$	lower limit of X_i given in the ith constraint
x_l	value of variables in l^{th} iteration step
x	horizontal axis (abscissa) in Cartesian coordinate system
y	vertical axis (ordinate) in Cartesian coordinate system

1

Introduction

In recent years, the development of electrical motors has shown different interesting trends. One trend is developing high-speed motors, which can be used in various applications, such as compressors, vacuum pumps and machine tools [1–3]. The advantages of high-speed motors are high efficiency, low weight and high power density. A second trend is developing high-efficiency motors to reduce the energy consumption and further to reduce carbon emissions. Potential measures include using die-cast copper in squirrel-cage induction motors [4], replacing squirrel-cage induction motors by permanent magnet (PM) motors such as line-start permanent-magnet motors [5], and by using hairpin windings to reduce ohmic losses in the stator [6]. Another trend is reducing the cost of the motor. A common idea is using permanent magnets with reduced or no expensive rare-earth content [7–10].

This thesis attempts to find a solution for drive systems with requirements of low cost, high efficiency, and wide speed range. Typical applications include home appliance motors for washing machines or air conditioners, in which the cost is important as well as the performance. In this thesis, research is based on a belt drive system for drum drives of washing machines and is mainly focused on design, optimization, test, and comparison of possible candidates.

This chapter first gives an introduction of different drive systems for washing machines. The motivation and the outline of this thesis are presented in the next sections.

1.1 Different Types of Drive Systems in Washing Machines

Practically, washing machines can be divided into two types by the direction of the rotation axis of drum. The first type is called pulsator washing machine, top-load washing machine, or vertical-axis washing machine, as the rotation axis is in vertical

direction [11, 12]. The other type is called roller washing machine, front-load washing machine, or horizontal-axis washing machine, and its rotation axis is in horizontal direction [13, 14]. In general, the top-load type is more traditional, with advantages of being cheaper, smaller, and faster. In the contrary, the front-load type is larger as well as more energy and water efficient.

The drive system for washing machine is a variable-speed drive system with two typical working points in washing cycle and spinning cycle [15]. In washing cycle, high torque and low speed ($30\,\mathrm{min}^{-1}$ to $60\,\mathrm{min}^{-1}$) are required for the drum, while low torque but high speed ($800\,\mathrm{min}^{-1}$ to $1{,}500\,\mathrm{min}^{-1}$) are required [16, 17] in spinning cycle, which is also known as drying cycle.

There are three solutions for the drive system in washing machines: gearbox, belt, and direct drive system, as shown in Figs. 1.1, 1.2, and 1.3 respectively.
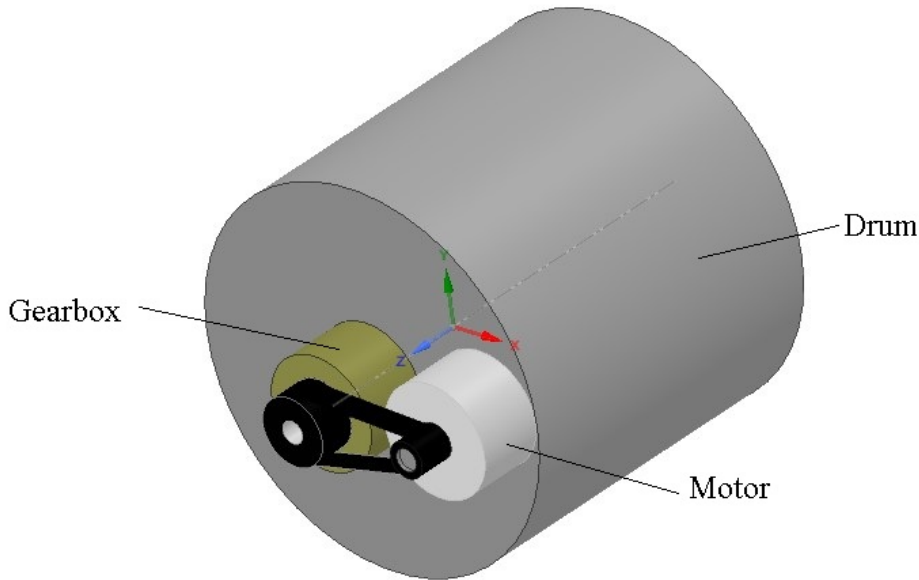
Fig. 1.1   Gearbox drive system.

The gearbox drive system is usually used in traditional top-load washing machines. The motor is coupled to the drum via both belt drive and gearbox with switchable transmission ratio: so a wide speed range of the motor is not required. With the development of speed control systems, the system designers are able to achieve a better control of working cycles to save water [11].

In a belt drive system, the motor is coupled to the drum via a belt drive, so the required torque is reduced, but on the other hand the maximum required speed is greatly increased. With a typical reduction ratio of 10, the maximum required speed can achieve $18{,}000\,\mathrm{min}^{-1}$ to $15{,}000\,\mathrm{min}^{-1}$ [18]. The belt drive washing machine is usually cheaper than direct drive washing machine.

In a direct drive system, the motor is connected to the drum directly, which means a large torque is required, while the maximum speed is low.
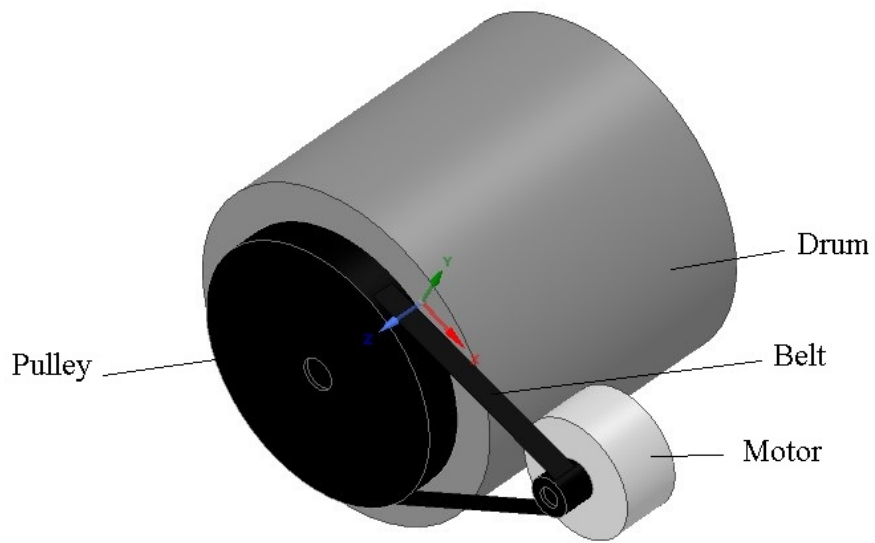
Fig. 1.2 Belt drive system.
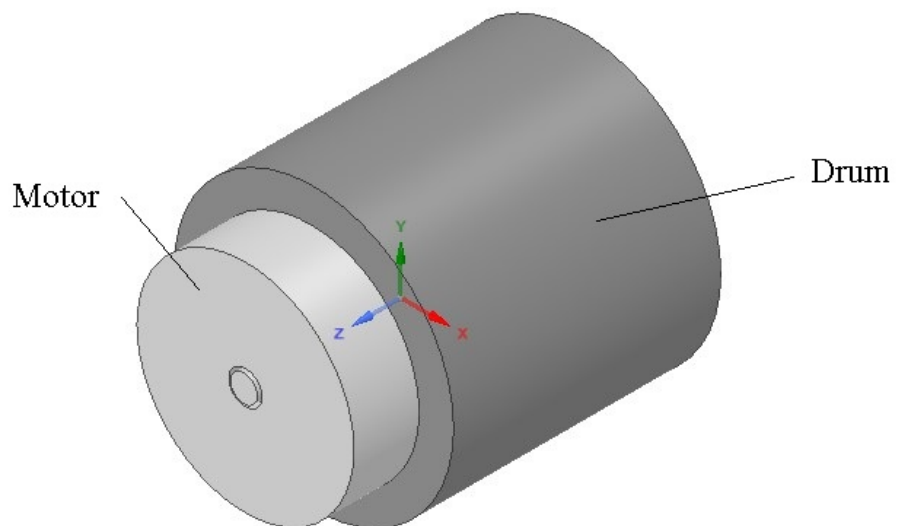
Fig. 1.3 Direct drive system.

The direct drive system is often claimed to be quieter, more efficient, and more reliable than a belt drive system with the absence of gearbox and transmission belt [19–21]. However, there are also different opinions that direct drive is only a strategic choice of the manufacturer: if a belt drive is used, motor and drum can be designed separately, which can be supplied by different companies easily [18]. The cost of a belt drive system is usually lower than the one of a direct drive system, and the maintenance is easier. Nowadays, both belt drive system and direct drive system are used by manufacturers in high-end washing machines. For example, LG uses direct drives while Bosch uses belt drives.

1.2   Motivation

In belt drive washing machine applications, the basic requirements are wide speed range, high efficiency, and low cost. Two types of interior permanent magnet (IPM) motors with ferrite magnets are considered to be capable of meeting these requirements and discussed in this thesis. The aim of the research is to check the feasibility of using them as alternatives to conventional motors in belt drive washing machines.

Automatic optimization with parametric models is necessary in the motor design process. The requirements thereon are flexibility, robustness, and being able to handle constraints with different priorities.

A comparison of the two candidates is also interesting. Special attention should be paid to structural strength at maximum speed and performance concerning irreversible demagnetization when utilizing ferrite magnets.

There are also some further considerations in this thesis: the two types of motors discussed in this thesis are also suitable for some other variable-speed applications, for example domestic applications such as air conditioners and refrigerators, or traction applications such as minimal electric vehicles. This thesis also tries to provide some general understandings of the two motors and some hints for future discussions of the usage of them in these applications.

1.3   Outline of the Thesis

This thesis is organized as follows:

Chapter 1 has just given an introduction of the background and motivation of the study.

Chapter 2 gives a state of the art of the motors used or proposed in washing machines. An overview of the research status of spoke-type motors and permanent-magnet assisted synchronous reluctance motors (PMASynRMs) is then presented.

Chapter 3 establishes parametric finite element (FE) models for the two motors firstly. In order to achieve the optimal design of them, a fitness function as the target function

is defined. A list of constraints with different grades of priorities is considered by using a penalty function. Then an optimization process using a genetic algorithm and the Simplex search method is carried out. Finally, different configurations of optimization processes are compared.

Chapter 4 presents further simulations for spoke-type synchronous motors based on the optimization process from Chapter 3 intended to achieve the final design. Different rotor structures are considered and discussed in aspects of structural strength at high speed, irreversible demagnetization due to stator current, and convenience of manufacturing. A comparison of single- and double-layer windings is also carried out. The effect of using different lengths of stator and rotor stacks is also discussed in one section. Finally, the design of spoke-type synchronous motor is fixed after a double-check of the performance by finite element analysis (FEA).

Chapter 5 presents the design aspects of a permanent-magnet assisted synchronous reluctance motor (PMASynRM) based on the optimization process in Chapter 3. Some modifications are made to the prototype for the convenience of manufacturing. The performance of the final design is also checked by FEA including structural strength at high speed, irreversible demagnetization, achievable torque, and thermal behaviour.

Chapter 6 describes the test bench and presents experimental results. After that, a summary of the results is also provided.

Chapter 7 summarizes the total thesis, and gives suggestions for future work.

<div align="right">

2

</div>

State of the art

This chapter starts with an introduction of different types of motors commonly used in washing machines. The next section presents an introduction of rare-earth-free machines. For the two types of permanent magnet synchronous motors (PMSMs) discussed in this thesis, spoke-type synchronous motor and permanent-magnet assisted synchronous reluctance motor (PMASynRM), the next sections give a review, summarizing research interests and research contributions from other researchers.

2.1   Motors Used or Proposed in Washing Machines

Different types of motors can be used in washing machines, including single-phase induction motors [22, 23], universal motors [24, 25], three-phase induction motors [11, 26, 27], and brushless permanent magnet motors, including brushless direct current (BLDC) motors [28, 29] and permanent magnet synchronous motors (PMSM) [30–32], also named brushless alternating current (BLAC) motors [33]. There are also some other types of motors that have been proposed, such as switched reluctance motors (SRM) [34–36].

2.1.1   Single-phase Induction Motor

Single-phase induction motors are widely used in home appliance applications, with advantages of low cost and simplicity of drive [23, 26]. The main drawbacks are non-adjustable speed and large starting current, so they were used in traditional low-end washing machines [26].

2.1.2   Universal Motor

Universal motor is a series connected commutator motor, which can be fed by alternating current (AC) source [25]. It was used quite commonly in washing machines because of

its simple speed control and wide speed range, but on the other hand suffered from the short lifetime of the brushes [27].

2.1.3 Three-phase Induction Motor

It has already been proved that a three-phase induction motor fed by a frequency converter has much better performance than a single-phase induction motor or a universal motor for washing machines [26, 27]. According to [11], the three-phase induction motor is a good choice for a belt drive system providing simply control and high efficiency in flux weakening mode at high speed.

2.1.4 Brushless Permanent Magnet Motor

Brushless permanent magnet motors include so called brushless direct current (BLDC) motors and permanent magnet synchronous motors (PMSMs). According to [33], theoretically the main difference between BLDC and PMSM is the shape of the back-electromotive-force (back-EMF) waveform, which is trapezoidal in BLDC and sinusoidal in PMSM. Practically, they are however distinguished by the drive method, i.e. current and voltage waveforms rather than by the structures. In this sub-section, both types are discussed without a further distinction.

In direct drive washing machines, surface-mounted permanent magnet (SPM) motors have been widely applied with the benefits of low noise and high efficiency [37–39]. In [36], a collection of figures of such motors manufactured by Samsung, LG, and Whirlpool was given. These motors had similar pancake shapes: external rotor with surface-mounted ferrite magnets, concentrated winding, short stack length, and large radius with a large number of poles. That was caused by the requirement of high torque and the limit of the size between front side and back side in washing machines.

In [31], an SPM Vernier motor with overlapping winding was proposed, in which the power density was increased at the cost of a low power factor. In [15, 30], interior permanent magnet (IPM) motors with rare-earth magnets and inner rotor were proposed in order to increase the power density and make the system more compact.

For interior permanent magnet (IPM) motors with field weakening control, it has already been demonstrated that these have a good performance in variable-speed applications [40]. In [11], an IPM motor was tested and compared with a three-phase induction motor for a belt drive system. The results indicated that both motors met the requirements of the applications, and that the IPM motor solution provided lower starting torque but higher efficiency in washing cycle.

Some special IPM motors also have already been proposed for belt drive washing machines, including permanent-magnet assisted synchronous reluctance motor (PMASynRM) and spoke-type synchronous motor.

As proven in [41], a PMASynRM has a large constant power speed range, which is exactly the requirement in belt drive systems. In [18, 32], a PMASynRM with injection molded plasto-ferrite was developed and compared with a three-phase induction motor, and the result indicated an improvement of efficiency by using PMASynRM.

The spoke-type rotor structure has a flux-concentration effect [42], so the flux density in the air gap can be increased to values above remanence, which is essential when low-cost ferrite magnets are used. With the increase of the capacity of washing machines and higher requirement of power density, the spoke-type synchronous motor with ferrite magnets becomes a promising choice in belt drive systems [43].

2.1.5 Switched Reluctance Motor

According to [36], switched reluctance motors have a simple, low-cost, and robust rotor structure without permanent magnets. Their main shortcomings are high torque ripple and acoustic noise at high speed [44, 45]. Different pancake-shaped switched reluctance motors were developed for direct drive washing machines, with external-rotor [34, 36] or double-stator structures [35]. The results in [36] showed slightly higher efficiency than a conventional surface permanent magnet motor and acceptable torque ripple.

2.1.6 Summary on Different Motors Used or Proposed in Washing Machines

According to the review of motors in washing machines above, a summary can be made as follows:

- Single-phase induction motors and universal motors were widely used in washing machines. However, nowadays they are outdated because of their low reliability, low efficiency, or difficult advanced control.

- In direct drive systems, surface permanent magnet motors with pancake shape and external rotor are widely used. Interior permanent magnet (IPM) motors with rare-earth magnets and inner rotor and switched reluctance motors (SRM) are also proposed for direct drive systems.

- In belt drive washing machines, the three-phase induction motor with a frequency converter has been a widely accepted choice. To further increase the efficiency, potential candidates are different types of IPM motors, including spoke-type synchronous motors and permanent-magnet assisted synchronous reluctance motors (PMASynRM), which will be further discussed in this thesis.

2.2 Rare-earth-free Machines

Among all kinds of motors, induction motors are most commonly used [46]. However, with higher and higher requirements on efficiency, more alternatives have been introduced [47]. Permanent magnet motors are widely discussed, with advantages of high efficiency, high power factor, high power density and high torque density [48–50]. As rare-earth magnets suffer from high price, unstable supply and limited reserves, despite of their excellent performance, researchers are looking for solutions to reduce their usage [51–53]. Solutions that totally avoid rare-earth magnets, also named rare-earth-free motors, have also been introduced in some applications such as electric vehicle (EV) [8–10, 54] and home appliance [55, 56]. In general, potential candidates include switched (SRM) and synchronous reluctance motors (RM) as well as interior permanent magnet (IPM) motors with ferrite magnets [57]. This thesis is mainly focused on IPM motors with ferrite magnets.

When rare-earth magnets are replaced by ferrite magnets, the design needs to be optimized to compensate for the decrease of flux density as the remanence of ferrite magnets is much lower than that of rare-earth magnets [47]. One choice is to use a spoke-type rotor, because the flux-concentration effect of this structure makes it possible to increase the flux density in air gap [42]. Another choice is to get a high saliency ratio, i.e. the quotient of inductances in q- and d-axis, to achieve a high reluctance torque [58]. The rotor of a permanent-magnet assisted synchronous reluctance motor (PMASynRM) is designed to achieve a high saliency ratio [57]. Both choices, spoke-type synchronous motor and PMASynRM, will be further discussed in this thesis.

2.3 Spoke-type Machines

2.3.1 Development of Spoke-type Motors

According to accessible literature in IEEE Xplore, the earliest references that used the term of "spoke-type" to describe the rotor structure with tangentially magnetized permanent magnets can be found no later than 1994 [59], and actually this type of rotor structure can be found even earlier [60]. In recent years, electric machines with spoke-type permanent magnet layout are drawing more and more attention for its efficient utilization of permanent magnet material in lots of applications, e.g. EV traction [61], electric power steering [62], water pump [63], and home appliance applications [43]. According to the comparison among spoke-type, tangential-type, U-shape, and V-shape layouts in [64], where rare-earth magnets were used, the latter has the best overall performance, while spoke-type layout has a worse low-speed performance but the best flux-weakening at high speed. There has also been other research showing the benefits

of spoke-type layout with ferrite magnets, with competitive performance and lower cost compared to commercial interior permanent-magnet synchronous motors [65, 66].

Based on the typical layout of spoke-type structure as shown in Fig. 2.1, the researchers have developed some novel structures. As the rotor poles are split into separate parts in Fig. 2.1, one basic consideration is to ensure the mechanical reliability especially when a high operating speed is required. In [67], a dovetail structure was used to connect the rotor pole and the support, so the maximum stress at high speed is obviously limited. Another solution is to keep the rotor stack as a single piece, by keeping an inner ring in the rotor lamination and using ribs to connect the inner ring and rotor poles [63].
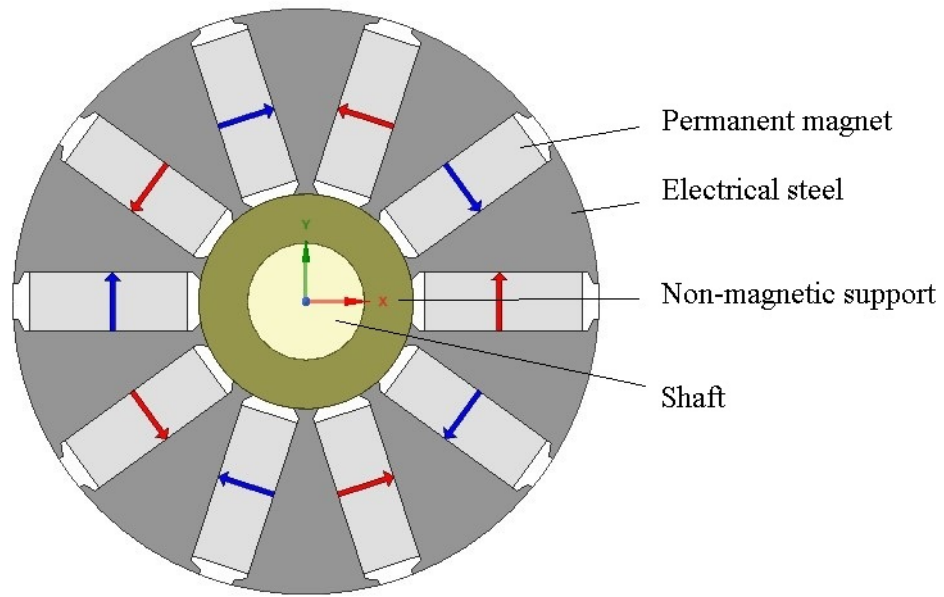
Fig. 2.1 Typical layout of a spoke-type rotor.

A second consideration is to increase torque density by using new structures as presented in Fig. 2.2. Several measures were used to reduce the flux leakage based on single-piece topology, such as using an alternate-rib structure [62], adding additional flux barriers between the ribs and the poles [43], or using a fir-tree structure in the rotor [68]. Some studies introduced tangential flux barriers in rotor poles to increase the saliency ratio and eventually enhance the torque density [69, 70]. To increase the flux density in air gap, some other novel structures were also proposed. In [71], a magnet ring was placed between rotor stack and shaft to strengthen the flux-concentration effect. In [72], a novel wing-shaped layout of ferrite magnets was developed to fix more magnets in the rotor and achieve higher flux density in air gap. To achieve advantages from both ferrite magnets and rare-earth magnets, a hybrid spoke-type structure with both ferrite magnets and rare-earth magnets was investigated [73].

There were also other considerations to develop new rotor layouts as shown in Fig. 2.3. Auxiliary salient poles were introduced in spoke-type rotors to reduce the
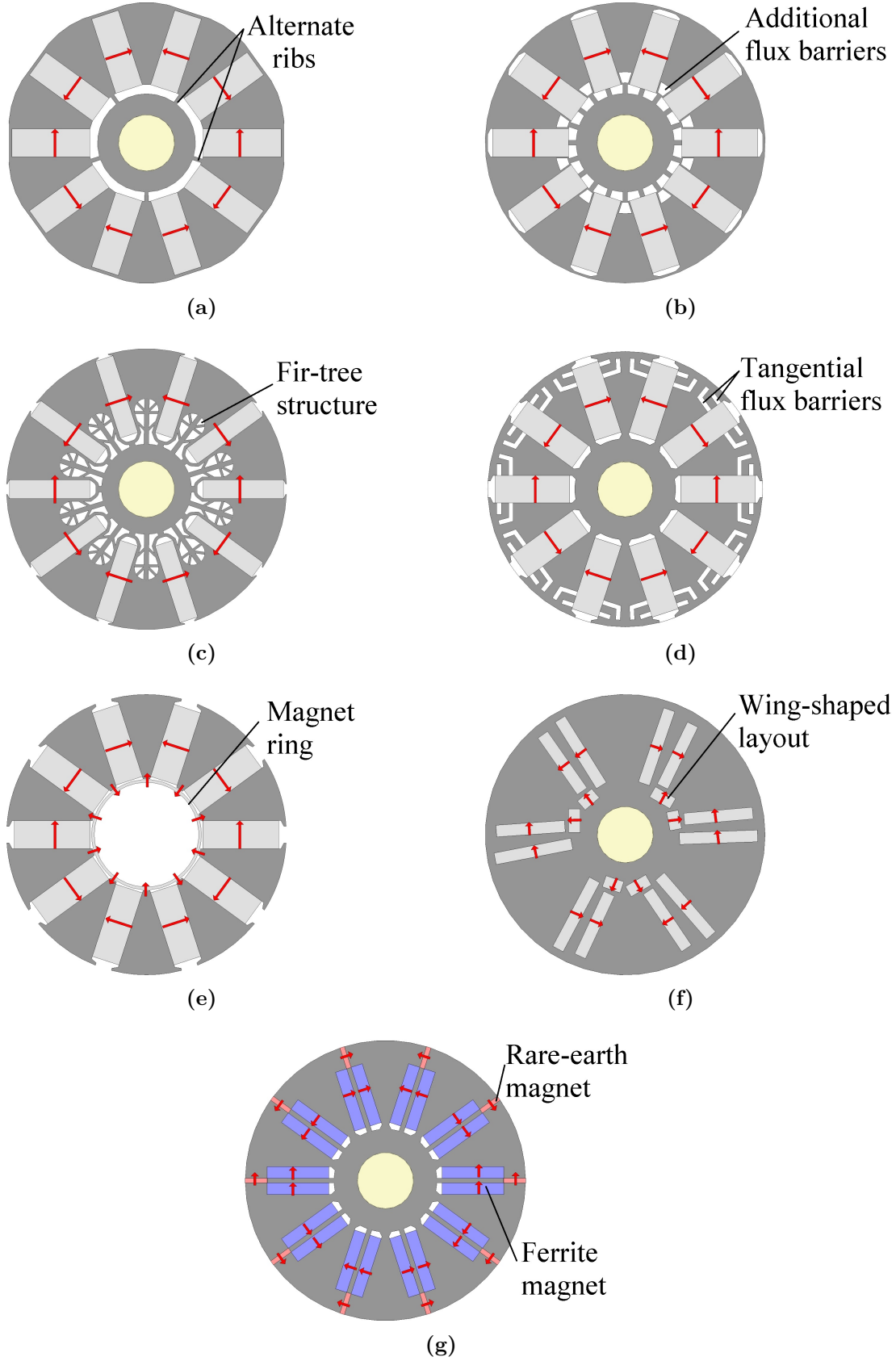
Fig. 2.2 Different rotor layouts proposed to increase torque density. (a) Layout with alternate ribs [62]. (b) Usage of additional flux barriers [43]. (c) Fir-tree structure [68]. (d) Layout with tangential flux barriers [69, 70]. (e) Usage of a magnet ring [71]. (f) Wing-shaped magnets layout [72]. (g) Hybrid structure with both ferrite and rare-earth magnets [73].

torque ripple [74]. Increasing field-weakening capacity was another reason for looking for new structures. A novel structure was presented that a mobile inner ring was coupled to rotor poles via springs which worked as mobile rotor yoke only at high speed [75]. In [76], each permanent magnet was split into two pieces and placed at both sides of the iron pole at q-axis, which resulted in enhanced field-weakening performance at the cost of slightly lower efficiency compared to conventional spoke-type layout.

(a)

(b)

(c)
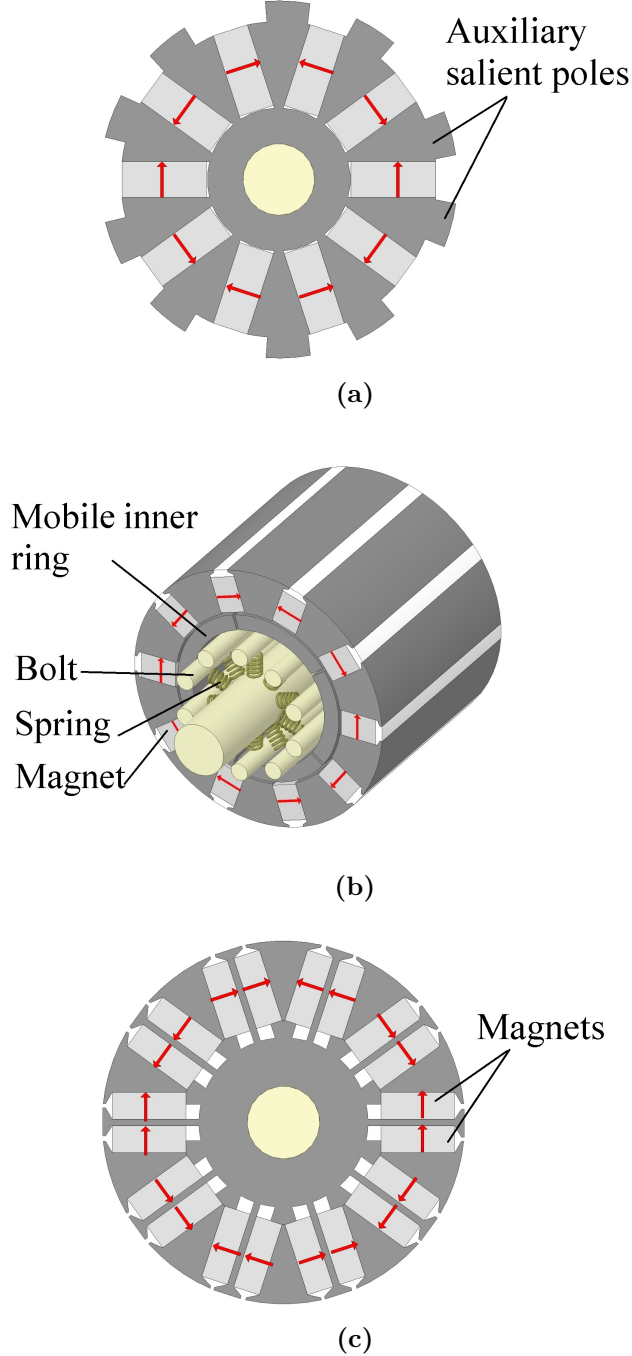
Fig. 2.3 New rotor layouts. (a) Layout with auxiliary salient poles [74]. (b) Usage of a mobile inner ring [75]. (c) Improved design with enhanced field-weakening performance [76].

2.3.2 Analytical Model of Spoke-type Motors

In order to get better understanding of the field distribution and performance of the motor and make the calculation process faster, the analytical method is still interesting for the researchers despite of the finite element (FE) technologies. Analytical models of spoke-type motor were used by using subdomain method based on Poisson's and Laplace's equations [77, 78]. A lumped parameter magnetic circuit model was also presented in [79]. Both methods can take nonlinearity of material into consideration. These studies were based on analysis of 2-dimensional (2D) models to avoid the large computation cost of 3-dimensional (3D) models, but on the other hand it is necessary to calculate end effects. In [80], the analytical relationship between back-EMF and stack length was derived. The overhang effect caused by the different lengths of permanent magnets and rotor stack was also calculated [81].

2.3.3 Optimal Design of Spoke-type Motors

To meet the requirements in different applications or to compare between various topologies, the optimal design of motors is always an interesting topic, including single- [82–85] and multi-objective optimization [86–88] with potential objectives of maximum torque density, minimum cogging torque, losses, material cost or vibration. When an analytical model is used with analytical expressions of objective function, the optimization process becomes time efficient at the cost of a decrease of precision compared to the one with an FE model [82]. When the finite element method (FEM) is used, a response surface method is often utilized to fit the results of a limited number of designs into analytical expressions [83, 84, 86–88]. The design of experiments method was selected to perform the sensitivity study of variables on objectives and form the data base for the response surface method [84, 86, 87]. Other algorithms such as differential evolution algorithm and genetic algorithm have also been proposed [85, 87], which can operate with or without analytical expressions.

Instead of executing a systematic optimization process with mathematical tools, some research was focused on optimal design in some specific topics, such as the selection of material, the shape of permanent magnets, and slot-pole combinations. In [89], the effect of utilizing different types of permanent magnets in a spoke-type motor, including conventional NdFeB magnets, different types of Dy-free NdFeB magnets, and ferrite magnets was investigated, and finally ferrite magnets were chosen. With the aim to reduce the cost of material, other cheaper grades of material, including aluminium winding, recycled NdFeB and Alnico magnets were also considered in spoke-type motors [90, 91]. The study presented in [92] was focused on the selection of rotor support material under consideration of structure strength, magnetic performance, thermal behaviour and cost of rotor. In [93], the effect of different magnet shapes, including rectangular, trapezoidal, and inverted trapezoidal magnets in spoke-type motors was investigated and the results

showed that each configuration has advantages in specific applications. A conclusion was made that 12-slot/14-pole combination has the best overall performance, after the discussion of different slot-pole combinations in spoke-type synchronous motors with fractional-slot concentrated winding [94].

2.3.4 Further Research Interests in Spoke-type Machines

In addition to the work introduced above, more contributions have been made for spoke-type motors. Copper losses with different specifications of stator windings were calculated considering skin and proximity effects [95]. Iron losses were calculated by using the Bertotti model [96]. In [97], the performance of a motor with stepped skewed rotor was investigated. Motors for EV applications must be investigated under highly saturated conditions as a high transient torque was required [98]. The inductance of a spoke-type motor with respect to the current magnitude and the current phase angle was discussed, and the influence on motor control at maximum torque per ampere (MTPA) and field weakening (FW) modes was also analyzed [99]. The high frequency response of the motor was investigated based on sensorless control with high frequency injection method [100]. Motors with multi-phases are also interesting for researchers. A 9-phase spoke-type motor for EV applications was developed, and the results showed that the problem of local saturation was overcome, and the rotor losses were reduced [101].

Apart from conventional motors, the spoke-type permanent magnet layout has been used in some unconventional types of motors to take advantage of its flux-concentration effect. In order to achieve higher torque density, this layout can be utilized in axial-flux motors [102–104] and Vernier motors [105–107]. In magnetic gears, spoke-type rotors were also used for the same reason [108–110]. A linear machine was designed for linear direct drive systems with higher force density and power factor [111]. In [112] and [113], spoke-type arrangement was used in motor with external-rotor and dual-stator structures, respectively.

2.4 Permanent-magnet Assisted Synchronous Reluctance Motors

2.4.1 Development of Permanent-magnet Assisted Synchronous Reluctance Motors

Conventional interior permanent-magnet synchronous motors (IPMSMs) have high efficiency and torque density [40]. With flux-weakening technique, constant-power operation can be achieved [40]. However, there are still some problems with conventional IPMSMs at high speed. A large demagnetizing current is required, which can lead to high copper losses even when the output torque is low [114]. At no load, the electromotive

force (EMF) induced by permanent magnets can be very high at high speed, which can reduce the reliability of the system [115]. To solve these problems, one choice is to use synchronous reluctance motors as there are no permanent magnets in the rotor. The problem of this motor is that its power factor is quite low, which means a larger inverter is required, and the copper losses increase [116].

When high torque density and a wide constant power speed range are required, the optimal solution is to use an IPMSM with high saliency ratio and proper amount of permanent magnets. Then this kind of motor can be also regarded as a synchronous reluctance motor with additional permanent magnets [117]. In [118], a permanent-magnet assisted synchronous reluctance motor (PMASynRM) with an axially laminated rotor stack was introduced, which was named "axially-laminated interior permanent magnet motor", in which a high saliency ratio was achieved by utilizing the anisotropy of steel sheets. The name of "permanent magnet assisted synchronous reluctance motor" as well as the abbreviation "PMASynRM" can be found in [119] published in 1999, and meanwhile a transversally laminated design with multi-layer flux barriers was introduced. Both of the name and the structure were soon widely accepted by other researchers [114, 120, 121]. Nowadays, PMASynRM has been widely considered in applications where low cost or a wide constant power speed range is required, such as ventilation [122], washing machine [18, 32, 53, 55], and EV traction including automotive [123–125], electric powertrain [126], and light traction [127].

Several studies have compared PMASynRM and other motors, and the results showed the advantages of PMASynRM in variable-speed applications, which can be concluded as follows:

- Compared to a synchronous reluctance motor, the torque of PMASynRM increases slightly at low speed by adding permanent magnets in the rotor and significantly in field weakening operation. The power factor in the whole operating range is improved [128].

- Compared to a conventional IPMSM, the constant power speed range of a PMASynRM can be increased with proper amount of permanent magnet material [129]. By replacing rare-earth magnets with ferrite magnets, the cost can also be slashed [130].

- A surface-mounted permanent magnet (SPM) motor has a poor field weakening performance compared to a PMASynRM [49].

- An induction motor has a similar overload curve as a PMASynRM, but its efficiency is lower than that of a PMASynRM due to the copper loss in the rotor [49].

As mentioned above, there were two kinds of rotor structures when this kind of motor was invented: those with so-called "axially laminated rotor stacks" [118] and

those with so-called "transversally laminated rotor stacks" and multi-layer flux barriers [131]. Both structures are illustrated in Fig. 2.4. As summarized in [131], an axially laminated rotor has a high saliency ratio, but suffers from high iron losses at high speed. Its manufacturing is more difficult than the one of the other kind of rotor due to the unconventional axially laminated structure. As a result, the structure with multi-layer flux barriers has nowadays become the most common one. A typical layout is shown in Fig. 2.5.
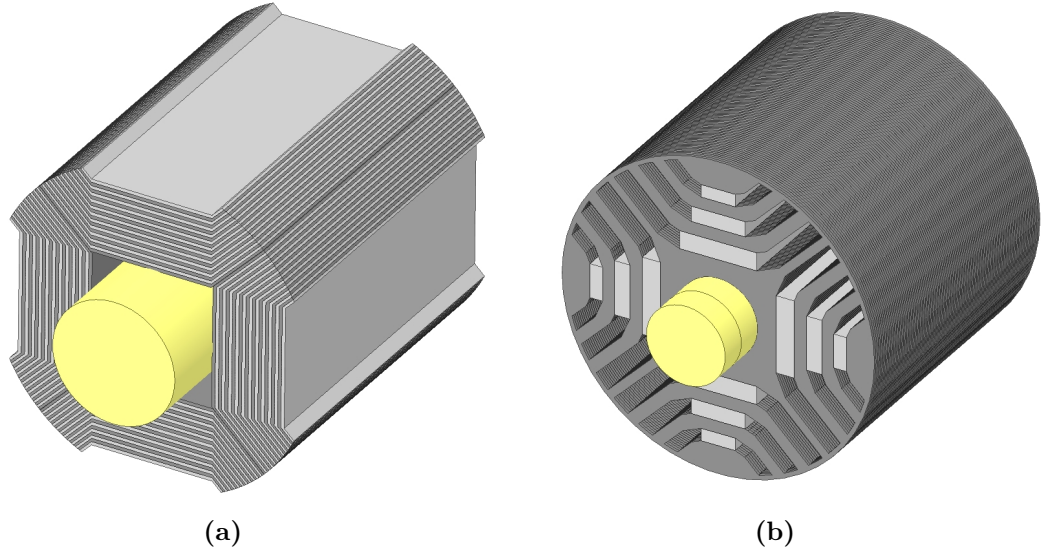
Fig. 2.4 Two kinds of rotor structures of PMASynRMs. (a) So-called "axially laminated rotor stack" [118]. (b) Rotor stack with multi-layer flux barriers.
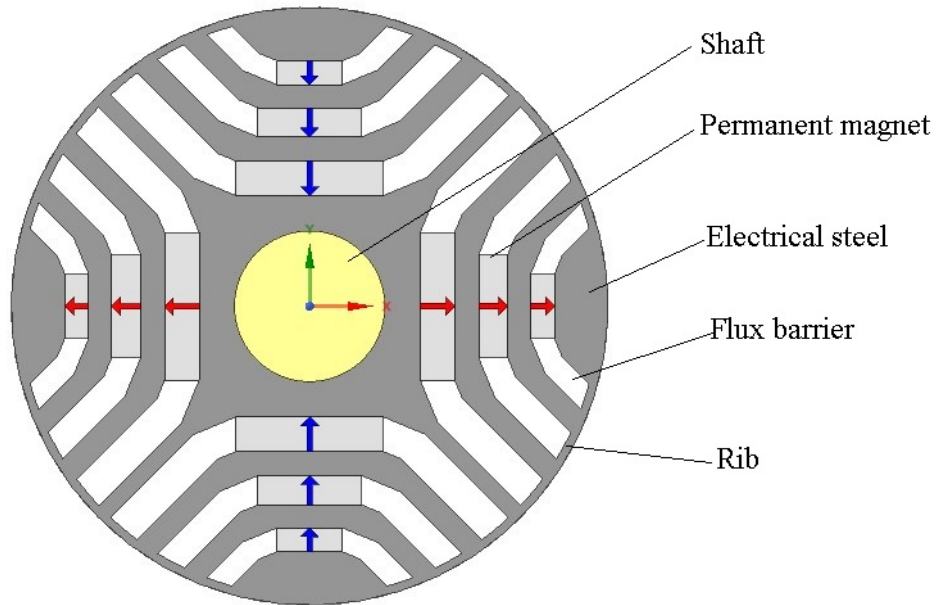
Fig. 2.5 Typical layout of PMASynRM rotor with multi-layer flux barriers.

Based on the layout in Fig. 2.5, some new layouts have been proposed as shown in Fig. 2.6. By introducing a cut-off structure in the rotor stack, uneven air gap and higher saliency ratio can been obtained, leading to enhancement of output torque and reduction of torque ripple [132]. A novel rotor with tuning-fork flux barrier and asymmetric rotor structure was proposed with the aim to decrease the flux leakage and improve the output torque [133]. In [134], another structure was proposed to increase output torque and power factor, which consisted of two segments in axial direction, one of which was a synchronous reluctance rotor without permanent magnets and the other one was an SPM rotor.
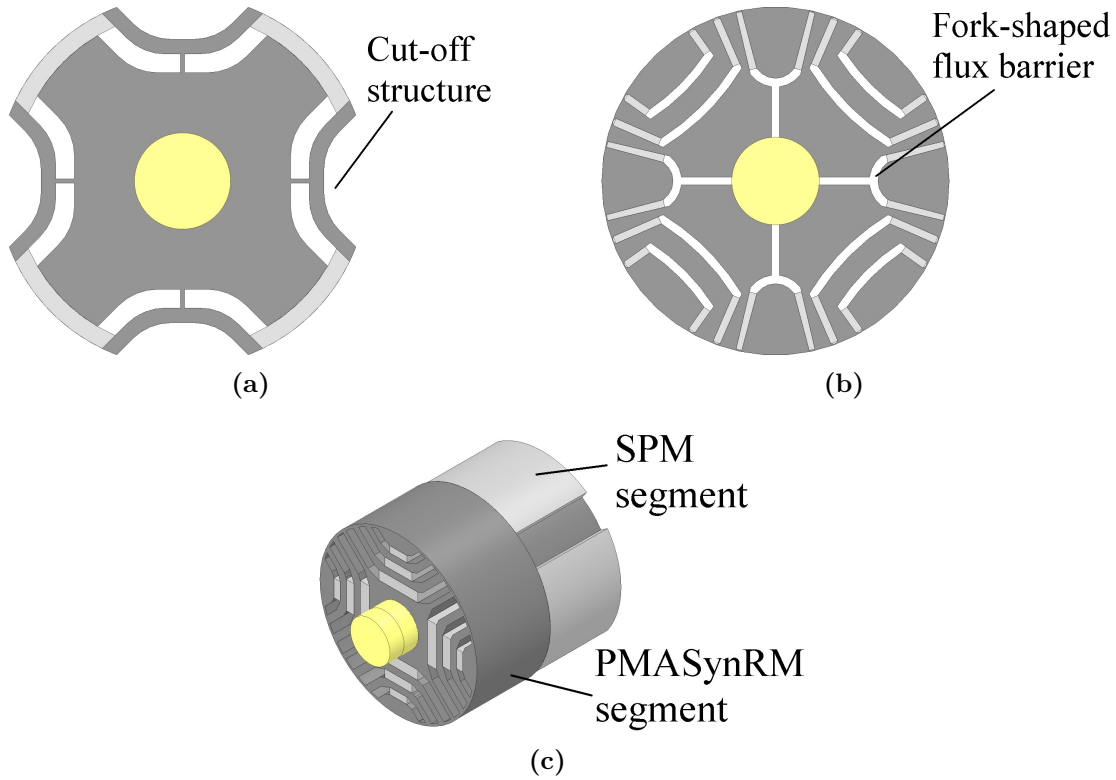
Fig. 2.6 New rotor layouts. (a) Rotor with a cut-off structure [132]. (b) Rotor with tuning-fork flux barriers [133]. (c) Combination of two segments in axial direction [134].

2.4.2 Analytical Model of Permanent-magnet Assisted Synchronous Reluctance Motors

Due to the complex boundary conditions, solving Poisson's and Laplace's equations for rotors of permanent-magnet assisted synchronous reluctance motors (PMASynRMs) becomes difficult, which is rather different from spoke-type rotor. As a result, the lumped parameter magnetic circuit model becomes the most common choice when an analytical model is required [52, 135–137]. It should be noted that the rib areas are highly saturated, which should be specially dealt with in this kind of model. One choice is to regard each rib as a magnetomotive force (MMF) source in series with an equivalent

reluctance [52]. Another choice is to regard it as an equivalent negative flux source, and finally the effect can be considered by modifying the equivalent permanent magnet width [135, 136]. Both solutions were developed under the assumption that the ribs were highly saturated, and the flux density in the ribs was kept constant.

Apart from the lumped parameter magnetic circuit model, there is another simplified analytical model for PMASynRMs by only modeling the distribution of flux density in air gap. In this model, the stator and rotor can be simplified to two MMF sources with harmonic components [138, 139]. Both average torque and torque ripple can be calculated by using this model.

2.4.3 Optimal Design of Permanent-magnet Assisted Synchronous Reluctance Motors

Similar to the spoke-type motor, large efforts have been made towards a systematic optimization of permanent-magnet assisted synchronous reluctance motors (PMASynRMs) by combination of a motor model and mathematical algorithms, the objectives of which include maximum torque and power factor, minimum losses and torque ripple [126, 139–144]. Both analytical [139, 140] and FE models [126, 141–144] have been used, the former being more time efficient and the latter being more precise. The used optimization algorithms included the differential evolution [126, 140, 141, 143], the genetic algorithm [142, 144] and the particle swarm optimization [139]. In some cases, the optimization must be carried out considering different operating points. One example is that an optimization process for EV applications sometimes needs to be carried out along given driving cycles [142], which means a huge number of operating points needs to be taken into consideration. To reduce computation cost, the speed-torque plane was divided into different regions in [143], and an average operating point and a weighting factor were calculated for each region.

Other studies did not utilize complex mathematical algorithms, which were usually focused on a certain topic. When making optimal design of PMASynRMs, the reduction of torque ripple has been one of the most important topics as high torque ripple is a critical shortcoming of this kind of motor. Low torque ripple was achieved by optimal design of width of the permanent magnets and extremity angle of the flux barriers [145]. The definition of the extremity angle is illustrated in Fig. 2.7. Different flux barriers can be used in one motor to reduce torque ripple: Two different laminates with different flux barriers can be utilized to form a stepped skewed rotor stack [146]; Another choice is to use an asymmetric rotor, with two different kinds of flux barriers in the same laminate [138]. To make the rotor be able to skewed continuously, flux barriers were filled with plasto-ferrite by injection molding [32].

Another important topic is the selection of the number of poles and slots. Research in [147] was focused on integer-slot windings (36-slot/4-pole, 36-slot/6-pole, and 48-
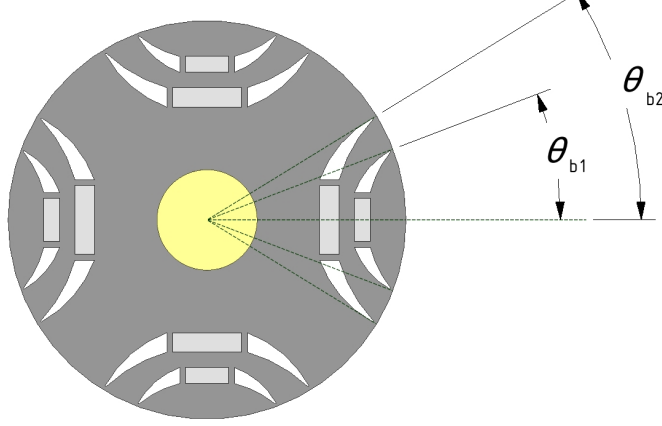
Fig. 2.7 Definition of extremity angle: θ_{b1} and θ_{b2} correspond to first and second layer, respectively [145].

slot/8-pole), and the conclusion was that a 4-pole configuration was suitable for high speed operation and 6-pole configuration for high torque operation. Configurations with 10 poles and different number of slots (12 slots, 24 slots, and 90 slots) were discussed, and finally the 24-slot/10-pole combination was proposed [148]. Some of the most popular fractional-slot-concentrated-winding configurations, including 12-slot/10-pole, 12-slot/8-pole, and 18-slot/8-pole configurations were investigated with the conclusion that the 18-slot/8-pole configuration has the best overall performance [149].

Other topics include achieving high output torque and constant power speed range. To achieve maximum low-speed torque with high power factor, the study in [150] was focused on the selection of permanent magnet flux linkage. In [151], the relationships between constant power speed range, no load EMF, saliency ratio, and rated current were evaluated, and guidelines for the tradeoff between constant power speed range, no load EMF, and rated current were given by analytical formulas.

2.4.4 Further Research Interests on Permanent-magnet Assisted Synchronous Reluctance Motors

In general, other research topics on permanent-magnet assisted synchronous reluctance motors (PMASynRMs) mainly include performance calculation, motor control, and design of new structures.

A PMASynRM with 9 slot/8-pole configuration was designed for washing machine applications [53]. Its performance was analyzed including torque-speed curve, direct current (DC) voltage-speed curve, torque ripple, iron losses, and copper losses as well as skin and proximity effects. In [152], a thermal model by combining a lumped parameter model and finite element analysis (FEA) was given based on a PMASynRM equipped with a housing water jacket, which was designed for hybrid electric vehicle applications. Thermal effects of different material usage and current eddy losses in the rotor were also investigated.

Compared to conventional interior permanent magnet (IPM) motors, PMASynRMs have higher saliency ratio and lower permanent magnet flux. Moreover, the relationship between flux and stator current becomes more complex as there are more ribs or bridges in a PMASynRM rotor as in a conventional IPM rotor [41]. These differences make special research on control of PMASynRMs necessary. According to [153], maximum torque per ampere operation can be achieved by adding small perturbations to the stator current vector and selecting the one producing the highest torque in each tuning step. In [154], a direct flux vector control based on a predictive flux and current observer was developed for a PMASynRM drive system. Some other studies were focused on sensorless control, intended to achieve a system with lower cost and higher reliability. A sensorless flux-oriented control of a PMASynRM for washing machine applications was developed in [155] based on a sliding mode position observer, in which both maximum torque per ampere and field weakening strategies were considered. A sensorless direct torque and flux control of a PMASynRM for an integrated starter-alternator in mild hybrid electric vehicles was presented in [156] by using a position observer with signal injection at low speed and position and a speed observer from stator flux estimation at higher speed. Research in [157] was focused on the impact of the cross-saturation effect on sensorless control of a PMASynRM based on signal injection. A sensorless control solution was developed for a PMASynRM in plug-in hybrid electric vehicle applications [158]. The effects of nonlinear performance on sensorless control, including saturation, cross-saturation, and harmonics of the inductance as well as solutions were also investigated.

Some unconventional PMASynRMs were also proposed for different purposes. A novel dual mechanical port machine with PMASynRM rotor was developed for HEV drive applications to eliminate the gearbox [159]. In order to provide a candidate in safety-critical applications, a 9-phase fault-tolerant PMASynRM with triple redundancy was designed and analyzed [160]. A 5-phase PMASynRM as an integrated starter-alternator was proposed in [161] with the advantages of high reliability and low torque ripple.

3

Optimization Process and Analysis

An automatic optimization procedure is useful when making designs of various types of motors. In order to obtain a basic design of each motor for further research, this procedure can avoid lots of manual work of adjusting different parameters, especially when a list of constraints needs to be considered. For a fair comparison of different motors, it is necessary to carry out the optimization process with the same requirements.

This chapter aims to form a flexible and reliable optimization process with given requirements and a parametric model for each kind of motor. The first section gives a description of parametric FE models for both motors. The next section selects two typical operating points to represent two operating modes respectively, and then describes the calculation process of them. The basic elements of a systematic optimization process, including variables, constraints, and objective function, are presented and explained in the following section. The next two sections provide details of several optimization algorithms and combinations of them, based on which the complete optimization process is formed. The final section gives a comparison of different configurations.

3.1 Parametric Model

The first step of establishing an optimization process is setting up parametric models. Although there are some techniques to obtain analytical models of spoke-type motors and permanent-magnet assisted synchronous reluctance motors (PMASynRMs) as mentioned in Sections 2.3.2 and 2.4.2, they are not used due to following considerations:

- The first one is that the existence of bridges or ribs in some structures makes the nonlinear behavior of these parts more significant.

- The second one is that torque ripple is an important criterion in the optimization, which is difficult to be calculated with high precision by analytical methods.

- The last one is that it is not easy to obtain solutions with high precision. Some structures are so complex that they are difficult to be modeled by using subdomain method. The lumped parameter magnetic circuit method can be one choice, but its precision depends on the topology of the magnetic circuit and the accuracy of the parameters. When there are many constraints in the optimization process, the problem of lacking precision can become critical as a so-called 'optimal design' with low precision can be actually one that cannot satisfy given requirements.

As a result, FE models instead of analytical models are used in this chapter despite large computation cost.

In this chapter, parametric models are built up by using ANSYS Parametric Design Language (APDL). In these models, all values are given in form of variables, constants, and expressions using them. The values of variables and constants can be read from another separate assignment file. By editing this assignment file, values of variables and constants can be transferred from optimization loops to parametric models.

Examples of 2D FE models of spoke-type motors and PMASynRMs are presented in Fig. 3.1. However, a new FE model must be constructed when there are changes in structure.

<table>
<tr><td>(a)</td><td>(b)</td></tr>
<tr><td>(c)</td><td>(d)</td></tr>
</table>
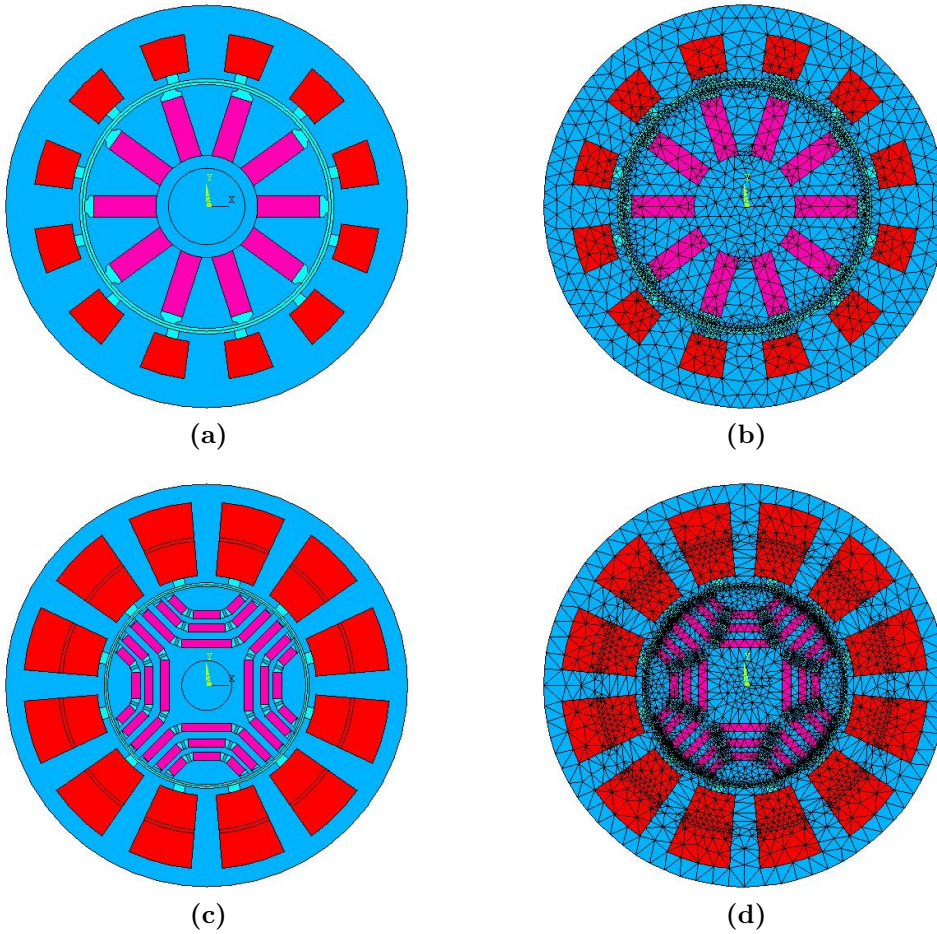
Fig. 3.1 FE models. (a) A spoke-type motor without meshing. (b) A spoke-type motor with meshing. (c) A PMASynRM without meshing. (d) A PMASynRM with meshing.

3.2   Calculation of Operating Points

3.2.1   Operating Points

There are two operating cycles for drive system in washing machine: washing cycle and spinning cycle. For each of them, a typical operating point is selected. The first one is with low speed and high torque, and control strategy of maximum torque per ampere (MTPA) is used. The second one is with high speed and low torque, and control strategy of field weakening (FW) is used. The details are listed in Table 3.1.

Table 3.1   Details of two operating points

Operating points	1	2
Operating mode	Washing	Spinning
Rotation speed/min^{-1}	550	16,600
Torque/(N·m)	1.3	0.3
Control strategy	MTPA	FW
Maximum line-to-line voltage/V	——	230

3.2.2   Definition of d- and q-Axis and Positive Direction

Before further calculation, it is necessary to clarify the definition of d- and q-axis and positive direction to avoid confusion in axis and sign of terms in equations.

In a spoke-type synchronous motor, the definition of d- and q-axis is similar to the one in a conventional interior permanent-magnet synchronous motor (IPMSM), where the d-axis is defined as the midline of north pole of the rotor. When it comes to permanent-magnet assisted synchronous reluctance motors (PMASynRM), there are however two different conventions:

- The first one is to regard a PMASynRM as a conventional IPMSM.

- The second one is to regard a PMASynRM as a synchronous reluctance motor (RM), where the d-axis is defined as the midline of iron pole with ambiguous allocation of the q-axis to north or south pole of the magnet.

The relationship of the two definitions is that the d-axis in the first system corresponds to q- or minus q-axis in the second one.

In this thesis, the first convention is used for PMASynRM to keep consistent with the one of spoke-type synchronous motor. The illustrations showing the definition of d- and q-axis in both motors are given in Fig. 3.2.
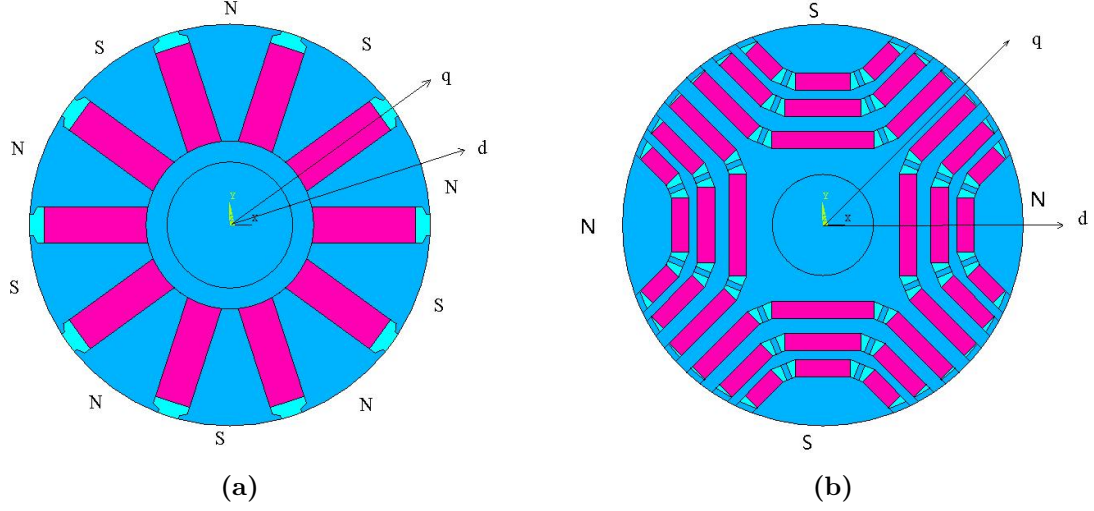
Fig. 3.2 Definition of d- and q-axis. (a) In a spoke-type synchronous motor. (b) In a permanent-magnet assisted synchronous reluctance motor.

When defining positive direction, the load convention is chosen. Voltages in d- and q-axis can be expressed as:

$$
\begin{cases}
V_d = I_d \cdot R_s + E_d \\
V_q = I_q \cdot R_s + E_q
\end{cases}
\tag{3.1}
$$

where V_d and V_q are voltages in d- and q-axis, I_d and I_q are corresponding currents, E_d and E_q are corresponding EMFs of stator winding, and R_s is resistance of one phase of the stator winding.

The positive direction of flux linkage is defined as the direction from rotor to stator. The positive direction of stator current is defined by the rule that positive stator current produces positive flux linkage. By ignoring the nonlinear effect of material, the flux linkage can be expressed as:

$$
\begin{cases}
\Psi_d = \Psi_p + \sqrt{2} \cdot I_d \cdot L_d \\
\Psi_q = \sqrt{2} \cdot I_q \cdot L_q
\end{cases}
\tag{3.2}
$$

where Ψ_d and Ψ_q are flux linkages in d- and q-axis, L_d and L_q are corresponding inductances, and Ψ_p is permanent magnet flux linkage.

The EMF can be expressed as:

$$
\begin{cases}
E_d = -\omega \cdot \dfrac{\Psi_q}{\sqrt{2}} \\
E_q = \omega \cdot \dfrac{\Psi_q}{\sqrt{2}}
\end{cases}
\tag{3.3}
$$

where ω is electrical angular velocity.

From (3.1), (3.2) and (3.3), the stator voltages can be expressed as:

$$
\begin{cases}
V_d = I_d \cdot R_s - \omega \cdot I_q \cdot L_q \\
V_q = I_q \cdot R_s + \omega \cdot I_d \cdot L_d + \omega \cdot \dfrac{\Psi_p}{\sqrt{2}}
\end{cases}
\tag{3.4}
$$

3.2.3 Calculation of Permanent Magnet Flux Linkage and Inductances

When executing an FEA, stator currents (I_d and I_q) or stator voltages (V_d and V_q) should be given. However, the operating points are given by torque, rotation speed, and control strategy as shown in Table 3.1. To avoid the long computation time that would be caused by FEA-based iteration, the stator currents at operating points are estimated by using parameters obtained from results of FEA. As ferrite magnets are utilized, which produce lower flux density in the air gap compared to rare-earth magnets, the nonlinear effect of material is ignored when calculating stator currents in given operating points.

Permanent magnet flux linkage Ψ_p can be obtained directly from FEA at no load. To calculate the inductances (L_d and L_q), a second FEA is carried out with rated currents in d- and q-axis. According to (3.2), the inductances can be expressed as follows:

$$
\begin{cases}
L_d = \dfrac{\Psi_{dn} - \Psi_p}{\sqrt{2} \cdot I_{dn}} \\
L_q = \dfrac{\Psi_{qn}}{\sqrt{2} \cdot I_{qn}}
\end{cases}
\tag{3.5}
$$

where I_{dn} and I_{qn} are rated currents in d- and q-axis, Ψ_{dn} and Ψ_{qn} are corresponding flux linkages, which are obtained by applying rated stator currents I_{dn} and I_{qn} in FEA. Initial values are set as $I_{dn} = -1\,\text{A}$ and $I_{qn} = 1\,\text{A}$ in case that the values of rated currents have not been determined.

3.2.4 Calculation of Stator Currents at Operating Point 1

At operating point 1 from Table 3.1 indexed with 1, maximum torque per ampere (MTPA) is used. Output torque $T_{o,1}$ can be expressed as:

$$
T_{o,1} = \frac{m}{2} \cdot p \cdot \left[\frac{\Psi_p}{\sqrt{2}} + (L_d - L_q) \cdot I_{d,1} \right] \cdot I_{q,1}
\tag{3.6}
$$

where m is the phase number, $I_{d,1}$ and $I_{q,1}$ are the currents in d- and q-axis at this operating point, and p is the number of pole pairs.

The corresponding RMS value of the stator current $I_{s,1}$ can be expressed as:

$$
I_{s,1} = \sqrt{I_{d,1}^2 + I_{d,1}^2}
\tag{3.7}
$$

3. Optimization Process and Analysis

The phase angle between q-axis and stator current is labeled γ_1 and illustrated in Fig. 3.3.
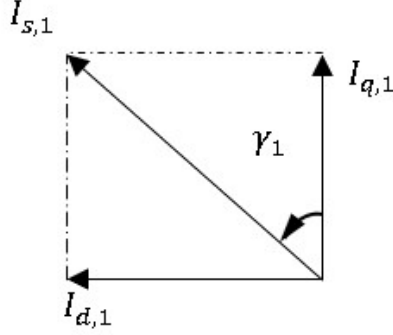
Fig. 3.3 Illustration of phase angle γ_1 between q-axis and stator current.

The relationship between $I_{d,1}$, $I_{q,1}$, $I_{s,1}$ and γ_1 can be described by following equations:

$$\begin{cases} I_{d,1} = -I_{s,1} \cdot \sin \gamma_1 \\ I_{q,1} = I_{s,1} \cdot \cos \gamma_1 \end{cases} \tag{3.8}$$

The inductances satisfy the following condition for both motors:

$$L_d < L_q \tag{3.9}$$

In order to obtain positive reluctance torque, $I_{d,1}$ must be negative, and γ_1 must be in the range of:

$$0 < \gamma_1 < \frac{\pi}{2} \tag{3.10}$$

From (3.6), (3.8) and (3.10), $I_{s,1}$ can be derived as a function of γ_1:

$$I_{s,1} = \frac{\frac{\Psi_p}{\sqrt{2}} \cdot \cos \gamma_1 + \sqrt{\frac{4 \cdot T_{o,1}}{m \cdot p} \cdot (L_d - L_q) \cdot \sin 2\gamma_1}}{(L_d - L_q) \cdot \sin 2\gamma_1} \tag{3.11}$$

When MTPA is applied for a fixed output torque $T_{o,1}$, $I_{s,1}$ is minimized by solving the following problem:

$$\begin{aligned} \min \quad & I_{s,1}(\gamma_1) = \frac{\frac{\Psi_p}{\sqrt{2}} \cdot \cos \gamma_1 + \sqrt{\frac{4 \cdot T_{o,1}}{m \cdot p} \cdot (L_d - L_q) \cdot \sin 2\gamma_1}}{(L_d - L_q) \cdot \sin 2\gamma_1} \\ \text{subject to} \quad & 0 < \gamma_1 < \frac{\pi}{2} \end{aligned} \tag{3.12}$$

Then $I_{d,1}$ and $I_{q,1}$ can be obtained by using (3.8).

3.2.5 Calculation of Stator Currents at Operating Point 2

At operating point 2, field weakening (FW) is used. Similar to (3.6), output torque $T_{o,2}$ can be expressed as:

$$T_{o,2} = \frac{m}{2} \cdot p \cdot \left[\frac{\Psi_p}{\sqrt{2}} + (L_d - L_q) \cdot I_{d,2}\right] \cdot I_{q,2} \tag{3.13}$$

where $I_{d,2}$ and $I_{q,2}$ are currents in d- and q-axis at operating point 2.

The corresponding RMS value of stator voltage $V_{s,2}$ can be expressed as:

$$V_{s,2} = \sqrt{V_{d,2}^2 + V_{q,2}^2} = V_{om} \tag{3.14}$$

where $V_{d,2}$ and $V_{q,2}$ are the stator voltages in d- and q-axis at this operating point and V_{om} is the RMS value of maximum allowable stator voltage.

From (3.4), the relationship between stator voltages ($V_{d,2}$ and $V_{q,2}$) and stator currents ($I_{d,2}$ and $I_{q,2}$) can be derived as:

$$\begin{cases} V_{d,2} = I_{d,2} \cdot R_s - \omega_2 \cdot I_{q,2} \cdot L_q \\ V_{q,2} = I_{q,2} \cdot R_s + \omega_2 \cdot I_{d,2} \cdot L_d + \omega_2 \cdot \dfrac{\Psi_p}{\sqrt{2}} \end{cases} \tag{3.15}$$

where ω_2 is electrical angular velocity at operating point 2.

By substituting the voltages in (3.14) by (3.15), the following equation can be obtained:

$$\sqrt{(I_{d,2} \cdot R_s - \omega_2 \cdot I_{q,2} \cdot L_q)^2 + (I_{q,2} \cdot R_s + \omega_2 \cdot I_{d,2} \cdot L_d + \omega_2 \cdot \frac{\Psi_p}{\sqrt{2}})^2} = V_{om} \tag{3.16}$$

$I_{d,2}$ and $I_{q,2}$ can be found by simultaneous solving of equations (3.13) and (3.16).

If the required torque exceeds the value achievable for a given voltage and speed, the equation system will not render a solution.

This problem can also be explained by number of intersections of constant torque and constant voltage curves, the former corresponding to (3.13), and the latter corresponding to (3.16). As shown in Fig. 3.4, the number of intersections varies from 0 to 2 with increasing voltage, which means the number of solutions of (3.13) and (3.16) also increases from 0 to 2.

To achieve an automatic optimization process, it is necessary to avoid the interruption of optimization process caused by non-existing solutions of equations. In this case, V_{trans}, corresponding to the minimum required voltage for given output torque, is used instead of V_{om}. $I_{d,2}$ and $I_{q,2}$ are then determined by using (3.13) and following equation instead

3. Optimization Process and Analysis

of (3.16):

$$\sqrt{(I_{d,2} \cdot R_s - \omega_2 \cdot I_{q,2} \cdot L_q)^2 + (I_{q,2} \cdot R_s + \omega_2 \cdot I_{d,2} \cdot L_d + \omega_2 \cdot \frac{\Psi_p}{\sqrt{2}})^2} = V_{trans} \qquad (3.17)$$

with $V_{trans} > V_{om}$.
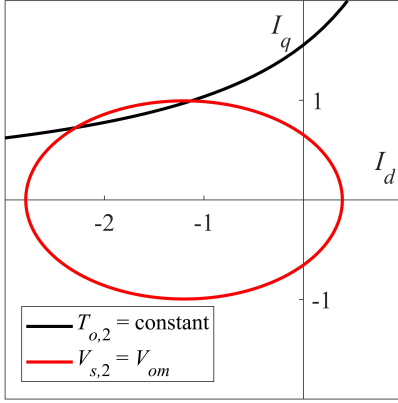
(a)
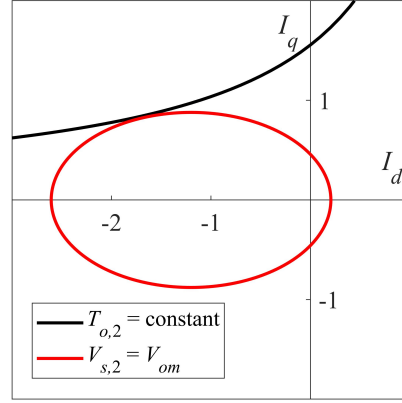
(b)
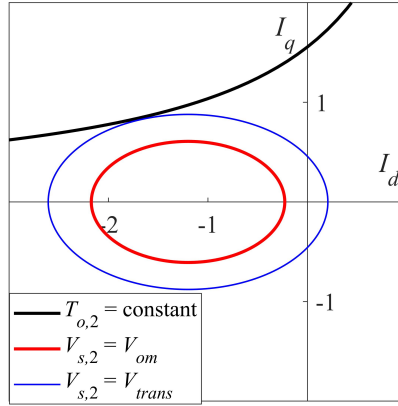
(c)

Fig. 3.4 Constant torque curve and constant voltage curves with different voltages. (a) Two intersections. (b) Transition state with one intersection. (c) No intersection.

In practice, a new parameter V_e is defined:

$$V_e = V_{trans} - V_{om} \qquad (3.18)$$

The minimum value of V_e labeled $V_{e,min}$ is used to evaluate lack of field weakening (FW) capacity of given motors. The currents $I_{d2,1}$ and $I_{q2,1}$ for $V_{e,min}$ are used for further calculation. In order to continue a smooth calculation process without disambiguations, the result of (3.18) is set $V_{e,min} = 0$ in case of $V_{trans} \leq V_{om}$.

When there are two intersections as in Fig. 3.4(a), the one with both lower total and demagnetizing current is chosen in order to get the best efficiency and decrease the risk of irreversible demagnetization.

When both MTPA and FW requirements are respected, a positive value $I_{d2,1} > 0$ will not render an efficient operating point. So it will be set $I_{d2,1} = 0$ in the following calculation. The corresponding $I_{q2,1}$ will be calculated by using (3.13). These stator current constraints will be considered in Section 3.3.2.

3.2.6 Calculation of of Detailed Characteristics by FEA

In the preceding sections, the stator currents for both operating points have been determined. A 2D FEA can be carried out by applying these stator currents, and more detailed results can be obtained thereof including precise torque and EMF. Further evaluation concerns torque ripple, efficiency, and power factor. In this section, the subscript j is used to represent two operating points, which satisfies:

$$j = 1 \quad \text{or} \quad j = 2 \tag{3.19}$$

The torque ripple coefficient $k_{t,j}$ can be calculated from the torque waveform in one electrical period:

$$k_{t,j} = \frac{T_{max,j} - T_{min,j}}{2 \cdot T_{av,j}} \tag{3.20}$$

where $T_{av,j}$, $T_{max,j}$, and $T_{min,j}$ are average torque, maximum torque, and minimum torque in one electrical period, respectively.

Before calculating efficiency and power factor, output power and losses should be figured out. Output power can be calculated from output torque and electrical angular velocity:

$$P_{o,j} = \frac{T_{av,j} \cdot \omega_j}{p} \tag{3.21}$$

where $P_{o,j}$ and ω_j are output power and electrical angular velocity at j^{th} operating point, respectively.

Losses $P_{loss,j}$ mainly contain three components: copper losses $P_{Cu,j}$, iron losses $P_{Fe,j}$, and friction losses $P_{f,j}$:

$$P_{loss,j} = P_{Cu,j} + P_{Fe,j} + P_{f,j} \tag{3.22}$$

Copper losses $P_{Cu,j}$ can be calculated from stator current:

$$P_{Cu,j} = m \cdot I_{RMS,j}^2 \cdot R_s \tag{3.23}$$

where $I_{RMS,j}$ is root mean square (RMS) phase value of stator current.

Iron losses $P_{Fe,j}$ can be calculated as follows [162]:

$$P_{Fe,j} = \sum_k [K_h \cdot f_j \cdot B_{m,j,k}^2 + K_c \cdot (f_j \cdot B_{m,j,k})^2 + K_e \cdot (f_j \cdot B_{m,j,k})^{1.5}] \tag{3.24}$$

where K_h, K_c, and K_e represent hysteresis, eddy-current, and excess core loss coefficients, $B_{m,j,k}$ represents the peak value of AC component of the flux density in the kth element in steel sheets, f_j is the frequency at j^{th} operating point.

Friction losses between rotor and air gap can be calculated as given in [163]:

$$P_{f,j} = C_{M,j} \cdot \pi \cdot \rho \cdot \omega_j^3 \cdot r_r^4 \cdot l_r \tag{3.25}$$

where ρ represents the density of air, r_r represents the outer radius of rotor, l_r represents the length of the rotor stack, and $C_{M,j}$ represents the coefficient of friction losses, which has different expressions when the Reynolds number varies:

$$C_{M,j} = \begin{cases} 10 \cdot \dfrac{(\frac{\delta}{r_g})^{0.3}}{Re_{\delta,j}} & \text{when} \quad 0 < Re_{\delta,j} < 64 \\[2ex] 2 \cdot \dfrac{(\frac{\delta}{r_g})^{0.3}}{Re_{\delta,j}^{0.6}} & \text{when} \quad 64 \le Re_{\delta,j} < 500 \\[2ex] 1.03 \cdot \dfrac{(\frac{\delta}{r_g})^{0.3}}{Re_{\delta,j}^{0.5}} & \text{when} \quad 500 \le Re_{\delta,j} < 10,000 \\[2ex] 0.065 \cdot \dfrac{(\frac{\delta}{r_g})^{0.3}}{Re_{\delta,j}^{0.2}} & \text{when} \quad 10,000 \le Re_{\delta,j} \end{cases} \tag{3.26}$$

in which δ represents the radial air gap length, r_g represents the average radius of air gap, and $Re_{\delta,j}$ represents the Reynolds number.

The Reynolds number is defined as follows:

$$Re_{\delta,j} = \frac{\omega_j \cdot r_g \cdot \delta}{\nu} \tag{3.27}$$

where ν is the kinematic viscosity of air. When calculating the Reynolds number, the effects of slots are ignored.

Efficiency η_j and power factor λ_j can then be found as:

$$\eta_j = \frac{P_{o,j}}{P_{o,j} + P_{loss,j}} \tag{3.28}$$

$$\lambda_j = \frac{P_{o,j} + P_{loss,j}}{m \cdot V_{RMS,j} \cdot I_{RMS,j}} \tag{3.29}$$

in which $V_{RMS,j}$ represents the RMS phase value of the stator voltage, m is the phase number.

3.3 Optimization Conditions for a Spoke-type Synchronous Motor

3.3.1 Fixed Parameters and Variables

The FE model used in this chapter is totally parametric, so theoretically all geometrical magnitudes can be regarded as variables. It is however unnecessary to do so, as some parameters are fixed by given applications, and some others are non-independent.

According to [117], the amount of permanent magnet flux should be selected properly to achieve a wide constant power speed range. Related parameters are length, width, and coercivity of each permanent magnet, pole pitch and axial motor length, and radial air gap length. Other important parameters are basic configuration of the motor and specifications related to winding and geometry of laminations.

In practice, 6 parameters are selected as variables as listed in Table 3.2 because they impact the properties most. The axial core length, which is set to be the same for the stator stack, rotor stack, and permanent magnets, is selected as the first variable, because they concern the cost of material. The second one is the radial air gap length. It has a strong impact on the performance of motors. The next one is the number of turns per slot of the stator winding considering that it concerns the amount of copper usage when the diameter of conductors is fixed. The fourth one is the remanence of magnets, with the consideration that the amount of permanent magnet flux is not the higher the better for motors designed for variable-speed applications. So the grade of ferrite magnets can be selected appropriately. Width and length of each magnet are also chosen as variables, because they are closely related to the amount of permanent magnet flux and volume of magnets.

Table 3.2   Variables for a spoke-type synchronous motor

Variable	Minimum	Maximum
Core length l_e/mm	30	50
Air gap length δ/mm	1	5
No. of turns per slot N_s	50	250
Remanence of ferrite magnet B_r/T	0.2	0.4
Width of each ferrite magnet w_p/mm	1	6
Length of each ferrite magnet l_p/mm	5	16

Some other parameters have been fixed. The details of some fixed parameters are listed in Table 3.3. According to [94], the 12-slot/10-pole configuration has lower cost and better overall performance than those with less slots and poles. Although better performance can be obtained by choosing higher numbers of slots or poles or both, this configuration has been chosen considering that the number of slots and poles should be limited for small motors to avoid high manufacturing cost. The widths of yoke and teeth

have been fixed to avoid deep saturation. Non-independent parameters such as outer diameter of stator and size of slots can be derived from variables and fixed parameters.

Table 3.3 Fixed parameters for a spoke-type synchronous motor

Fixed parameter	Value
Number of phases	3
Number of poles	10
Number of slots	12
Width of yoke	7 mm
Width of teeth	9 mm
Diameter of shaft	12 mm
Fill factor	0.50
Diameter of conductors	0.8 mm
Number of parallel branches	1

3.3.2 Constraints and Penalty Functions

Normally, constraints define the feasible region of an optimization. Only designs inside the feasible region have valid values of the objective function, while the ones outside the feasible region are simply sorted out. This approach can lead to problems when the constraints are rather complex. The optimization must start within a feasible region which requires extra computation. The process becomes difficult when the feasible region consists of several domains instead of one connected domain. Some constraints are hard and may not be violated, whereas others are soft and can be compromised when the constraints cannot be simultaneously satisfied. Therefore the constraints are given different levels of priorities.

In this thesis, constraints are divided into two groups. The first group directly limits variables according to the list in Table 3.2. These constraints require no special actions as they can be checked directly without executing an FEA. The other group consists of functions invoking results from an FEA, e.g. constraints of torque ripple coefficient and field weakening capacity. Penalty functions are added to the objective function to deal with the latter. Fig. 3.5 gives a description of the principle of a penalty function, where $F(x)$, $g(x)$, and $f_p(x)$ are objective, constraint, and penalty function respectively, ϵ is the coefficient of priority, and g_0 is the base value of $g(x)$. When a constraint is satisfied, the corresponding penalty function equals zero. When it is violated, the corresponding penalty function quantifies the degree of violation considering its importance. A negative term is then added to the objective function. By using penalty functions, the optimization makes full use of the results of 'faulty designs' instead of throwing them away directly.

$$\text{max:} \quad F(x)$$
$$\text{subject to:} \quad g(x) \geq 0$$

simple optimization function without penalty function

$$\text{max:} \quad F(x) + f_p(x)$$
$$\text{where} \quad f_p(x) = \begin{cases} 0 & g(x) \geq 0 \\ \dfrac{\varepsilon \cdot g(x)}{g_0} & g(x) < 0 \end{cases}$$

optimization function with penalty function
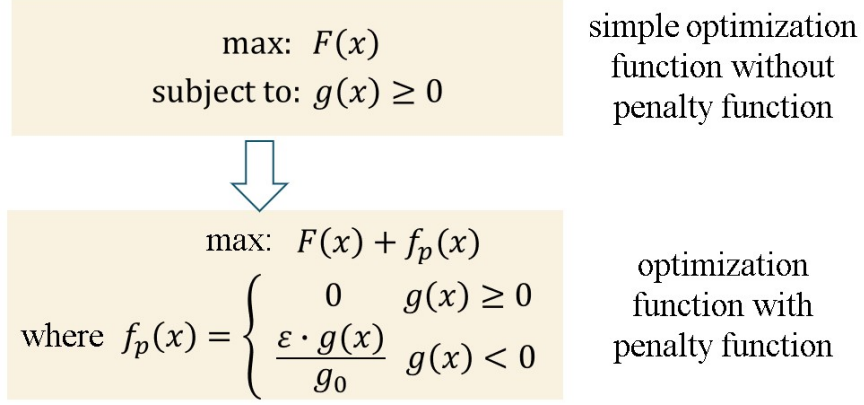
Fig. 3.5 Objective functions with and without penalty function.

Some new parameters are defined combining two operating points for a discussion of the motor's performance. Average efficiency η_{av} is calculated as:

$$\eta_{av} = \frac{P_{o,1} \cdot t_1 + P_{o,2} \cdot t_2}{\frac{P_{o,1} \cdot t_1}{\eta_1} + \frac{P_{o,2} \cdot t_2}{\eta_2}} \tag{3.30}$$

where $P_{o,1}$ and $P_{o,2}$ are the output powers, η_1 and η_2 are the efficiencies, t_1 and t_2 are the equivalent operating periods.

For power factor, its minimum value λ_{min} is considered:

$$\lambda_{min} = \min(\lambda_1, \lambda_2) \tag{3.31}$$

where λ_1 and λ_2 are the power factors in both operating points.

For the torque ripple coefficient, its maximum value $k_{t,max}$ is used:

$$k_{t,max} = \max(k_{t,1}, k_{t,2}) \tag{3.32}$$

where $k_{t,1}$ and $k_{t,2}$ are the torque ripple coefficients in both operating points.

The current density $J_{s,j}$ at the jth operating point in the stator winding can be calculated as:

$$J_{s,j} = \frac{4 \cdot I_{RMS,j}}{\pi \cdot a \cdot d_c^2} \tag{3.33}$$

in which a is the number of parallel branches, and d_c is the diameter of the conductors without insulation.

The maximum current density value $J_{s,max}$ then follows as:

$$J_{s,max} = \max(J_{s,1}, J_{s,2}) \tag{3.34}$$

where $J_{s,1}$ and $J_{s,2}$ are the current densities in both operating points.

35

The ratio between losses and the surface area of motor must be limited due to heating. The maximum heat flux $k_{heat,j}$ is calculated as:

$$k_{heat,max} = \max(\frac{P_{loss,j}}{A_s}) \tag{3.35}$$

where A_s is the surface area of motor.

An error flag k_{error} representing some unexpected errors is also defined:

$$k_{error} = \begin{cases} 0 & \text{when there is no unexpected error} \\ 1 & \text{when an unexpected error happens} \end{cases} \tag{3.36}$$

Unexpected errors include failures of modeling, meshing, convergence leading to a failure of FEA. By considering them, the optimization process can become more stable.

As discussed in Section 3.2.5, $V_{e,min}$, the minimum value of V_e which is described in (3.18), can be used to evaluate the field weakening capacity of a motor. So it is used as base of the penalty function. A constraint for the outer radius of stator r_s is also used to limit the size of motor.

Generally, a penalty function $f_{p,i}$ is defined corresponding to the ith constraint. For a lower bound constraint where $X_i \geq X_{min,i}$ is desired, the corresponding $f_{p,i}$ is defined as:

$$f_{p,i} = \frac{(X_i - X_{min,i}) - |X_i - X_{min,i}|}{2 \cdot X_{b,i}} \epsilon_i \tag{3.37}$$

For an upper bound constraint where $X_i \leq X_{max,i}$ is desired:

$$f_{p,i} = \frac{(X_{max,i} - X_i) - |X_{max,i} - X_i|}{2 \cdot X_{b,i}} \epsilon_i \tag{3.38}$$

For a bound constraint where $X_{min,i} \leq X_i \leq X_{max,i}$ is desired:

$$f_{p,i} = \frac{(X_i - X_{min,i}) - |X_i - X_{min,i}|}{2 \cdot X_{b,i}} \epsilon_i + \frac{(X_{max,i} - X_i) - |X_{max,i} - X_i|}{2 X_{b,i}} \epsilon_i \tag{3.39}$$

where X_i represents the parameter in the ith constraint, $X_{min,i}$ and $X_{max,i}$ are the corresponding lower and upper limits, $X_{b,i}$ is the base value to normalize X_i, and ϵ_i is the coefficient of priority defining the grade of ith constraint.

The constraints are listed in Table 3.4. They are divided into three grades. The highest priority coefficient $\epsilon = 100,000$ is given to unexpected error flag. When this error occurs, the results are unreliable. So this one must be checked first of all. As the constraints of torque ripple, current density, heat flux, outer radius, and field weakening capacity should not be violated in the final design, the second highest priority coefficient $\epsilon = 1,000$ is assigned to them. The lowest priority coefficient $\epsilon = 25$ is allocated to efficiency and power factor, which means they can be compromised to make sure that the other constraints are able to be satisfied when all of them cannot be met simultaneously.

Table 3.4   Details of the constraints

i	X_i	$X_{min,i}$	$X_{max,i}$	$X_{b,i}$	ϵ_i
1	η_{av}	0.8	——	1	25
2	λ_{min}	0.8	——	1	25
3	$k_{t,max}$	——	0.15	0.15	1,000
4	$J_{s,max}/(\mathrm{A/mm^2})$	——	5	5	1,000
5	$k_{heat,max}/(\mathrm{W/mm^2})$	——	0.002,5	0.002,5	1,000
6	k_{error}	——	0	1	100,000
7	r_s/mm	——	60	60	1,000
8	$V_{e,min}/\mathrm{V}$	——	0	200	1,000

3.3.3   Objective Function

For the optimization, the total cost of material is set as the objective. Relative costs of the main components have been estimated based on several resources [164–167]. Table 3.5 gives an overview of the values used.

Table 3.5   Costs of material

Material	Normalized cost
Steel sheets	1
Copper	3.75
Ferrite	5

In this dissertation, the objective function $F(x)$ is defined as:

$$F(x) = 1 - \frac{f_{cost}}{f_{cost,b}} + \sum_{i=1}^{8} f_{p,i} \tag{3.40}$$

where f_{cost} represents the total cost of material, and $f_{cost,b}$ is the corresponding base value. The value of $f_{cost,b}$ can be obtained by a rough estimation of f_{cost}, which is based on the model by using the average value of upper and lower limits for each variable in Table 3.2. When a constraint is satisfied, the corresponding penalty function will output 0, otherwise it will render a negative value. The cost function f_{cost} outputs a positive value and shall be minimized.

The objective function is also named fitness function.

This approach has transferred a constrained optimization into an unconstrained one except for the limit of some variables. The objective is to find the maximum value of this fitness function. For a design which statifies all constraints and has a cost close to $f_{cost,b}$, a fitness close to 0 is expected.

3.4 Optimization Conditions for Permanent-magnet Assisted Synchronous Reluctance Motors

3.4.1 Fixed Parameters and Variables

For permanent-magnet assisted synchronous reluctance motors (PMASynRMs), the layout of permanent magnets is far more complex than the one in spoke-type synchronous motors. To simplify the problem, the relative position of the center of each magnet to the radius of the rotor is fixed. Two variables are then used related to magnets, i.e. the radius of rotor r_r and p. u. magnet width k_{width}, which is defined as follows:

$$k_{width} = \frac{w_{pa}}{w_{p0}} \qquad (3.41)$$

in which w_{pa} represents the actual width of a magnet, and w_{p0} is the corresponding base value defined in the original rotor. By using r_r and k_{width}, modifications can be made to the original rotor.

As mentioned before, the other variables are core and air gap lengths, number of turns per slot, and remanence of ferrite magnets. The details are listed in Table 3.6.

Table 3.6 Variables for a PMASynRM

Variable	Minimum	Maximum
Core length l_e/mm	30	50
Air gap length δ/mm	1	5
No. of turns per slot N_s	50	250
Remanence of ferrite magnet B_r/T	0.2	0.4
Rotor radius r_r/mm	0.25	0.32
P. u. magnet width k_{width}	0.75	1.25

Various independent parameters have been fixed according to Table 3.7. Further non-independent parameters can be derived from fixed parameters and variables.

In [148] and [149], the suggested configurations with fractional-slot windings for PMASynRMs all have a high number of poles (at least 8). However, this is difficult to realize for PMASynRMs with limited rotor size. As a consequence of the resulting low pole number, configurations with integer-slot windings are considered. In order to keep the same number of slots as in the spoke-type synchronous motor, the 12-slot/4-pole configuration is selected. The configurations with integer-slot winding usually have higher torque ripple and longer end windings, which will be discussed later.

Table 3.7   Fixed parameters for a PMASynRM

Fixed parameter	Value
Number of phases	3
Number of poles	4
Number of slots	12
Width of yoke	5 mm
Width of teeth	7 mm
Diameter of the shaft	12 mm
Copper fill factor	0.50
Diameter of conductors	0.8 mm
Number of parallel branches	1

3.4.2   Constraints, Penalty Function, and Objective Function

The definitions and specifications of constraints, penalty function, and objective function for a PMASynRM are kept the same as the ones for a spoke-type synchronous motor, except for the limits of the two new variables in the last two lines of Table 3.6.

3.5   Optimization Algorithms

The systematic optimization of a motor with an FE model is usually a complex problem, in which the global optimum must be found out among local optima [168]. Apart from continuous variables, discrete variables are often required to be included. For example, N_s can only be an integer. The objective function and constraints contain the results from FEA, which means they are nonlinear and cannot be simplified into analytical expressions. The objective function can also be non-smooth due to the existence of noise in FEA. When selecting optimization algorithms, it is necessary to take these factors into consideration.

In general, optimization algorithms can be classified into deterministic and stochastic algorithms [169, 170].

The deterministic algorithms can be further divided into two groups using derivative information or not. Newton's method and quasi-Newton method belong to the first group, while the Nelder-Mead method belongs to the second group using the comparison of function values instead of derivative information. The latter method is often selected when the objective function is non-smooth [171]. The problem of the deterministic algorithms is that the optimization process can be trapped in a local optimum in some situations [169].

The stochastic algorithms are a group of algorithms that include random processes, which are usually learned from natural phenomena. Typical members are particle swarm optimization, genetic algorithms, differential evolution, and simulated annealing [169, 170]. Compared to deterministic algorithms, stochastic ones are usually

relatively less efficient but have the capability to find the global optimum [170]. Another characteristic is that the search process can be different in each round with the same specifications, which is caused by the random process [169].

In this thesis, a genetic algorithm, the Nelder-Mead method, the quasi-Newton method, and some combinations of them have been considered.

3.5.1 Introduction of Genetic Algorithms

Genetic algorithms can find the global optimum and have been reported for optimization of motor design [172–174]. They are based on the theory of natural evolution. The variables are coded as chromosomes and each design is seen as an individual in the society. The values of variables and the objective function of a design are seen as its genes and fitness, respectively. The initial generation can be generated at random or given directly, and a new generation is produced by the former generation. The reproduction process is based on selection, crossover, and mutation operations. The individuals with higher fitness are more likely to be selected to generate the next generation [175]. After several generations, the population tends to have a higher overall fitness and finally approaches the global optimum. The termination conditions can be given by the maximum number of generations or minimum diversity of the current population.

A description of the process of a genetic algorithm is illustrated in Fig. 3.6.

3.5.2 Introduction of the Nelder-Mead Method

The Nelder-Mead method belongs to direct search methods that only use the value of the objective function and do not require information on derivatives [171, 176]. The original work of Nelder and Mead can be found in [177]. This algorithm is based on a simplex, which is the convex hull of $n_v + 1$ vertices of a polytope for a vector of variables with a dimension n_v [176].

The algorithm consists of three steps, i.e. generating an initial simplex, transforming the working simplex until the terminatin condition is satisfied, and returning the results [176]. The initial value of the optimization is set as the first vertex. Then the initial simplex can be generated with the help of a set of base vectors. Basic operations of transformation are reflection, expansion, contraction, and shrinking.

In MATLAB, the Nelder-Mead algorithm can be realized by 'fminsearch' function directly.
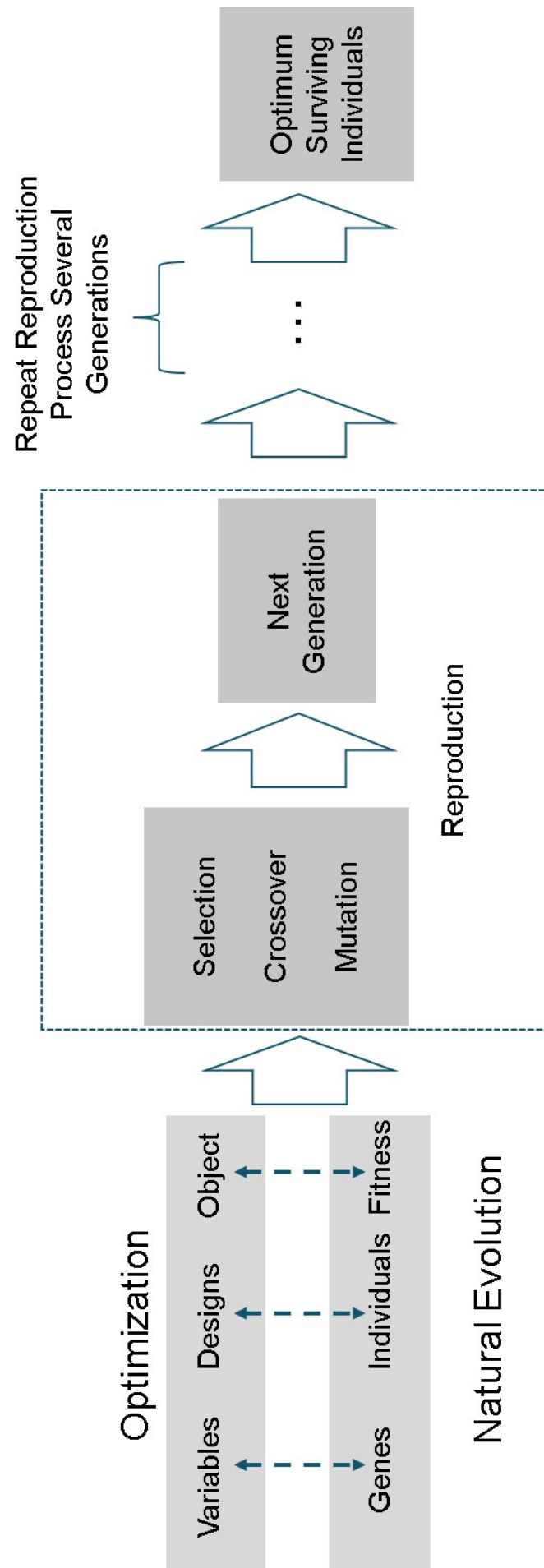
Fig. 3.6   The process of a genetic algorithm.

3.5.3   Introduction of the Quasi-Newton Method

Newton's method is an algorithm that uses information on first and second derivatives. The iterative scheme can be described as:

$$x_{l+1} = x_l - [F''(x)]^{-1} \cdot F'(x) \tag{3.42}$$

where x_l represents the values of variables in l^{th} iteration, $F'(x)$ and $F''(x)$ represent derivative and second derivative of the objective function $F(x)$.

The problem of Newton's method is that the inverse of a Hessian matrix must be calculated, which is usually time consuming. The quasi-Newton method does not require such calculation. Instead, it is simplified by estimating the required information directly.

In MATLAB, the 'fminunc' function realizes one quasi-Newton algorithm, the so-called BFGS method.

3.5.4   Combined Configurations

All algorithms have limitations. Theoretically genetic algorithms can approach the global optimum, but they become slow and inefficient when getting close to the target. Both Nelder-Mead and quasi-Newton methods usually find local optima, and they cannot deal with discrete variables. As a consequence, different combinations of these algorithms are discussed in this thesis.

For the genetic algorithm, the termination condition is that the best fitness increases less than 1×10^{-4} p. u. of its last absolute value in 10 generations. For the other two algorithms, the convergence criterion is 1×10^{-4}, which means an increase of less than 1×10^{-4} p. u. of the last absolute value of the objective function for the Nelder-Mead method and an absolute value of the gradient of less than 1×10^{-4} p. u. of the initial gradient for the quasi-Newton method. For combined configurations, the optimization switches to the next stage when the termination condition of the former stage is satisfied. In this thesis, 5 configurations are discussed. They can be described as follows:

- Configuration 1 (Conf. 1) just uses a genetic algorithm. The list of variables includes the number of turns N_s, which is a discrete variable.

- Configuration 2 (Conf. 2) combines a genetic algorithm and the Nelder-Mead method. The genetic algorithm is executed first using an integer value for N_s. Then the Nelder-Mead method is used in order to make the calculation faster. Because the Nelder-Mead method cannot deal with discrete variables, the last value for N_s from the genetic algorithm solution is fixed in the second stage, which means the optimization is finished by using a reduced number of variables.

- Configuration 3 (Conf. 3) also combines a genetic algorithm and the Nelder-Mead method. The first stage still uses a genetic algorithm, but N_s is set to be

continuous. The second stage uses the Nelder-Mead method with a continuous N_s. After rounding N_s to an integer and fixing that value, a third stage follows the Nelder-Mead method in the same way as the second stage in Conf. 2.

- Configuration 4 (Conf. 4) uses the last two stages of Conf. 3.

- Configuration 5 (Conf. 5) uses twice the quasi-Newton method. In the first stage, N_s is continuous. In the next stage, it is rounded to an integer and fixed.

3.6 The Complete Optimization Process

After the preparation from Sections 3.1 to 3.5, the complete optimization process can be set up. Fig. 3.7 gives a flowchart describing this process.

The first steps are setting up the FE model and initializing of the optimization. The initial generation is generated at random when genetic algorithms are used as the first stage. For the other two algorithms used in this stage, an initial point must be provided manually. Basic parameters are figured out based on FEA with rated currents and in no load condition. They are then used to estimate the currents for given operating points. The fitness function of each design is then calculated based on a second FEA with estimated currents at given operating points. After that, the fitness function is passed to the optimization algorithm for its iterations. The complete process of the evaluation of fitness is packaged as a function, so that it is independent from optimization algorithms except the transmission of the values of variables and the objective function. When the termination conditions are satisfied, the optimization process ends. Finally the results are saved for further actions.

3.7 Comparison and Analysis

Computation cost is evaluated by number of evaluations of the fitness function instead of computation time, so that the conclusion does not vary in different platforms.

In total, 8 optimization processes have been carried out as presented in Table 3.8. Fig. 3.8 shows the convergence processes of the best designs of both motors. A summary can then be made as follows:

- Confs. 1, 2, and 3 can achieve acceptable results, which indicates that the genetic algorithm is suitable for the optimization in this thesis. The Nelder-Mead method further trims the results to the closest local optimum in case that the genetic algorithm stage only provides a point near a local optimum.

- In general, Conf. 1 is the fastest, because it has only one stage. Conf. 3 has the largest computation cost but provides the best result, so it is accepted as the final solution.
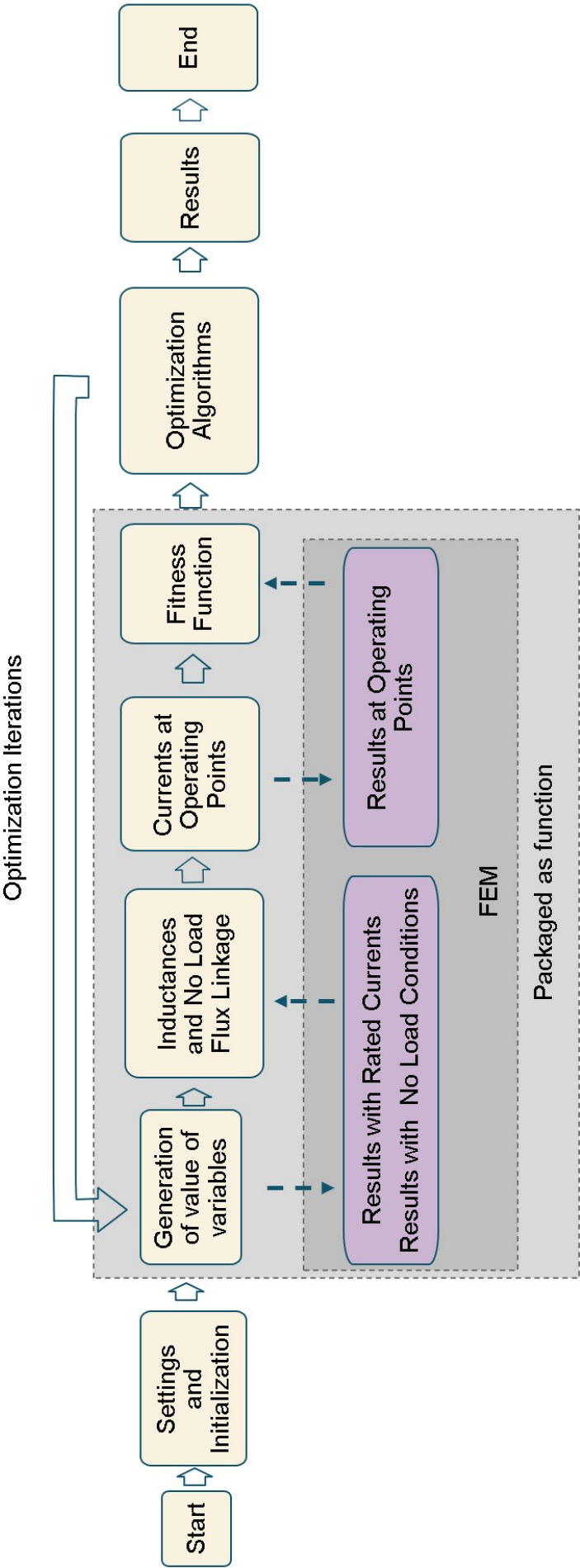
Fig. 3.7 The complete optimization process.

Table 3.8   Results of different configurations

| | Number | Method | Initial fitness | Fitness after each stage | | | Final fitness | Number of evaluations |
				Stage 1	Stage 2	Stage 3		
Spoke-type motor	1	Conf. 1	——	-1.981	——	——	-1.981	2,100
	2	Conf. 2	——	-1.981	-1.981	——	-1.981	2,448
	3	Conf. 3	——	-1.549	-1.534	-1.533	-1.533	2,507
	4	Conf. 4	-31,682	-2,010.4	-225.77	——	-225.77	751
	5	Conf. 4	-22,226	-5,376.6	-695.82	——	-695.82	803
	6	Conf. 5	-31,682	-31,682	-31,682	——	-31,682	144
	7	Conf. 5	-22,226	-22,226	-22,180	——	-22,180	156
PMASynRM	8	Conf. 3	——	-0.460	-0.460	-0.431	-0.431	2,171
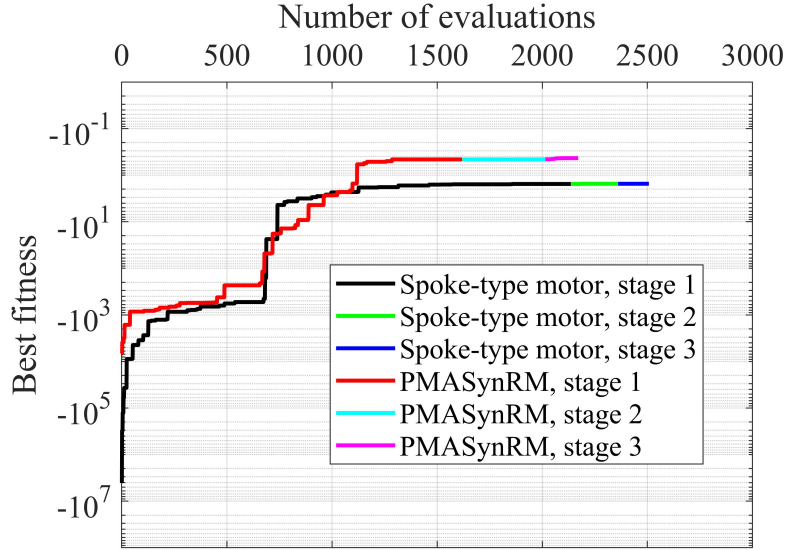
Fig. 3.8   The convergence processes of Conf. 3 for both motors.

- Conf. 4 is trapped in a local optimum which is far away from the global optimum.

- Conf. 5 converges to a point near the initial point. This is caused by the noise of FEA, which makes the usage of gradient information meaningless in such optimization process.

- Remanence reaches the maximum, which infers that a better design may be achieved by using ferrite magnets with higher remanence. But the higher cost of such magnets should also be considered.

- The radial air gap length reaches the minimum, which means a better design may be achieved by a narrower air gap when it is feasible in practice. However, the torque ripple increases with a narrower air gap.

<div style="text-align: right; font-size: 4em; color: #888;">4</div>

Design Aspects of Spoke-Type Synchronous Motors

In Chapter 3, various automatic optimization processes based on an FE model have been established. Considering practical issues, modifications must be applied based on the results obtained by using the methods in Chapter 3. There are also different variants of spoke-type synchronous motors with different layouts, which need to be discussed for given application.

In this chapter, various rotor layouts are listed first. Then these are discussed in relation to mechanical strength and irreversible demagnetization including a comparison of single- and double-layer windings in the following section. A configuration with an extended rotor stack is also examined. Finally the design of the prototype is fixed after double-checking its performance.

4.1 Different Rotor Layouts

The main characteristic of spoke-type layout is the use of tangentially magnetized permanent magnets. Various layouts are presented in Fig. 4.1.

- In the basic layout of spoke-type rotor labeled Type 1, the rotor consists of separate pieces as shown in Fig. 4.1(a). Using glue to stick these together cannot provide enough mechanical strength as the motor must operate at speeds up to 20,000 min^{-1} (corresponding to 120% of the rated speed at operating point 2 in Table 3.1 according to IEC 60034-1).

- The second solution is illustrated in Fig. 4.1(b) and labeled Type 2. The idea is to use bolts and non-magnetic end rings at both sides of the rotor stack to hold the pole segments together as illustrated in Fig. 4.1(e). Wedges retain the magnets.
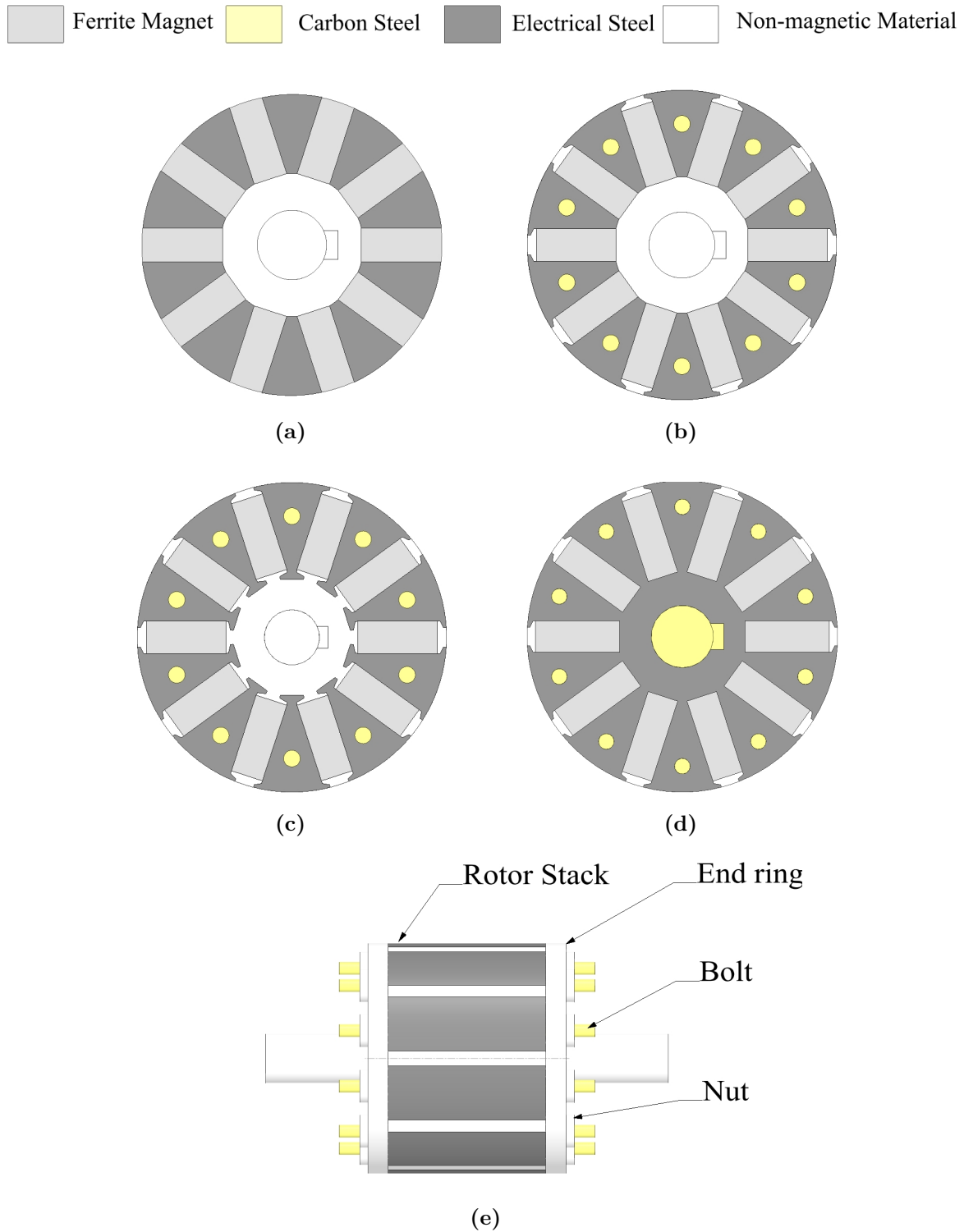
Fig. 4.1 Different rotor layouts of spoke-type rotors. (a) Type 1. (b) Type 2. (c) Type 3. (d) Type 4. (e) End rings for Types 2, 3, and 4.

- In Fig. 4.1(c), the third solution labeled Type 3 is presented. In addition to Type 2, a non-magnetic connecting hub is used to fix the pole segments. The structure is similar to the one described in [67] but differs in two aspects, because the space is limited in small electric machines. The first one is that the pole segments are designed to be inserted into the connecting hub to make the rotor more compact instead of choosing the opposite way. The second one is that a simple wedge-shaped structure is used instead of a complex fir-tree structure.

- The fourth layout is presented in Fig. 4.1(d) and labeled Type 4. The main idea is to avoid separate pieces in the rotor by keeping an inner ring in the rotor sheet.

As illustrated in Fig. 4.1(e), end rings are used in Types 2, 3, and 4 in order to fix the rotor stack in the axial direction and provide space for rotor balancing.

The main drawback of Type 4 is a large flux leakage in the inner ring, which reduces the flux produced by permanent magnets and thus also torque. Fig. 4.2 shows two variants of this Type 4 to solve this problem, which are labeled Types 4a and 4b, respectively. In Type 4a, a non-magnetic shaft is used, and the inner ring is also narrowed. The inner ring is highly saturated leading to a reduced flux leakage. In Type 4b, triangle-shaped flux barriers are added to the structure of Type 4a with the intention to saturate the magnetic bridges even more.
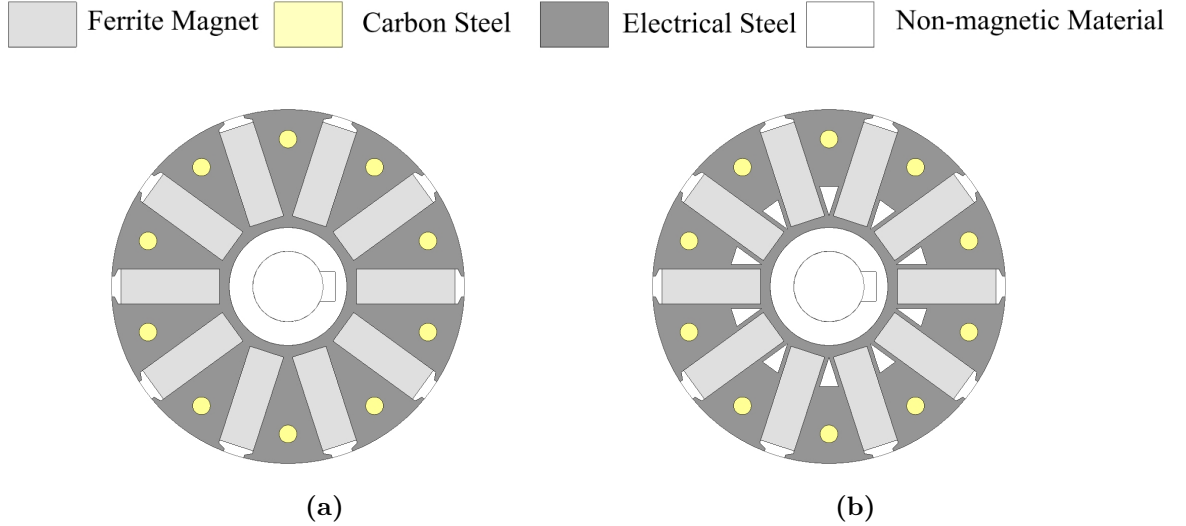
Fig. 4.2 Two variants of Type 4. (a) Type 4a. (b) Type 4b.

To analyze the effect of flux leakage in the inner ring, no load EMF and torque have been calculated for Types 2, 4, 4a, and 4b. Only inner ring and shaft were varied, whereas the outer contours close to the air gap were constant. For Type 4a, four ring sizes were calculated with different maximum (w_{in}) and minimum ($w_{in,min}$) widths of the inner ring as depicted in Fig. 4.3.
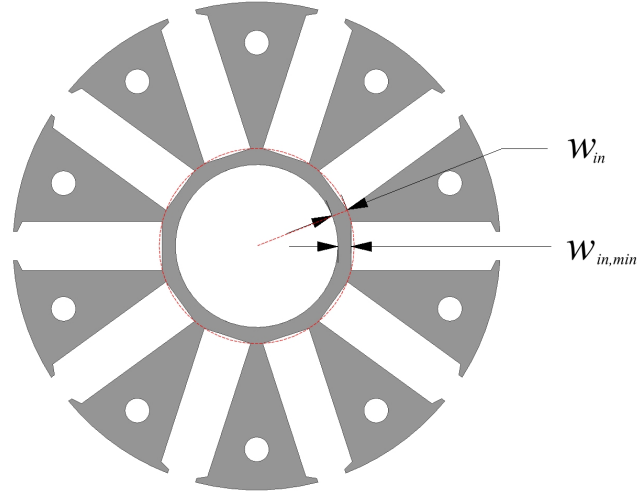
Fig. 4.3 Width and minimum width of the inner ring.

The results are listed in Table 4.1 and allow following conclusions:

Table 4.1   Comparison of no load EMF and torque among different variants

Variants	Width of inner ring/mm	No load EMF RMS/pu	Torque/pu
Type 2	——	1.48	1.51
Type 4	6	1	1
Type 4a	1	1.12	1.13
	2	1.00	1.00
	3	1.00	1.00
	6	1.00	1.00
Type 4b	1	1.15	1.16

- From Type 2 to 4, flux leakage increases significantly with size of the inner ring. No load EMF and torque decrease about 1/3.

- Comparing Type 4 and 4a, flux leakage can be reduced only by a very narrow inner ring.

- As seen from results for Type 4b vs. 4a, flux leakage can be reduced slightly by adding triangle-shaped flux barriers.

In general, the effect of the measures is less significant than expected. This can be explained by the existence of saturated bridges in Type 4. An overview and a detailed view of flux density distribution in Type 4 at no load are given in Figs. 4.4(a) and 4.4(b), respectively. In Fig. 4.4(b), it can be observed that the regions connecting inner ring and iron poles are already highly saturated in Type 4, which limits the leakage flux in inner ring.
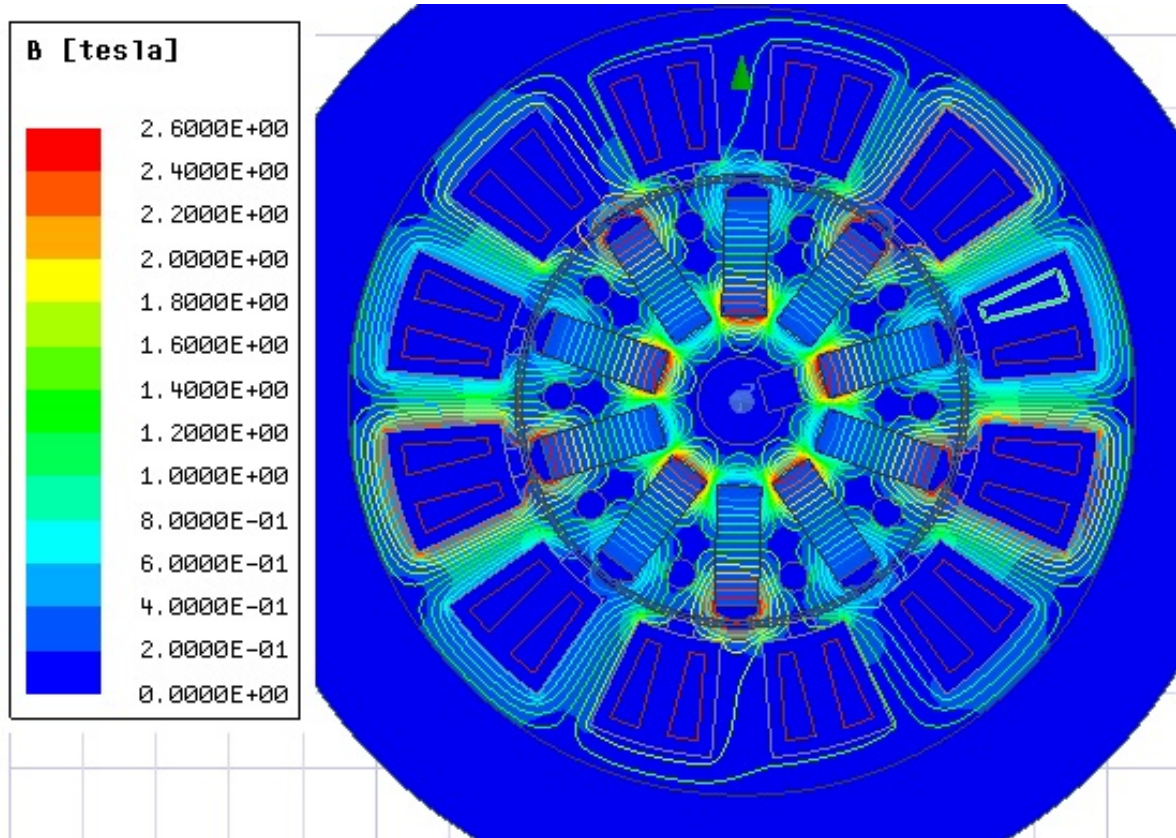
(a)
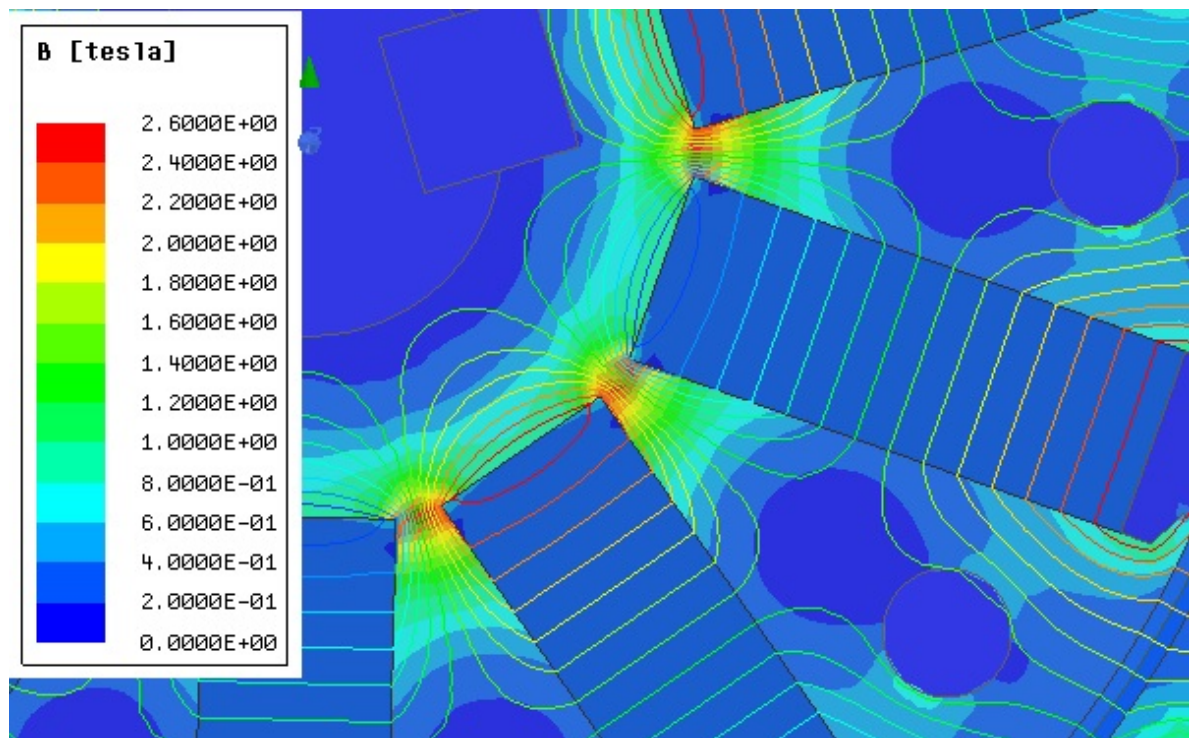
(b)

Fig. 4.4 Distribution of flux density of Type 4 at no load. (a) Overview. (b) Detailed view.

When the width of inner ring is $w_{in} = 1\,\text{mm}$, the minimum width becomes $w_{in,min} < 0.6\,\text{mm}$. Considering the feasibility of such a small dimension in mass production and potential mechanical problems, Types 4a and 4b are excluded up from here.

4.2 Mechanical Analysis

Because the centrifugal force in the rotor is proportional to the square of rotation speed, the mechanical stress in the rotor increases significantly with speed. In this thesis, the rotation speed reaches 16,600 min^{-1} in spinning mode. Thus, 120% of 16,600 min^{-1}, namely 20,000 min^{-1}, is set as the maximum rotation speed.

According to Section 4.1, Types 2, 3, and 4 need to be investigated further. The dimensions of each layout are listed in Table 4.2. They are based on the optimization process presented in Chapter 3. The size of ferrite magnets has been adjusted so that they can be found easily in the market. Basic dimensions of stacks have been rounded, since better accuracy of calculation than precision of manufacturing is unnecessary and meaningless in practice.

Table 4.2 Dimensions of different layouts

Parameters	Type 2	Type 3	Type 4
Outer diameter of stator/mm	114	114	110
Outer diameter of rotor/mm	56	56	60
Length of stacks/mm	40	40	50
Height of magnets/mm	6	6	6
Width of magnets/mm	14	14	16
Size of bolts	M4	M4	M4
Width of end rings/mm	5	5	5
Diameter of shaft/mm	12	12	12

3D static mechanical analyses have been carried out in Ansys Workbench. The two end faces of the shaft were set as fixed support. The axis of the shaft was set as the axis of rotation. The simulation was carried out for 20,000 min^{-1}. In Table 4.3, the maximum equivalent stress and yield strength of each component for the three motors are given. The yield strength can be found in different resources [178–182]. For ferrite magnet, tensile strength is used here as it is a brittle material.

Table 4.3 Results of mechanical analysis

Component	Material	Von Mises stress/MPa			Yield strength/MPa
		Type 2	Type 3	Type 4	
Shaft	S235JR	37.1	16.9	3.1	235
Bolts	S235JR	372.3	114.2	101.0	235
Stack	M270-35A	894.5	92.6	93.2	355-450
Hub	AA7075	15.6	115.0	——	360-470
End ring	AA7075	829.3	73.4	47.8	360-470
Ferrite magnet	Y30BH	14.5	15.0	14.4	34 (tensile strength)

In order to evaluate the reliability of these rotors at different speeds, the safety factor $k_{SF,s}$ of the sth component results as:

$$k_{SF,s} = \frac{\sigma_{y,s}}{\sigma_{m,s}} \tag{4.1}$$

where $\sigma_{y,s}$ and $\sigma_{m,s}$ represent minimum yield and maximum equivalent strength of sth component, respectively.

The overall safety factor of a rotor k_{SF} is defined as the minimum value of the safety factors of all components:

$$k_{SF} = \min(k_{SF,s}) \tag{4.2}$$

Under the assumption that the stress is proportional to the square of rotation speed, the relationship between safety factor and rotation speed is given in Fig. 4.5. According to [136], the safety factor of a rotor should be higher than 2 marked by the dotted line in Fig. 4.5.
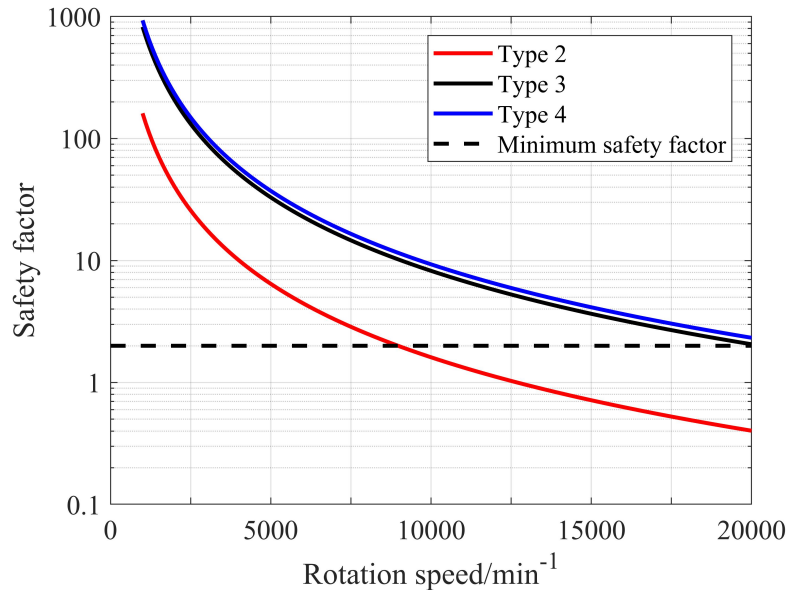
Fig. 4.5 Safety factor of three motors vs. speed.

The conclusion can then be drawn, that both Types 3 and 4 have sufficient mechanical strength in the whole speed range, while Type 2 does not meet the requirements. In the following sections, Types 3 and 4 will be further discussed, while Type 2 will be no more considered.

4.3   Demagnetization Analysis

In this thesis, the permanent magnet material Y30BH is utilized. Its demagnetization characteristics are presented in Fig. 4.6. Ferrite magnets have lower resilience to demagnetization than rare-earth magnets. Another difference to rare-earth magnets is that they have a positive temperature coefficient of intrinsic coercivity, which means the worst situation of ferrite magnets for demagnetization is at the lowest operation temperature. Considering that the motors are designed for home appliances, 0 °C is set as the lowest temperature for demagnetization analysis. In this section, a double-layer winding is used. The analyses are carried out by using Ansys Electronics Desktop.
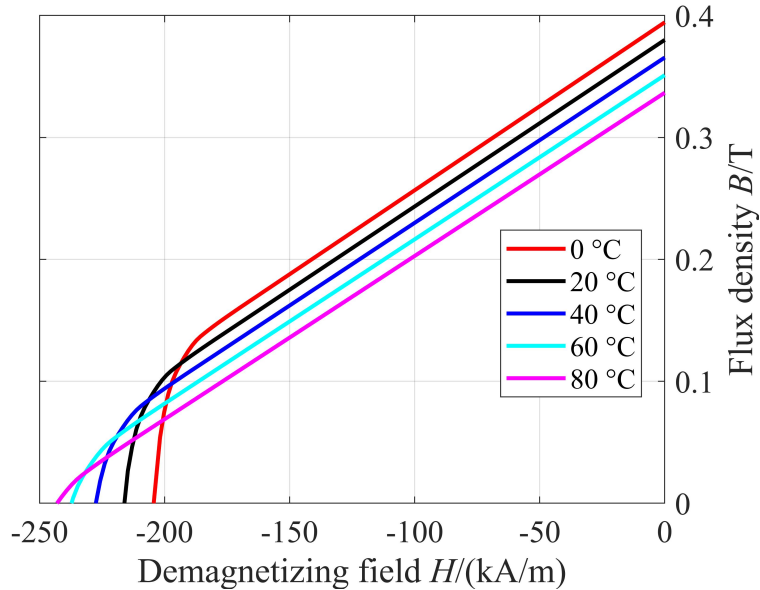
Fig. 4.6   Normal B-H curve of Y30BH at different temperatures.

Fig. 4.7 gives a description of recoil curve and new remanence after irreversible demagnetization, where solid and dotted lines represent original and recoil curves. B_r and $B_r^{'}$ represent original remanence and new remanence after irreversible demagnetization. (H_1, B_1) represents the operating point with maximum demagnetizing current. It should be emphasized that only the components in the demagnetizing direction should be taken into account when calculating H_1 and B_1.

Recoil curve can be expressed as:

$$B_1 = \mu_{rp} \cdot \mu_0 \cdot H_1 + B_r^{'} \tag{4.3}$$
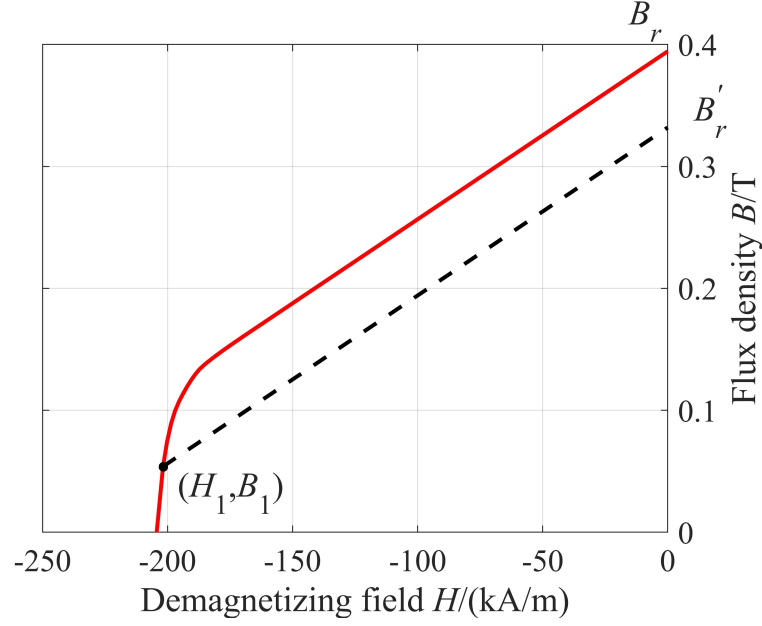
Fig. 4.7 Recoil curve and new remanence after irreversible demagnetization.

where μ_0 is vacuum permeability, μ_{rp} is relative permeability of magnets, and the value of $\mu_{rp} \cdot \mu_0$ corresponds to gradient of the tangent at $H = 0$ in the normal B-H curve. The new remanence point B'_r can then be derived as:

$$B'_r = B_1 - \mu_{rp} \cdot \mu_0 \cdot H_1 \tag{4.4}$$

The demagnetization ratio is defined by the decrease of no load EMF after application of a demagnetizing current:

$$k_{demag,-Id} = \frac{E_{0,0} - E_{0,-Id}}{E_{0,0}} \tag{4.5}$$

in which $E_{0,0}$ and $E_{0,-Id}$ represent no load EMFs before and after application of a demagnetizing current $-I_d$, $k_{demag,-Id}$ represents the corresponding demagnetization ratio.

The calculation in Ansys Electronics Desktop consists of three steps:

- The first step calculates the no load EMF without demagnetizing current.

- The second step simulates a reference model with application of a demagnetizing current $-I_d$. The new characteristic of magnets considering irreversible demagnetization is determined.

- The third step calculates the no load EMF after demagnetization by using the data from the reference model.

For Types 3 and 4, different demagnetizing currents were applied, and the results are given in Fig. 4.8. In this thesis, the limit of demagnetization ratio is set to 1% [183],

which is marked by the dotted line in Fig. 4.8. Considering a demagnetizing current limit of 200% of the maximum stator current in healthy condition, Type 3 has sufficient resilience to demagnetization, whereas Type 4 needs modifications.
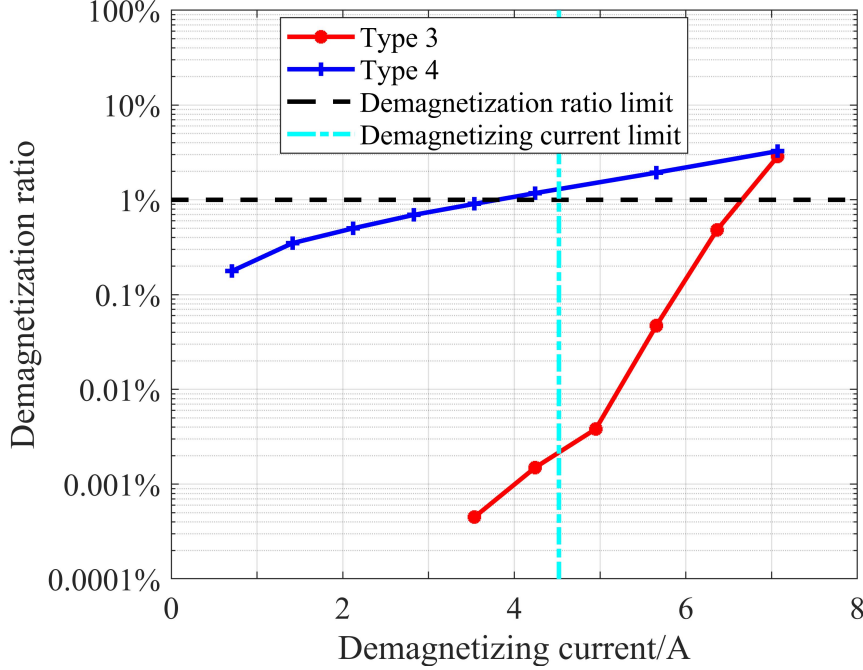
Fig. 4.8 Irreversible demagnetization ratio vs. demagnetization current for Types 3 and 4 at 0 °C.

From Fig. 4.4, an explanation of the poor resilience to demagnetization of Type 4 can be made as follows: in order to reduce flux leakage in the inner ring, the bridges connecting iron poles and inner ring are highly saturated. When a demagnetizing current is applied, a part of the flux produced by the current is forced across the corner of the magnets. Then partial irreversible demagnetization occurs in these places.

By inserting additional flux barriers between the magnets and inner ring in Type 4, a new layout labeled Type 4c can be obtained as shown in Fig. 4.9.

Compared to Type 4, the resilience against demagnetization of Type 4c is significantly improved as presented in Fig. 4.10.

Based on the analyses above, both Types 3 and 4c have sufficient performance in aspects of irreversible demagnetization. To explain this, the distribution of flux density at no load for the two motors is given in Fig. 4.11. For Type 3, the maximum flux density in rotor core is not high because there is no inner ring. For Type 4c, the ferrite magnets are separated from the most saturated area by additional flux barriers. Both designs lead to low partial irreversible demagnetization.
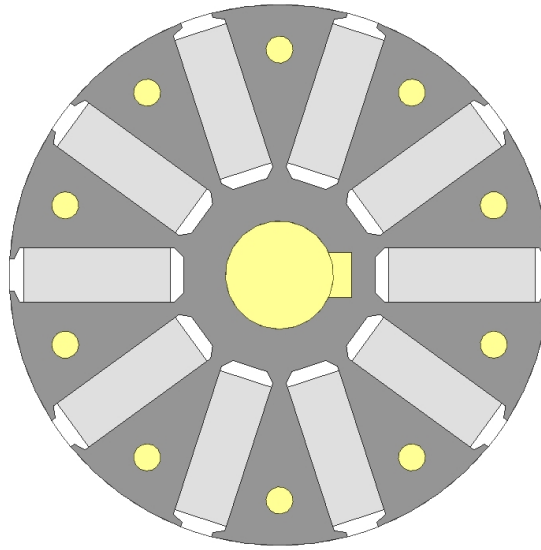
Fig. 4.9 Rotor layout of Type 4c.
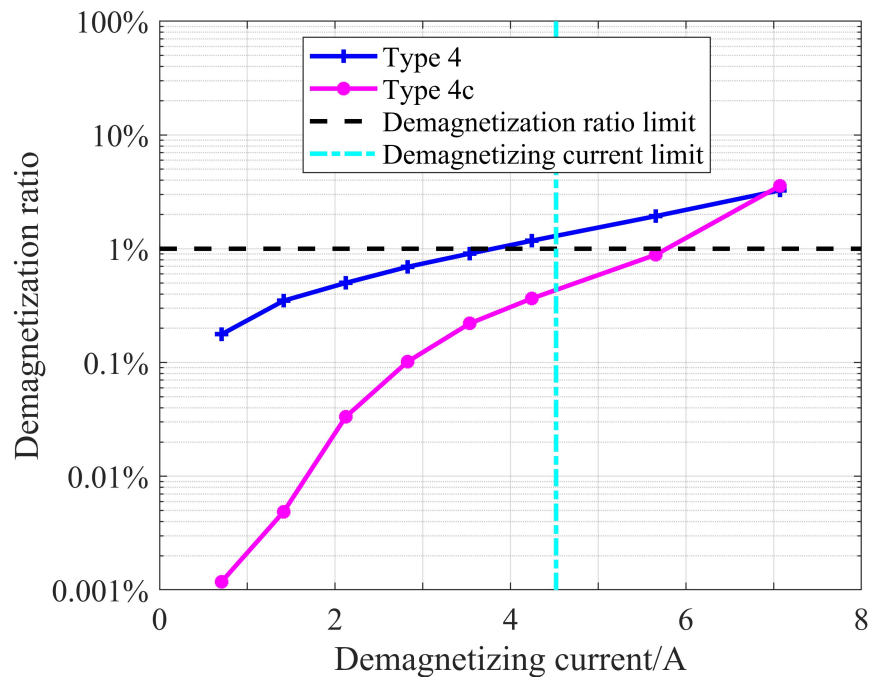
Fig. 4.10 Irreversible demagnetization ratio vs. demagnetization current for Types 4 and 4c at 0 °C.
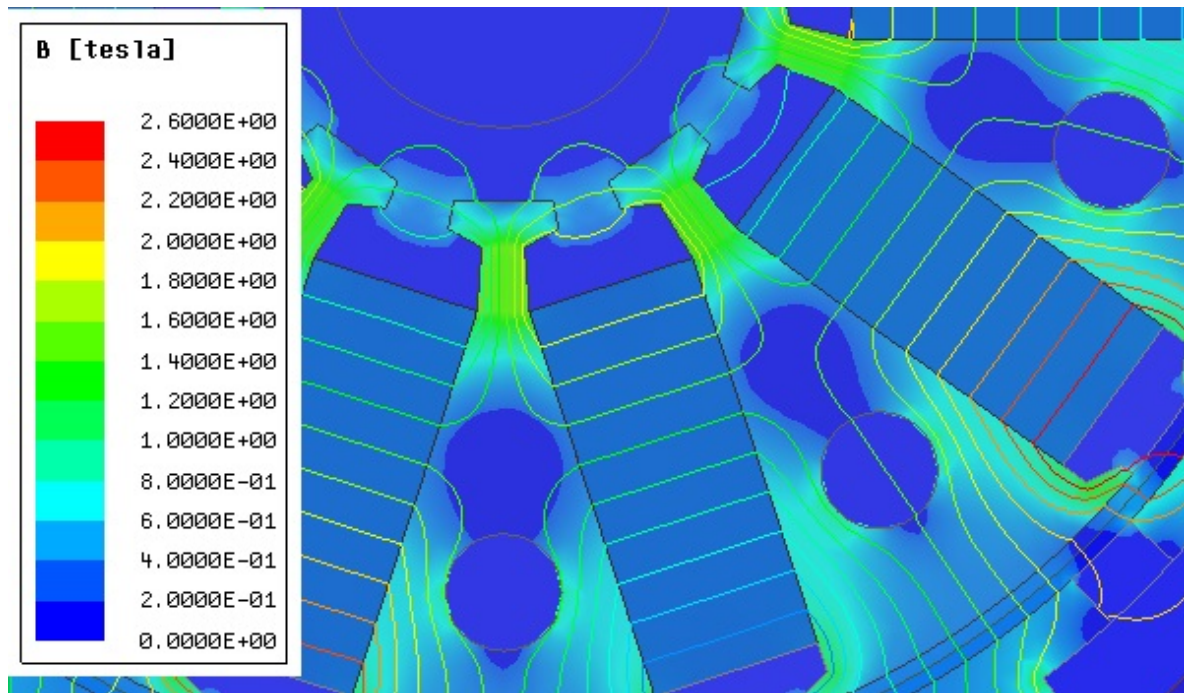
(a)
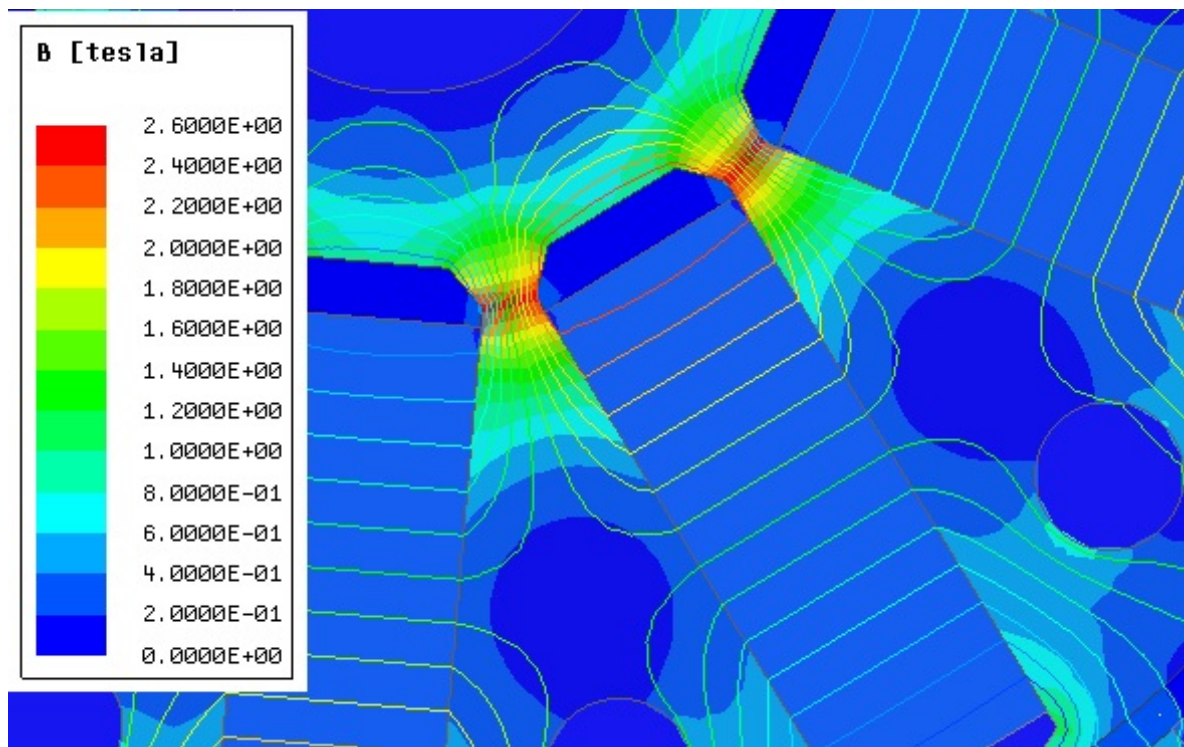
(b)

Fig. 4.11 Distribution of flux density at no load for Types 3 and 4c. (a) Type 3. (b) Type 4c.

4.4 Comparison of Single- and Double-layer Windings

In section 4.3, demagnetization characteristics of Types 3, 4, and 4c were investigated. To make fair comparison, double-layer windings were used for all of them. This section focuses on the differences of single- and double-layer windings. The rotor layout of Type 4c is utilized for both configurations. The following analyses have been carried out by using MATLAB and Ansys Electronics Desktop.

4.4.1 Introduction for Single- and Double-layer Windings

In this thesis, the 12-slot/10-pole configuration is used for spoke-type synchronous motors. The layouts of single- (SL) and double-layer (DL) windings are illustrated in Figs. 4.12(a) and 4.12(b), respectively. In the former, there is only one layer of coil sides in each slot, while there are two different ones in the latter [184]. Both have also been named alternate teeth and all teeth configurations [185].
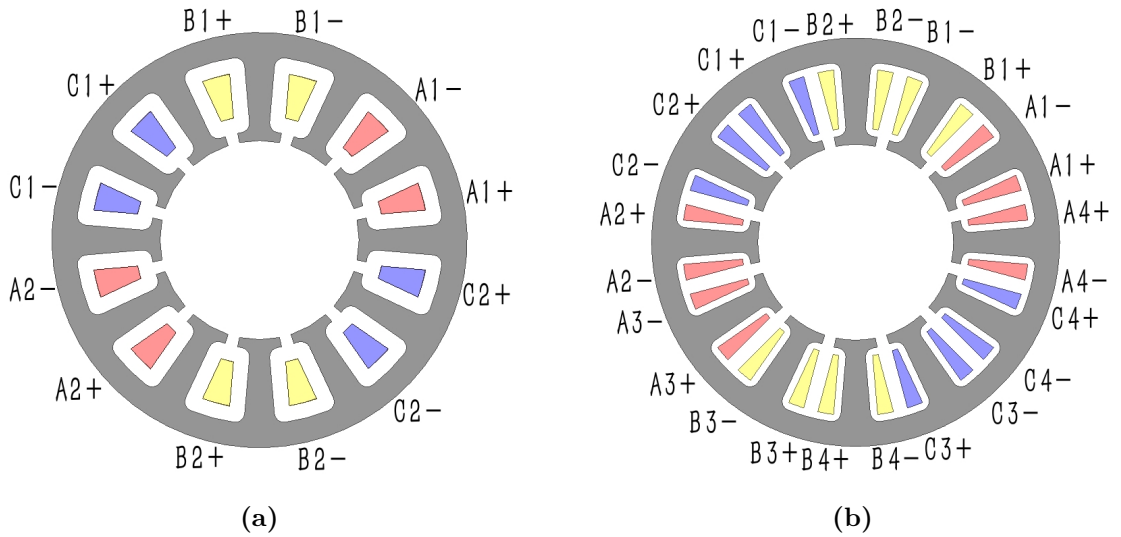
Fig. 4.12 Layouts of stator windings. (a) Single-layer configuration. (b) Double-layer configuration.

In practice, the fill factor of a single-layer winding can be higher than the one with double-layer configuration, because less layers of insulation are required. Moreover, there are only 6 coils in a single-layer winding. That is only half of a double-layer one, which means less production cost for the winding manufacturing process. It is essential to investigate the differences in performance of the two configurations considering that the motors discussed in this thesis are designed for home appliance applications, which are cost sensitive. If the differences turn out to be not critical, single-layer configuration would be selected.

In order to make a fair comparison, an equal motor configuration is maintained except the winding layout. The common configuration for the two motors is listed in Table 4.4. The number of turns of each coil in double-layer configuration is set to be half of the one in single-layer configuration, so that the total number of turns per phase is maintained throughout both designs.

Table 4.4   Common configuration

Parameter	Value
Number of phases	3
Number of poles	10
Number of slots	12
Number of conductors in each slot	144
Fill factor of slots	0.5
Outer diameter of stator stack	110 mm
Outer diameter of rotor stack	60 mm
Length of stator stack	50 mm
Length of rotor stack	50 mm
Length of air gap	1 mm
Height of magnets	6 mm
Width of magnets	16 mm
Diameter of shaft	12 mm

4.4.2   Analysis by Using Theory of Motor Windings

The double-layer winding mentioned above is equivalent to two sets of single-layer windings. The mechanical angle between them equals 150°.

Similar to the distribution factor defined to analyze MMF and EMF of distributed windings, a suppression factor is defined to describe the relationship between the winding factors of single- and double-layer windings:

$$k_{d,n} = |\frac{k_{w,DL,n}}{k_{w,SL,n}}| \tag{4.6}$$

where $k_{d,n}$ represents the suppression factor for the nth harmonic in a double-layer compared to a single-layer winding. $k_{w,SL,n}$ and $k_{w,DL,n}$ are the corresponding winding factors for single- and double-layer configurations. The space harmonic corresponding to $p = 1$ is defined as fundamental in order to avoid fractions when describing suppression and winding factors.

The suppression factor $k_{d,n}$ can be calculated as:

$$k_{d,n} = |\cos \frac{n \cdot p_h \cdot \alpha_{SL,m}}{2}| \tag{4.7}$$

where $\alpha_{SL,m}$ is the mechanical angle between two sets of single-layer windings, which equals 150° in this case, and p_h refers to the number of pole pairs of harmonic components.

Table 4.5 lists the results for $k_{d,n}$ for different orders of harmonics.

Table 4.5   Values of suppression factors

Order	Suppression factor $k_{d,n}$
1	0.259
5	0.966
7	0.966
11	0.259
etc.	...

Effects of using double-layer windings can be summarized as follows:

- The suppression factor of the 5th harmonic equals 0.966 resulting in a small torque reduction or a slight increase of required MMF compared to the single-layer winding.

- The suppression of the fundamental in a double-layer winding equal 0.259 and thus leads to a more sinusoidal MMF waveform and to lower partial irreversible demagnetization compared to a single-layer winding.

4.4.3   FEA at Operating Points

FE analyses have been carried out for 20 °C. As shown in Fig. 4.13, the no load EMF waveforms of both configurations are quite close to sinusoidal. As estimated in Section 4.4.2, the no load EMF of the double-layer configuration is slightly lower and less distorted.
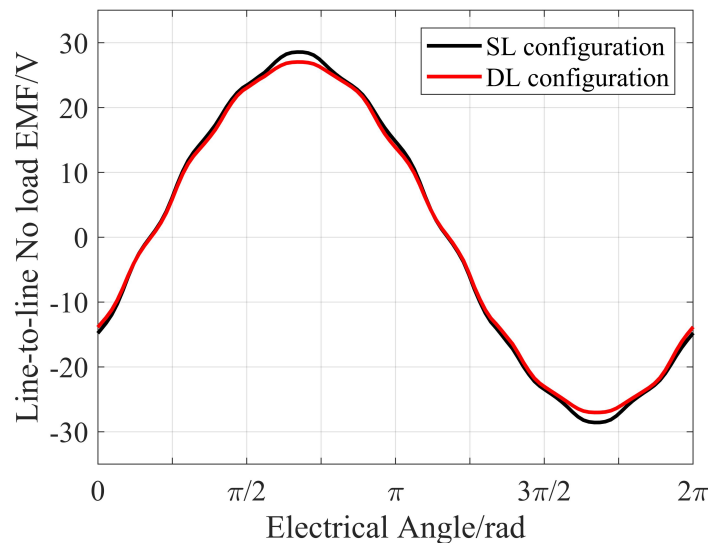
Fig. 4.13   Waveforms of line-to-line no load EMF at $550 \, \text{min}^{-1}$.

For the two operating points given in Table 3.1, the results of FEA are listed in Table 4.6. The curves of the output torque are illustrated in Fig. 4.14.

Table 4.6   FEA results of given operating points

Configuration	SL winding		DL winding	
Operating mode	washing	spinning	washing	spinning
Resistance/Ω	2.0		1.9	
Inductance in d-axis/H	0.024		0.017	
Inductance in q-axis/H	0.027		0.021	
Average torque/(N·m)	1.3	0.3	1.3	0.3
Torque ripple coefficient	3.0%	11.3%	1.2%	12.4%
Rotation speed/min^{-1}	550	16,600	550	16,600
Current, RMS value/A	2.16	1.48	2.26	1.70
Efficiency	71.7%	91.4%	71.5%	92.5%
Power factor	0.752	0.962	0.817	0.836
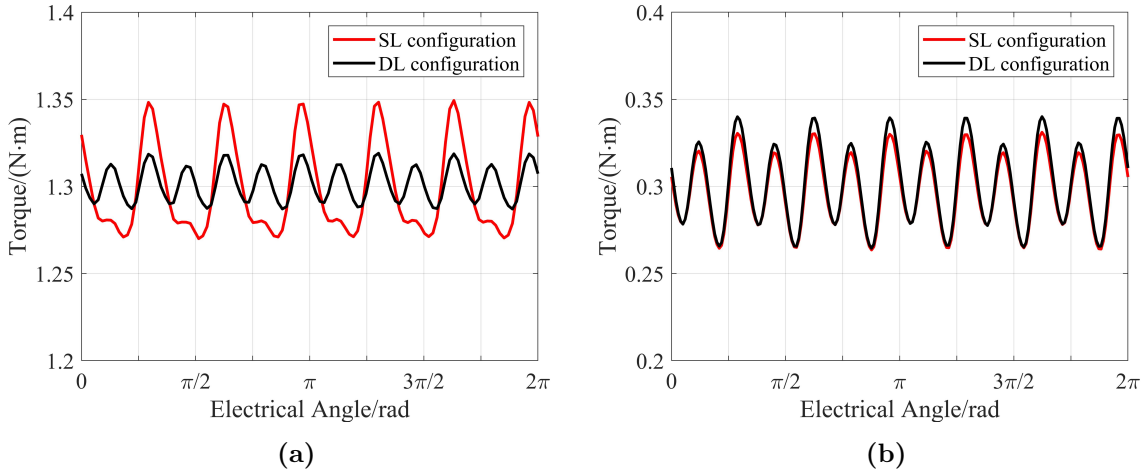
Fig. 4.14   Torque vs. Electrical angle. (a) Washing mode. (b) Spinning mode.

From Table 4.6 and Fig. 4.14, the following conclusions can be made when comparing double- to single-layer configuration:

- At both operating points, higher currents are required to obtain given torque for double-layer configuration, which can lead to more losses in converter. At high speed, this phenomenon is more significant than expected, which results from the reduction of harmonic leakage inductance.

- When using double-layer windings, efficiency does not decrease significantly despite of higher currents. Instead, it increases in spinning mode. This can be explained by a lower stator resistance caused by shorter end turns and lower iron losses caused by lower harmonic components.

- Torque ripple is significantly reduced in double-layer configuration in washing mode, while there is no significant difference in spinning mode.

4.4.4 Analysis of Irreversible Demagnetization

In Section 4.4.2, a prediction has been made that a single-layer winding configuration is more likely to have potential problems of irreversible demagnetization compared to a double-layer version. By using the method which has been presented in Section 4.3, a comparison of irreversible demagnetization has been carried out for both configurations. Fig. 4.15 shows, that the double-layer configuration has much better irreversible demagnetization performance.
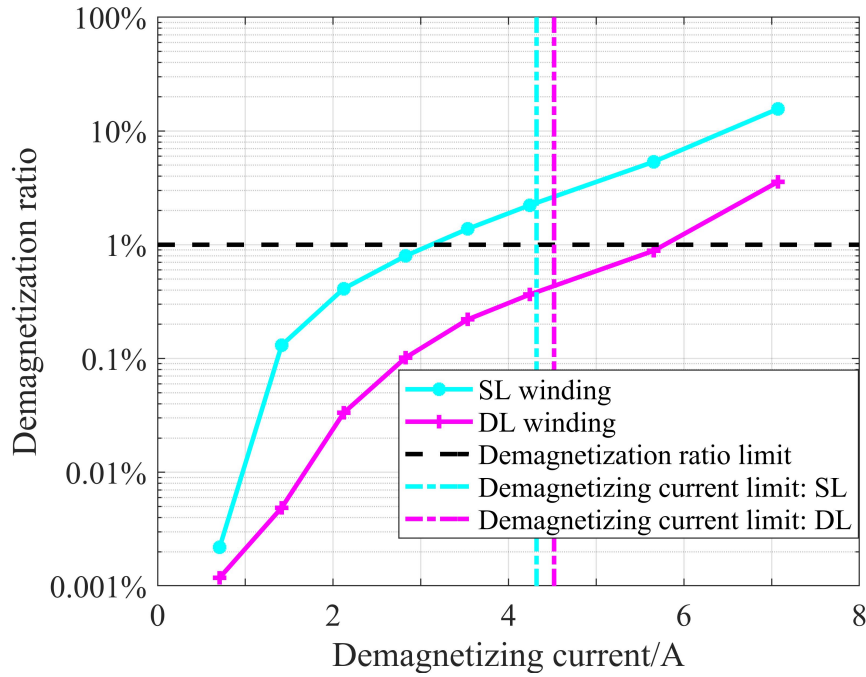
Fig. 4.15 Demagnetization ratio with different demagnetizing current for single- and double-layer configurations.

For a better explanation of this result, the loss of remanence in both healthy and overcurrent conditions has been calculated as shown in Fig. 4.16. In healthy condition, the demagnetizing current of operating point 2 has been used. In overcurrent condition, it has been set to double of the RMS value of the total stator current at operating point 1.

According to Fig. 4.16, partial irreversible demagnetization at the corners of the magnets is more serious in single-layer configuration in both healthy and overcurrent conditions compared to the one of double-layer configuration.
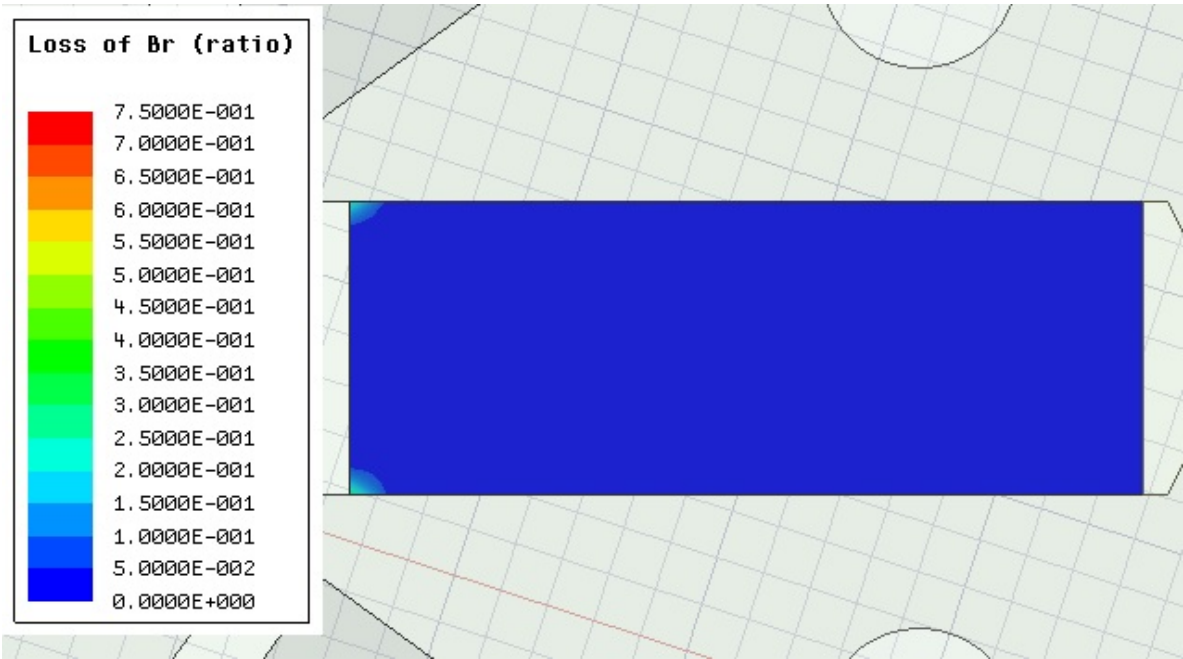
(a)
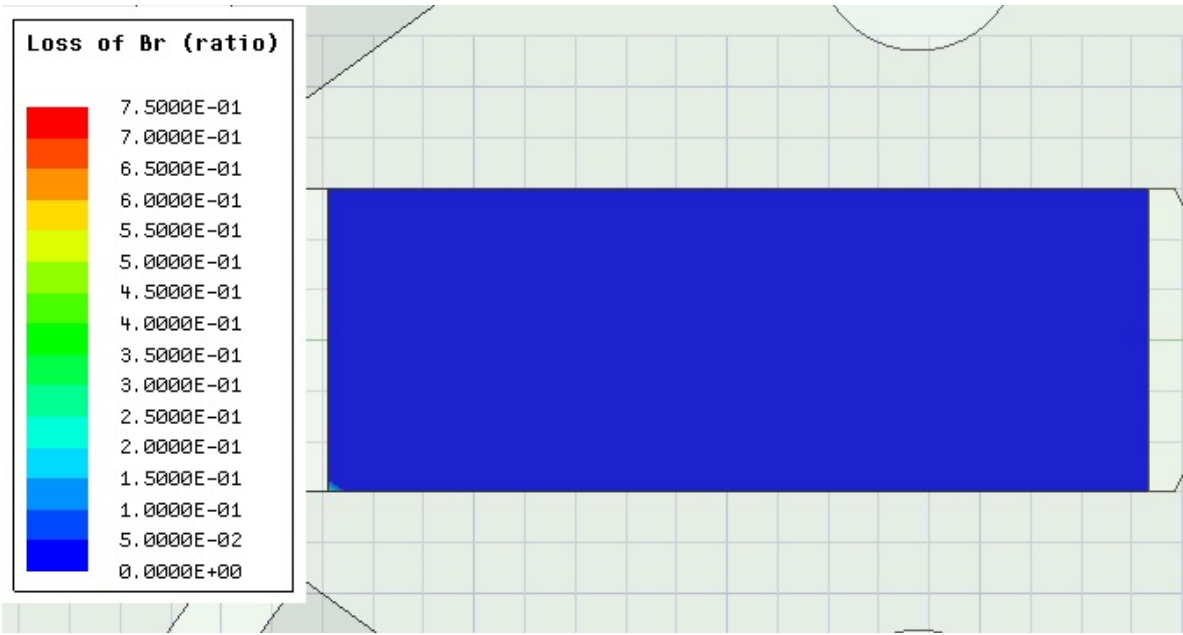
(b)

Fig. 4.16 Distribution of loss of remanence in magnets after irreversible demagnetization. (To be continued)

.
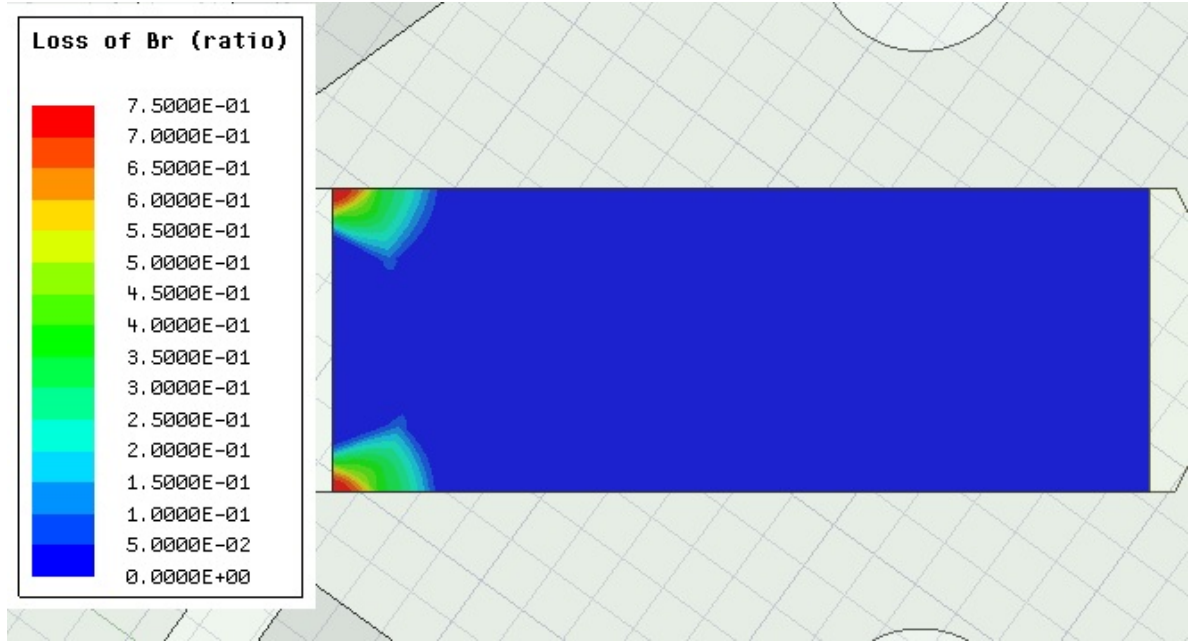
(c)
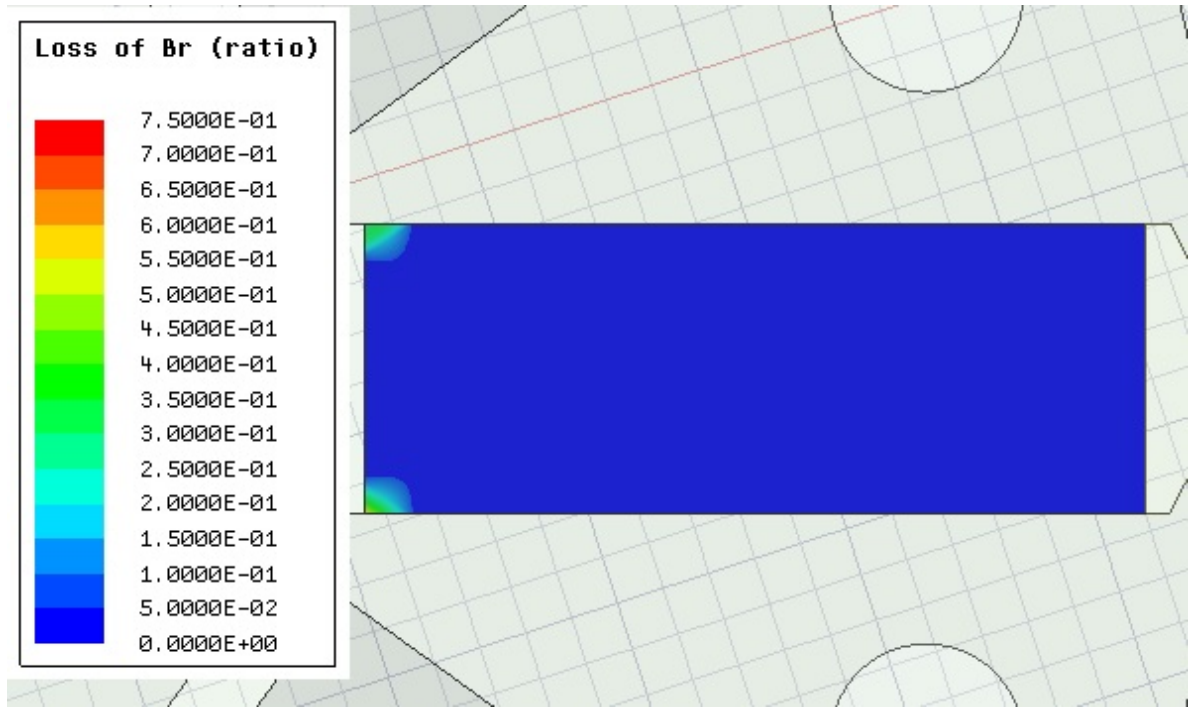
(d)

Fig. 4.16 Distribution of loss of remanence in magnets after irreversible demagnetization. (a) Single-layer version with $I_d = -1.38\,\mathrm{A}$. (b) Double-layer version with $I_d = -1.63\,\mathrm{A}$. (c) Single-layer version with $I_d = -4.32\,\mathrm{A}$. (d) Double-layer version with $I_d = -4.52\,\mathrm{A}$.

4.4.5 Summary

The comparison of single- and double-layer windings can be summarized. For double-layer configuration:

- The manufacturing is more difficult. The maximum fill factor in stator slots is lower.

- Higher stator currents are required at given operating points due to its lower winding factor.

- Double-layer configuration is more efficient, especially in spinning mode. This is due to its shorter end turns and less harmonic components.

- Torque ripple in washing mode is reduced, while there is no significant difference in spinning mode.

- The resilience against demagnetization is much higher, which is caused by a lower harmonic in MMF waveform corresponding to $p = 1$.

Generally speaking, irreversible demagnetization is the most serious issue in this case. As shown in Fig. 4.15, the single-layer configuration cannot provide sufficient safety against irreversible demagnetization. In the final design, a double-layer winding is used.

Demagnetization analysis shows an interesting result that double-layer configuration is superior to single-layer configuration with the motor specifications used in this thesis. It should be noted that this conclusion cannot be extended to all fractional-slot concentrated windings directly. The results however at least indicate that it is necessary to take irreversible demagnetization into consideration and make a trade-off between performance of irreversible demagnetization, easiness of manufacturing and other aspects when making decisions between single- and double-layer windings.

4.5   Discussion of Motor With Longer Rotor Stack

There is more space for the length of a rotor stack than a corresponding stator stack. In this situation, it is possible to extend the rotor stack axially without increasing the size of the whole motor. This technique is often used for flux concentration in small motors. In this section, the effect of using longer rotor stack is investigated.

4.5.1   Analysis by Using a 2D Analytical Method

Fig. 4.17 presents a 2D model for analytical calculation with the following conditions:

- Only the radial direction and the axial direction are considered in the model as the 3D model of the motor can be regarded as rotationally symmetric. Model length in tangential direction is labeled l_t, which actually makes no difference in the analysis.

- Stator stack and rotor stack have an infinite permeability, while the air gap has a permeability of μ_0.
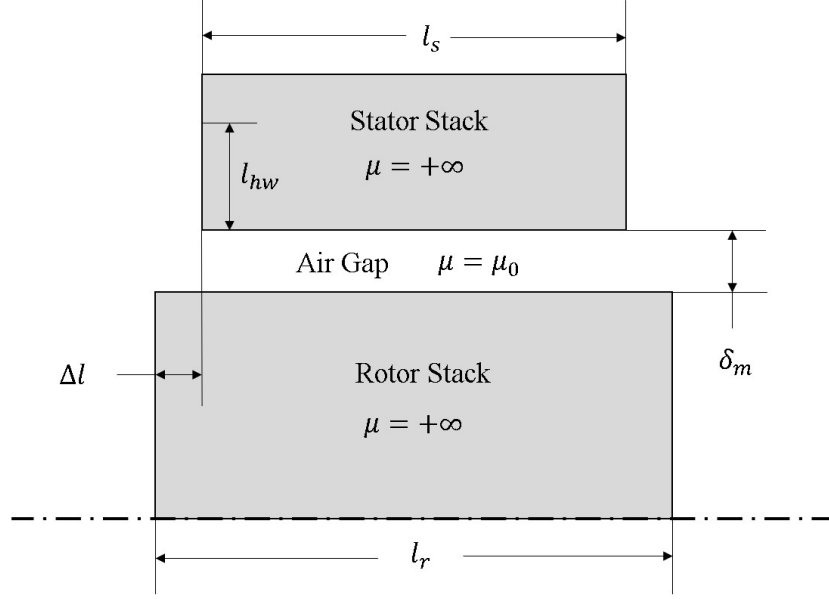
Fig. 4.17 Model used for analytical analysis.

- The effect of permanent magnets is simplified to an MMF source between air gap and rotor stack with the symbol F_p.

- Only the no load condition is discussed, which means there is no MMF produced by stator currents.

- Lengths of stator stack, rotor stack, and end region of each side are named l_s, l_r, and Δl, respectively. A modified air gap length δ_m is used to model the effect of air gap length and PM thickness.

- l_{hw} represents average depth of all conductors, which corresponds to the length of the integral path in end region.

Conformal transformation can be used to achieve a precise analytical solution, which is however complex and time consuming. In order to simplify the calculation, the flux lines in air gap and end regions are simplified to rectangular and ring-shaped segments. The value of magnetic field strength is assumed to be constant along each flux line. The concerned regions, including end regions and air gap, are divided into 3 regions according to the patterns of approximate flux lines as illustrated in Figs. 4.18 and 4.19.

First of all, an end factor k_{end} is defined as the ratio of magnetic energy of models considering and neglecting end effects, which are labeled $E_{m,3D}$ and $E_{m,2D}$:

$$k_{end} = \frac{E_{m,3D}}{E_{m,2D}} \tag{4.8}$$

where $E_{m,2D}$ can be expressed as:

$$E_{m,2D} = \frac{\mu_0 \cdot l_r \cdot l_t \cdot F_p^2}{2 \cdot \delta_m} \tag{4.9}$$
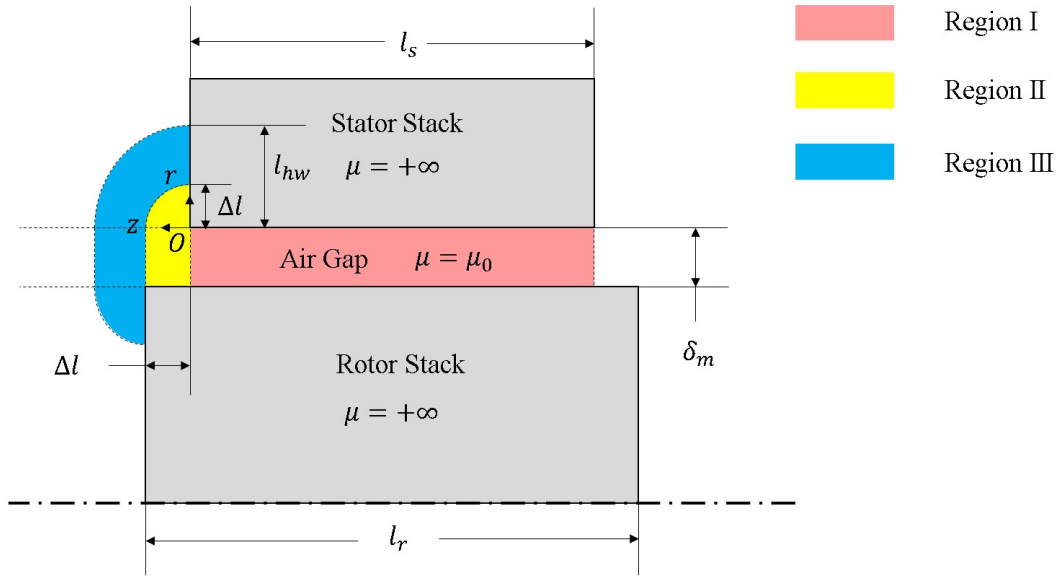
Fig. 4.18   Illustration of different regions.
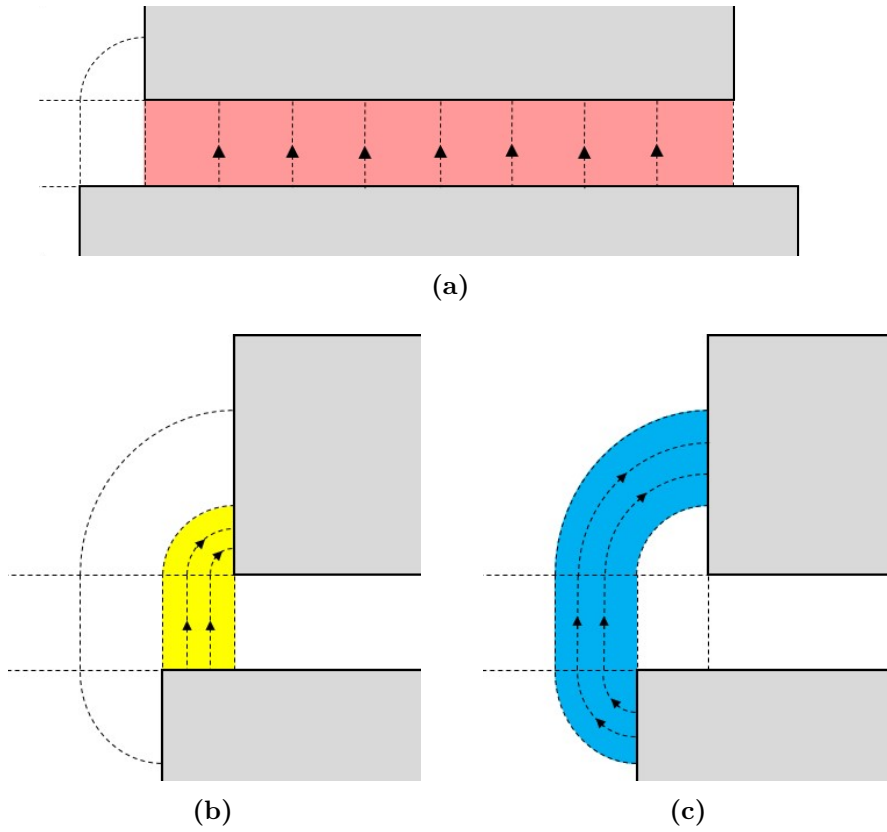
Fig. 4.19   Approximate flux lines. (a) Region I. (b) Region II. (c) Region III.

$E_{m,3D}$ can be expressed as:

$$E_{m,3D} = E_{m1} + 2 \cdot (E_{m2} + E_{m3}) \tag{4.10}$$

where E_{m1}, E_{m2}, and E_{m3} correspond to magnetic energy in region I, II, and III, respectively.

The modified air gap length δ_m can be expressed as:

$$\delta_m = \frac{\delta}{k_\delta} + \frac{\delta_p}{\mu_{rp}} \tag{4.11}$$

where δ is the air gap length, k_δ is the Carter's coefficient, and μ_{rp} is the relative permeability of magnets. For SPM motors, δ_p is the thickness of magnets, while it equals 0 for IPM motors.

In the following analysis, each flux line is represented by the location of its end point. In region I, the magnetic field strength H_{r1} can be calculated as:

$$H_{r1}(z) = \frac{F_p}{\delta_m} \tag{4.12}$$

The relationship between l_r, l_s and Δl can be written as:

$$l_s = l_r - 2 \cdot \Delta l \tag{4.13}$$

The magnetic energy in region I can then be figured out:

$$
\begin{aligned}
E_{m,1} &= \frac{1}{2} \cdot \mu_0 \cdot l_t \cdot \delta_m \cdot \int_{-l_s}^{0} H_{r1}^2(z)\,\mathrm{d}z \\
&= \frac{1}{2} \cdot \mu_0 \cdot l_t \cdot \delta_m \cdot (\frac{F_p}{\delta_m})^2 \cdot l_s \\
&= \frac{\mu_0 \cdot l_s \cdot l_t \cdot F_p^2}{2 \cdot \delta_m} \\
&= \frac{\mu_0 \cdot (l_r - 2 \cdot \Delta l) \cdot l_t \cdot F_p^2}{2 \cdot \delta_m}
\end{aligned}
\tag{4.14}
$$

When $0 < \Delta l < l_{hw}$, both regions II and III exist. In region II, the magnetic field strength H_{r2} can be calculated as:

$$H_{r2}(r) = \frac{F_p}{\frac{\pi}{2} \cdot r + \delta_m} \tag{4.15}$$

The magnetic energy in region II can then be figured out:

$$
\begin{aligned}
E_{m,2} &= \frac{1}{2} \cdot \mu_0 \cdot l_t \cdot \int_0^{\Delta l} (\frac{\pi}{2} \cdot r + \delta_m) H_{r2}^2(r)\,\mathrm{d}r \\
&= \frac{1}{2} \cdot \mu_0 \cdot l_t \cdot \int_0^{\Delta l} \frac{F_p^2}{\frac{\pi}{2} \cdot r + \delta_m}\,\mathrm{d}r \\
&= \frac{1}{2} \cdot \mu_0 \cdot l_t \cdot \frac{2}{\pi} \cdot F_p^2 \cdot \int_0^{\Delta l} \frac{1}{r + \frac{2 \cdot \delta_m}{\pi}}\,\mathrm{d}r \\
&= \frac{1}{\pi} \cdot \mu_0 \cdot l_t \cdot F_p^2 \cdot \ln(1 + \frac{\pi \cdot \Delta l}{2 \cdot \delta_m})
\end{aligned}
\tag{4.16}
$$

In region III, the magnetic field strength H_{r3} can be calculated as:

$$H_{r3}(r) = \frac{F_p}{\pi \cdot r - \frac{\pi}{2} \cdot \Delta l + \delta_m} \tag{4.17}$$

The magnetic energy in region III can then be figured out:

$$\begin{aligned}
E_{m,3} &= \frac{1}{2} \cdot \mu_0 \cdot l_t \cdot \int_{\Delta l}^{l_{hw}} (\pi \cdot r - \frac{\pi}{2} \cdot \Delta l + \delta_m) \cdot H_{r3}^2(r) \, dr \\
&= \frac{1}{2} \cdot \mu_0 \cdot l_t \cdot \int_{\Delta l}^{l_{hw}} \frac{F_p^2}{\pi \cdot r - \frac{\pi}{2} \cdot \Delta l + \delta_m} \, dr \\
&= \frac{1}{2} \cdot \mu_0 \cdot l_t \cdot \frac{1}{\pi} \cdot F_p^2 \int_{\Delta l}^{l_{hw}} \frac{1}{r - \frac{\Delta l}{2} + \frac{\delta_m}{\pi}} \, dr \\
&= \frac{1}{2\pi} \cdot \mu_0 \cdot l_t \cdot F_p^2 \cdot \ln(1 + 2\pi \cdot \frac{l_{hw} - \Delta l}{\pi \cdot \Delta l + 2 \cdot \delta_m})
\end{aligned} \tag{4.18}$$

From (4.8), (4.9), (4.10), (4.14), (4.16), and (4.18), the end factor with the condition $0 < \Delta l < l_{hw}$ can be calculated as:

$$k_{end} = 1 - \frac{2 \cdot \Delta l}{l_r} + \frac{2 \cdot \delta_m}{\pi \cdot l_r}[2 \cdot \ln(1 + \frac{\pi \cdot \Delta l}{2 \cdot \delta_m}) + \ln(1 + 2\pi \cdot \frac{l_{hw} - \Delta l}{\pi \cdot \Delta l + 2 \cdot \delta_m})] \tag{4.19}$$

When $\Delta l = 0$, region II does not exist. The magnetic energy in region III can still be calculated as in (4.18). Thus (4.19) can still be used to calculate end factor.

When $\Delta l \geq l_{hw}$, region III does not exist. The magnetic energy in region II can be calculated as:

$$\begin{aligned}
E_{m,2} &= \frac{1}{2} \cdot \mu_0 \cdot l_t \cdot \int_0^{l_{hw}} (\frac{\pi}{2} \cdot r + \delta_m) \cdot H_{r2}^2(r) \, dr \\
&= \frac{1}{2} \cdot \mu_0 \cdot l_t \cdot \int_0^{l_{hw}} \frac{F_p^2}{\frac{\pi}{2} \cdot r + \delta_m} \, dr \\
&= \frac{1}{2} \cdot \mu_0 \cdot l_t \cdot \frac{2}{\pi} \cdot F_p^2 \cdot \int_0^{l_{hw}} \frac{1}{r + \frac{2 \cdot \delta_m}{\pi}} \, dr \\
&= \frac{1}{\pi} \cdot \mu_0 \cdot l_t \cdot F_p^2 \cdot \ln(1 + \frac{\pi \cdot l_{hw}}{2 \cdot \delta_m})
\end{aligned} \tag{4.20}$$

The magnetic energy in region II can be expressed as:

$$E_{m3} = 0 \tag{4.21}$$

The end factor with the condition $\Delta l \geq l_{hw}$ can be calculated as:

$$k_{end} = 1 - \frac{2 \cdot \Delta l}{l_r} + \frac{4 \cdot \delta_m}{\pi \cdot l_r} \cdot \ln(1 + \frac{\pi \cdot l_{hw}}{2 \cdot \delta_m}) \tag{4.22}$$

In summary, the end factor can be expressed as:

$$k_{end} = \begin{cases} 1 - \dfrac{2 \cdot \Delta l}{l_r} + \dfrac{2 \cdot \delta_m}{\pi \cdot l_r} \cdot [2 \cdot \ln(1 + \dfrac{\pi \cdot \Delta l}{2 \cdot \delta_m}) + \ln(1 + \dfrac{2\pi \cdot (l_{hw} - \Delta l)}{\pi \cdot \Delta l + 2 \cdot \delta_m})], 0 \le \Delta l < l_{hw} \\ 1 - \dfrac{2 \cdot \Delta l}{l_r} + \dfrac{4 \cdot \delta_m}{\pi \cdot l_r} \cdot \ln(1 + \dfrac{\pi \cdot l_{hw}}{2 \cdot \delta_m}), \qquad\qquad\qquad\qquad \Delta l \ge l_{hw} \end{cases}$$

$$(4.23)$$

The value of k_{end} is closely related to the value of l_{hw}, which is however difficult to be determined precisely in practice. The end factor only considering the effects of regions I and II is labeled k_{end1} and calculated as:

$$k_{end1} = 1 - \frac{2 \cdot \Delta l}{l_r} + \frac{4 \cdot \delta_m}{\pi \cdot l_r} \cdot \ln(1 + \frac{\pi \cdot \Delta l}{2 \cdot \delta_m}) \tag{4.24}$$

4.5.2 Analysis by Using 2D FEM

The model presented in Fig. 4.17 can also be solved by using 2D FEM. Using the duality between static magnetic field and static current field, a DC current flow model is established instead of a magnetostatic one. Different values of impressed electric potentials are applied to the red lines directly in Fig. 4.20. In order to simulate infinite conductivity, its value was increased until the results stopped changing.

Fig. 4.20 Model for 2D FEA.

The results of k_{end1} are given in Fig. 4.21, which show good consistency between FEM and analytical method. Because the effects of region III were not considered, k_{end1} equals 1 when the lengths of stator and rotor stacks are the same.

Fig. 4.21 Results of end factor by using FEM and analytical method.

4.5.3 Analysis by Using 3D FEM

In order to validate the calculation and analysis in Section 4.5.1 and Section 4.5.2, further simulations were made by using 3D FEM in Ansys Electronics Desktop. 3D models of a surface-mounted permanent magnet (SPM) motor and a spoke-type motor with different lengths of stator and rotor stacks were set up as shown in Figs. 4.22 and 4.23. The former is close to the model discussed in Sections 4.5.1 and 4.5.2 when a modified air gap length δ_m is used. The latter is based on the specifications of the spoke-type synchronous motor used in this thesis.
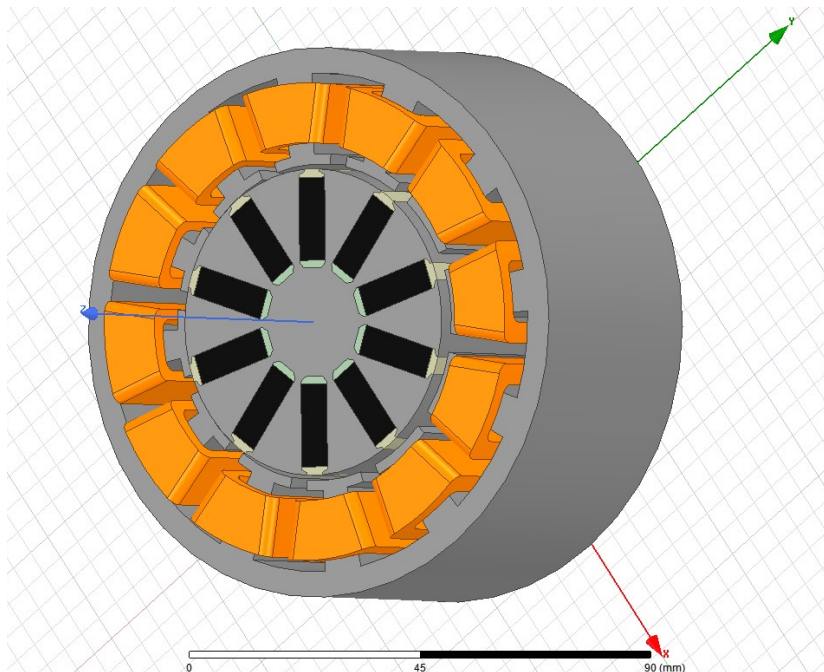
Fig. 4.23 3D model of a spoke-type motor with longer rotor stack.
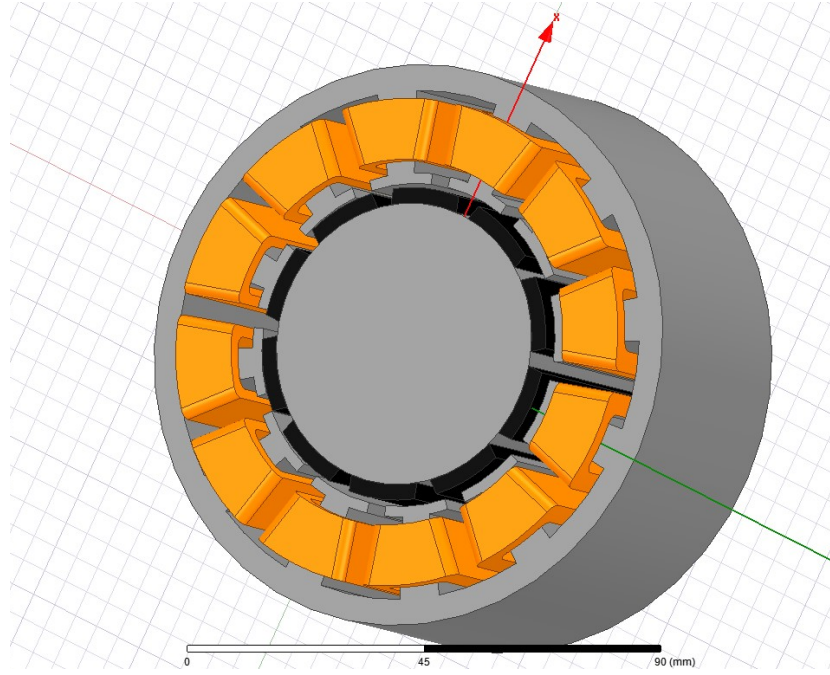
Fig. 4.22   3D model of a surface-mounted permanent magnet motor with longer rotor stack.

For different configurations, average torque has been calculated with given stator currents.   Average torque has also been analytically estimated from results of configurations with the same length of stator and rotor stacks by using k_{end} or k_{end1}. Details are listed in Table 4.7.

Table 4.7   Dimensions and torque for 3D models

Motor	SPM			Spoke		
Operating point	$I_d = 0\,\text{A}, I_q = 1.41\,\text{A}$			$I_d = -0.37\,\text{A}, I_q = 2.20\,\text{A}$		
Number	1	2	3	4	5	6
Length of rotor stack/mm	50	51	52	50	51	52
Length of stator stack/mm	50	49	48	50	49	48
Calculated torque by 3D FEM/(N·m)	0.7618	0.7692	0.7728	1.2570	1.2586	1.2618
Predicted torque by k_{end}/(N·m)	——	0.7673	0.7718	——	1.2655	1.2707
Predicted torque by k_{end1}/(N·m)	——	0.7757	0.7875	——	1.2756	1.2872

In Table 4.7, the results by using k_{end} are better than those by using k_{end1}. This is caused by not considering region III when calculating k_{end1}. When using k_{end}, it can

also be observed that the results match quite well for SPM motors, while the difference between them is larger for spoke-type motors. A possible explanation is, that the model of a SPM motor is close to the one used in analytical analysis and 2D FEA, while a complex spoke-type motor with highly saturated bridges is difficult to simplify for analytical modeling.

4.5.4 Summary

The results on rotor stack extension can be summarized as follows:

- The end factor k_{end} calculated in (4.23) can be used to analyze motors with shorter stator stacks. It is more precise for SPM motors than for spoke-type motors.

- For the two examples in this section, the estimation using k_{end1} calculated in (4.24) is less precise than the one using k_{end}.

- Average lengths of stator and rotor stacks can be used in an approximate calculation.

- When stator windings have long end turns, there is some more space for length of rotor stack without increasing the total motor length. In this case torque density can be increased by utilizing a longer rotor stack.

- A longer rotor stack will not be utilized in the final design considering that the distance between two bearings must be limited to ensure mechanical reliability at high speed.

4.6 Final Design

4.6.1 Configuration of the Final Design

According to the analyses in this chapter, the final design of a spoke-type synchronous motor can be formed step by step. Considering manufacturing convenience, mechanical stability at high speed, and resilience against demagnetization, the rotor layout of Type 4c was selected. A double-layer winding was chosen. In order to limit flexural vibration, stator and rotor core lengths are equal. The diameter of each conductor without insulation is 0.8 mm in the original design. In order to make the winding process more convenient, two conductors in parallel with a diameter of 0.56 mm each were used. Details are listed in Table 4.8.

Table 4.8   Motor specifications of the final design

Motor type	Spoke-type synchronous motor
Rotor layout	Type 4c
Non-magnetic shaft	no
Non-magnetic hub	no
Stator windings	double-layer windings
Number of phases	3
Number of slots	12
Number of poles	10
Outer diameter of stator stack	110 mm
Outer diameter of rotor stack	60 mm
Length of stator stack	50 mm
Length of rotor stack	50 mm
Width of air gap	1 mm
Magnet material	Y30BH
Height of magnet	6 mm
Width of magnet	16 mm
Diameter of conductor	0.56 mm
Number of conductors in parallel	2
Number of turns per each coil	72
Diameter of shaft	12 mm

Some analyses of the final design have been carried out in the former sections in this chapter. The 2D FEA of the final design at given operating points has already been done in Section 4.4.3. The results can be found in Fig. 4.13, Fig. 4.14, and Table 4.6 (DL winding). The analysis of irreversible demagnetization for the final design has been carried out in Section 4.4.4, and the results can be found in Figs. 4.15 and 4.16 (DL winding). Mechanical analysis of the final design will be carried out in the following part of this chapter.

4.6.2   Mechanical Analysis

The results of the 3D mechanical analysis for the final design are presented in Fig. 4.24. The corresponding details of each component are listed in Table 4.9. The results show that the final design has a safety factor above 2 in whole speed range.

Table 4.9   Results of mechanical analysis of the final design by using 3D FEM

Component	Material	Von Mises stress/MPa	Yield strength/MPa	Safety factor
Shaft	S235JR	2.4	235	97.9
Bolts	S235JR	95.6	235	2.46
Stack	M270-35A	151.1	355-450	2.35
End ring	AA7075	48.8	360-470	7.38
PM	Y30BH	15.2	34 (tensile strength)	2.24
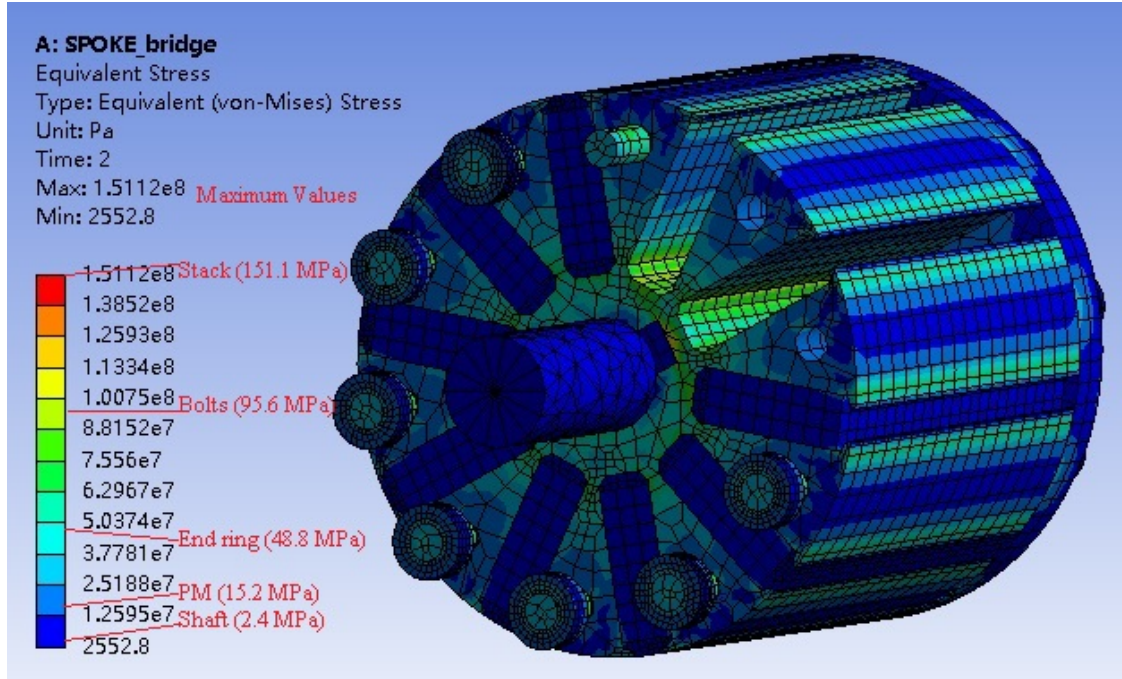
Fig. 4.24   Distribution of von Mises stress of the final design at 20,000 min^{-1}.

4.6.3   Thermal Analysis

In order to avoid overheat in operation, transient thermal analysis of the final design has also been carried out by using 3D FEM. The model is simplified as follows:

- Copper bars represent the stator winding in slots and end turns. The cross-sectional area of these bars equals the corresponding one of conductors in the motor. Fig. 4.25 shows details of copper bars and end turns. The space between stator stack and copper bars is filled with insulation material. Better results can be obtained by using a more complex winding model, e.g. the one with several layers of conductors and insulation [186], which is however not used in this thesis because of the limit of the computation platform.

- Radiation and convection conditions are applied to outer surfaces. By using the Nusselt number, convection in air gap is simplified to the situation with only conduction [187, 188].
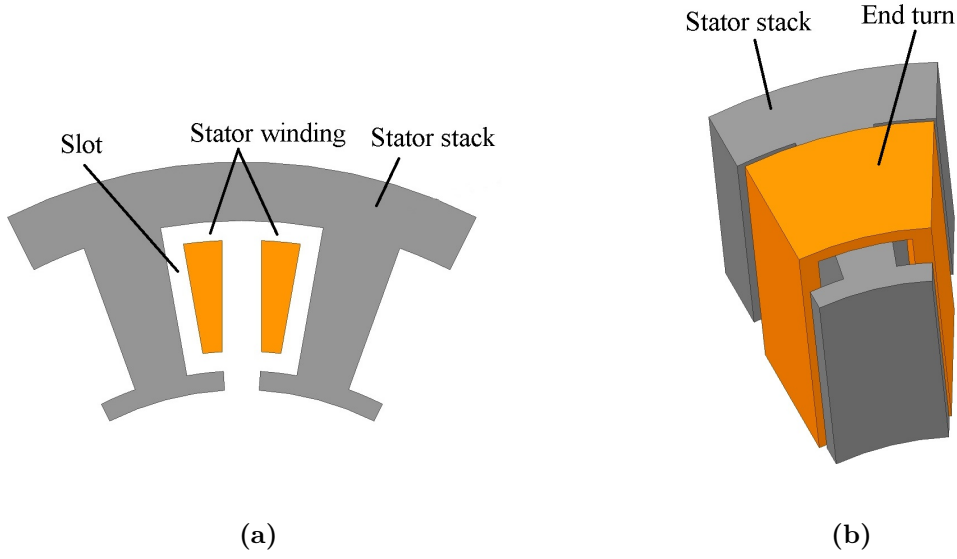
Fig. 4.25 Copper bars representing stator winding in a slot and end turns. (a) Stator winding in a slot. (b) End turn.

- Different inner heat sources are used to represent motor losses distributed evenly in copper bars and stator stack. Mechanical friction and windage losses are applied evenly in the rotor stack.

- The ambient temperature and the initial state of all components equal 40 °C. When calculating copper losses, a copper resistivity at 80 °C is used.

In the air gap, the Nusselt number Nu can be calculated from modified Taylor number Ta_m [187, 188]:

$$Nu = \begin{cases} 1, & Ta_m < 1,700 \\ 0.064 \cdot Ta_m^{0.367}, & 1,700 \leq Ta_m < 10,000 \\ 0.204 \cdot Ta_m^{0.241}, & 10,000 \leq Ta_m < 10,000,000 \end{cases} \quad (4.25)$$

where Ta_m can be calculated as [187, 188]:

$$Ta_m = \frac{\omega_m \cdot r_m \cdot \delta^3}{\nu^2 \cdot F_g} \quad (4.26)$$

in which ω_m is mechanical angular velocity, r_m is the medium radius of air gap, δ is radial air gap length, ν is the kinematic viscosity of air, and F_g is a geometrical factor which is about 1 in practice.

Both washing and spinning modes have been calculated. The temperature of different components at steady state (after an operating time of 5 h) is given in Table 4.10.

Table 4.10   Maximum temperature of different components at steady state for an ambient temperature of 40 ℃

Component	Maximum temperature/℃	
	Washing mode	Spinning mode
Stator winding	85.1	95.1
Stator stack	81.4	92.9
Rotor	80.5	94.0
Case	76.9	89.8

Considering that S3 operating mode is actually used in spinning mode, the results in Table 4.10 indicate a relatively low utilization of motor. However, the stator current should nevertheless be limited to ensure resilience to demagnetization. When ferrite magnets with better performance than Y30BH such as NMF series [189] are selected, the motor performance can be further improved, but its cost will increase simultaneously.

4.6.4   Manufacturing of the Prototype Motor

Based on the analyses in this chapter, a prototype of the spoke-type synchronous motor was manufactured. Pictures are given in Fig. 4.26.

(a)   (b)

(c)   (d)

(e)   (f)
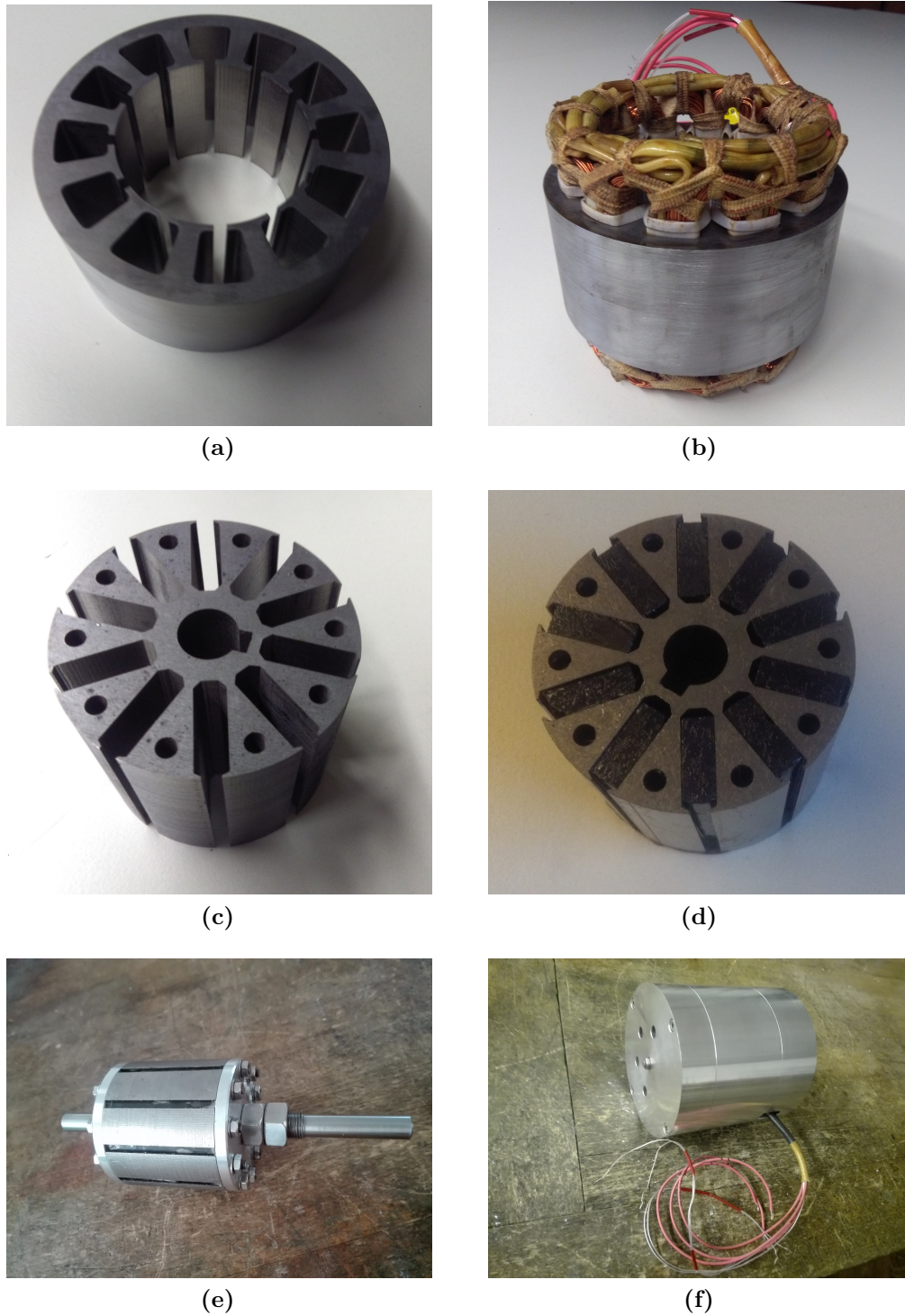
Fig. 4.26 Pictures of the prototype motor. (a) Stator stack. (b) Stator stack with winding. (c) Rotor stack. (d) Rotor stack with permanent magnets. (e) Rotor assembled. (f) Motor assembled.

5

Design Aspects of Permanent-Magnet Assisted Synchronous Reluctance Motors

In this chapter, the layout of a permanent-magnet assisted synchronous reluctance motor (PMASynRM) prototype was worked out based on the automatic optimization process described in Chapter 3. The performance of the motor was investigated by using 2D and 3D FEM, taking into account mechanical strength at high speed, efficiency, torque, and resilience against demagnetization. A prototype was manufactured according to these results.

5.1 Motor Configuration

Two typical rotor layouts of a permanent-magnet assisted synchronous reluctance motor (PMASynRM) are illustrated in Fig. 5.1. A layout with magnet blocks is commonly selected [127–130], because it is easier to manufacture. However, the shape of flux barriers is restricted by the shape of magnets considering that machining of ferrite magnets is difficult. A layout with injection molded plasto-ferrite was proposed in [32], where the shape of flux barriers can be designed flexibly, and the rotor can be continuously skewed. In this thesis, the latter is not chosen for two reasons:

- A prototype with this layout is difficult to manufacture, because special equipment and technology are required for the molding process.

- Injection molded plasto-ferrite has a lower remanence than sintered ferrite, which means a lower torque density.

5. Design Aspects of Permanent-Magnet Assisted Synchronous Reluctance Motors
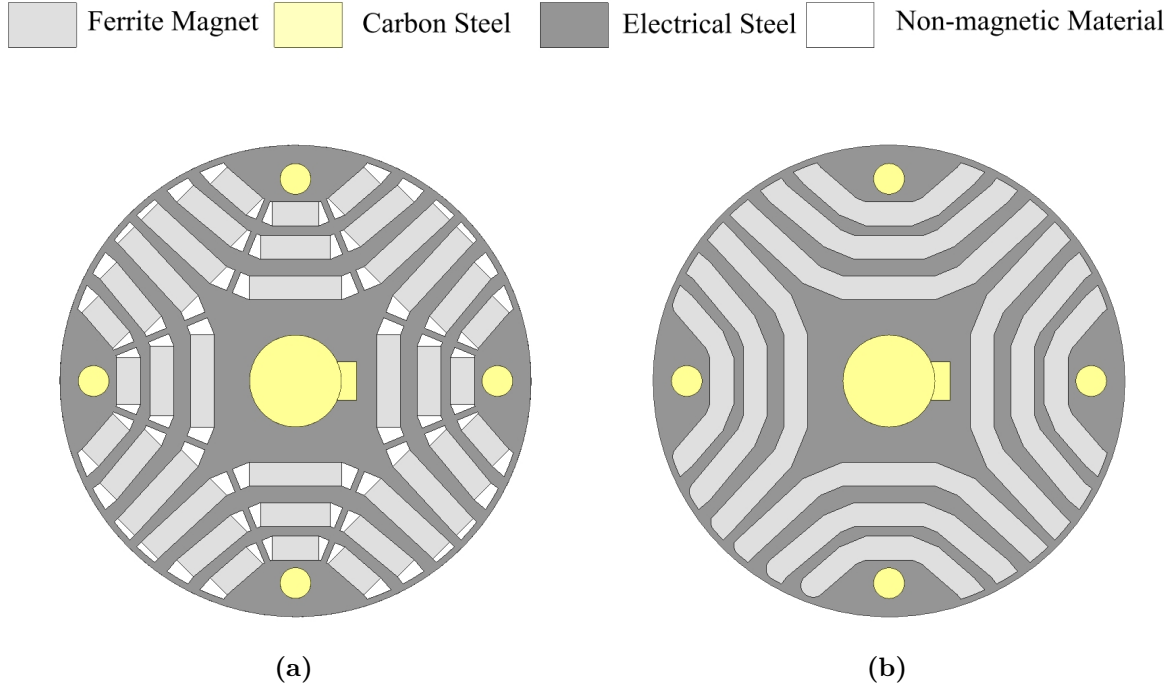
Fig. 5.1 Typical rotor layouts of PMASynRM. (a) With magnet blocks. (b) With injection molded plasto-magnet.

The initial width of all bridges in the rotor stack is set to 0.8 mm. A mechanical analysis will be carried out for the designed motor later. If the mechanical strength turns out to be not sufficient, this value must be increased.

In order to compensate for the flux leakage in the bridges, three magnets are used in each layer to make the flux barriers completely filled by magnets. If the ratio of width and height of each flux barrier were kept constant, flux density would be distributed evenly in different layers meaning no weak point for demagnetization of the magnets [190]. Ferrite magnets with different heights would then be required to satisfy this condition. In this thesis, this configuration is not used, so that the dimensions of magnets can be adjusted to standard sizes. All magnets have the same height of 3 mm in magnetizing direction. Widths have been adjusted to standard values of 6 mm, 9 mm, and 12 mm.

Because the space is limited, it is difficult to achieve a number of poles above four. As a consequence, an integer-slot winding results from a 12-slot/4-pole configuration. A single-layer winding instead of a double-layer short-pitch winding has been finally selected to limit the motor size, because the latter has a lower winding factor and leads to a lower power density. Details of the designed motor are listed in Table 5.1.

Table 5.1 Configuration of the PMASynRM

| Motor type	PMASynRM
Rotor layout	layout with magnet blocks
Stator winding	single-layer winding
Number of phases	3
Number of slots	12
Number of poles	4
Outer diameter of stator stack	116 mm
Outer diameter of rotor stack	61.6 mm
Length of stator stack	50 mm
Length of rotor stack	50 mm
Length of air gap	1 mm
Material of magnets	Y30BH
Height of magnets	3 mm
Widths of magnets	6 mm, 9 mm, 12 mm
Conductor diameter	0.56 mm
Number of conductors in parallel	2
Number of turns per coil	180
Diameter of shaft	12 mm
Width of bridges	0.8 mm

5.2 Mechanical Analysis

The process of mechanical analysis for a permanent-magnet assisted synchronous reluctance motor (PMASynRM) is similar to that for a spoke-type synchronous motor as presented in Chapter 4. The analysis was carried out again for 20,000 min^{-1}. Maximum von Mises stress values in each component are listed in Table 5.2. The distribution of von Mises stress at 20,000 min^{-1} is given in Fig. 5.2. From the results, it can be concluded that the design of PMASynRM has a sufficient mechanical strength as the safety factor is higher than 2 in whole speed range.

Table 5.2 Results of mechanical analysis of the PMASynRM by using 3D FEM

Component	Material	Von Mises stress/MPa	Yield strength/MPa	Safety factor
Shaft	S235JR	1.7	235	138.2
Bolts	S235JR	111.7	235	2.10
Stack	M270-35A	172.8	355-450	2.05
End ring	AA7075	106.0	360-470	3.40
PM	Y30BH	13.7	34 (tensile strength)	2.48
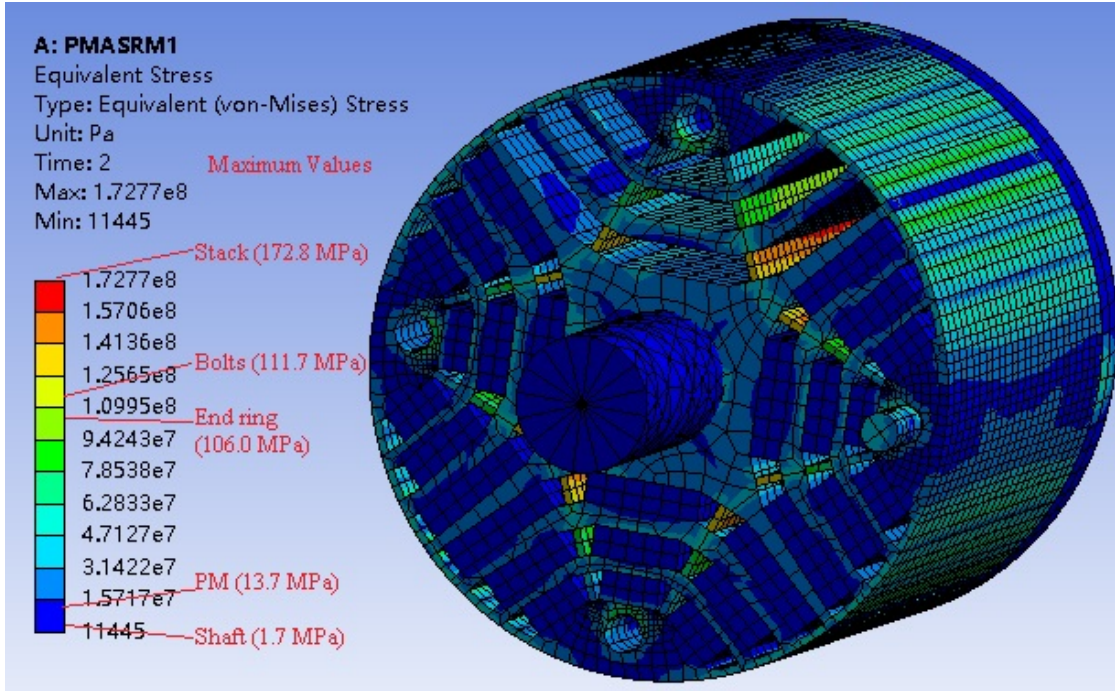
Fig. 5.2 Distribution of von Mises equivalent stress calculated at 20,000 min^{-1}.

5.3 Calculation of Operating Points

In this section, a 2D FE model for the permanent-magnet assisted synchronous reluctance motor (PMASynRM) has been built in Ansys Electronics Desktop.

First, a no load analysis has been carried out. Fig. 5.3 illustrates the corresponding flux density distribution. The phase EMF waveform at no load presented in Fig. 5.4 shows a significant 3rd harmonic, which forces a star connection. The line-to-line EMF waveform at no load is presented in Fig. 5.5.

For both load operating points given in Table 3.1, the motor performance was checked. Details are listed in Table 5.3. Torque waveforms are shown in Fig. 5.6. The results indicate that torque ripple in the PMASynRM is higher than in the spoke-type synchronous motor, especially in washing mode. This can be explained by a lower fundamental pulsation frequency of the torque ripple in this motor.

Table 5.3 Details of operating points

Configuration	PMASynRM	
Operating mode	washing	spinning
Average torque/(N·m)	1.3	0.3
Torque ripple coefficient	8.9%	16.0%
Rotation speed/min^{-1}	550	16600
Current, RMS value/A	1.77	1.41
Efficiency	66.9%	92.1%
Power factor	0.807	0.983
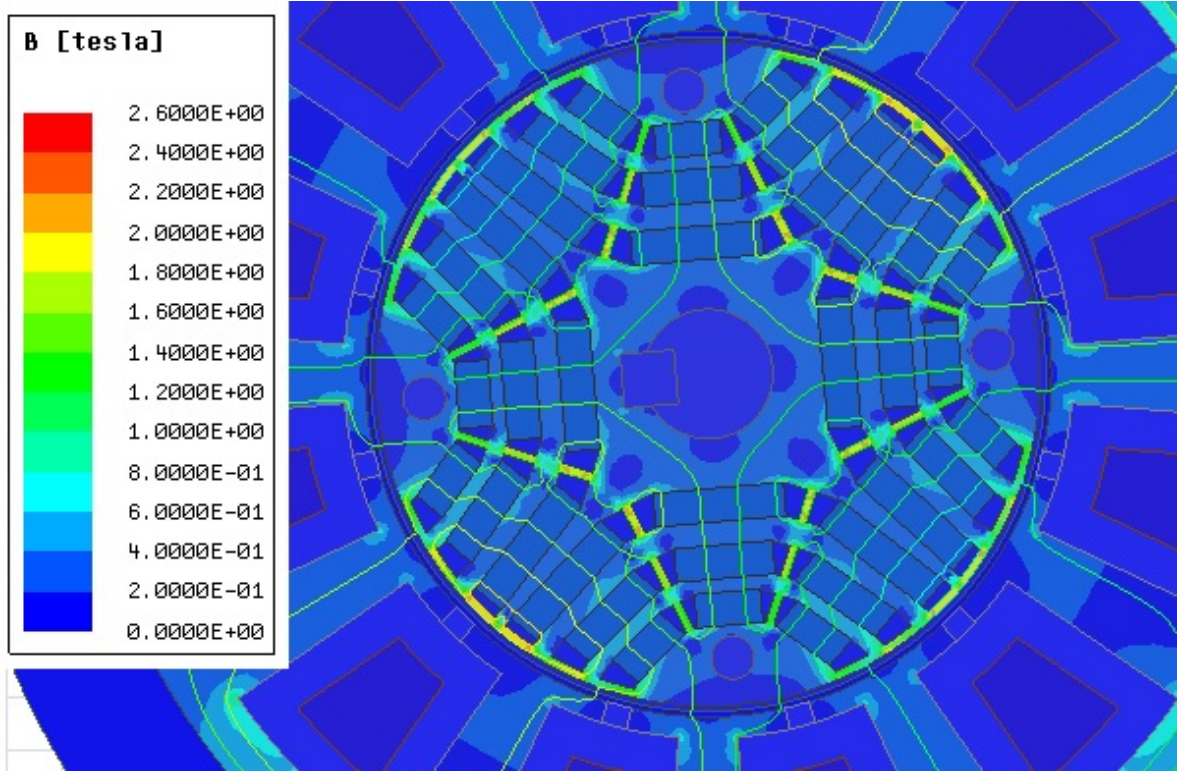
Fig. 5.3 Flux distribution of the PMASynRM at no load.
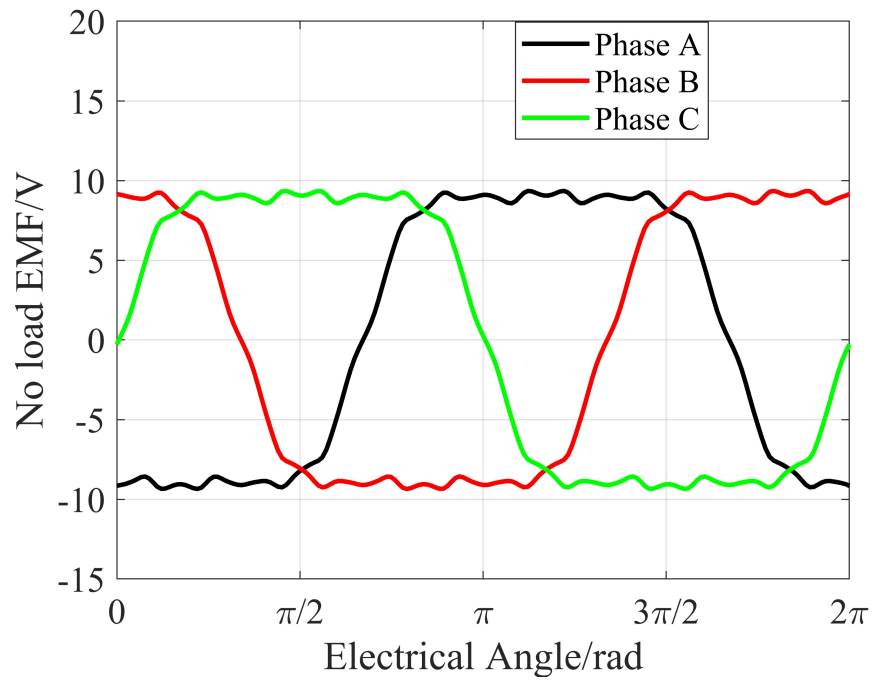
Fig. 5.4 Phase EMF waveform of the PMASynRM at no load.

Fig. 5.5 Line-to-line EMF waveform of the PMASynRM at no load.

Fig. 5.6 Torque waveforms at both operating points.

5.4 Demagnetization Analysis

The analysis of irreversible demagnetization is similar to the one presented in Section 4.3. A comparison of demagnetization ratio of both motors is presented in Fig. 5.7, from which it can be concluded that the permanent-magnet assisted synchronous reluctance motor (PMASynRM) has a high resilience against demagnet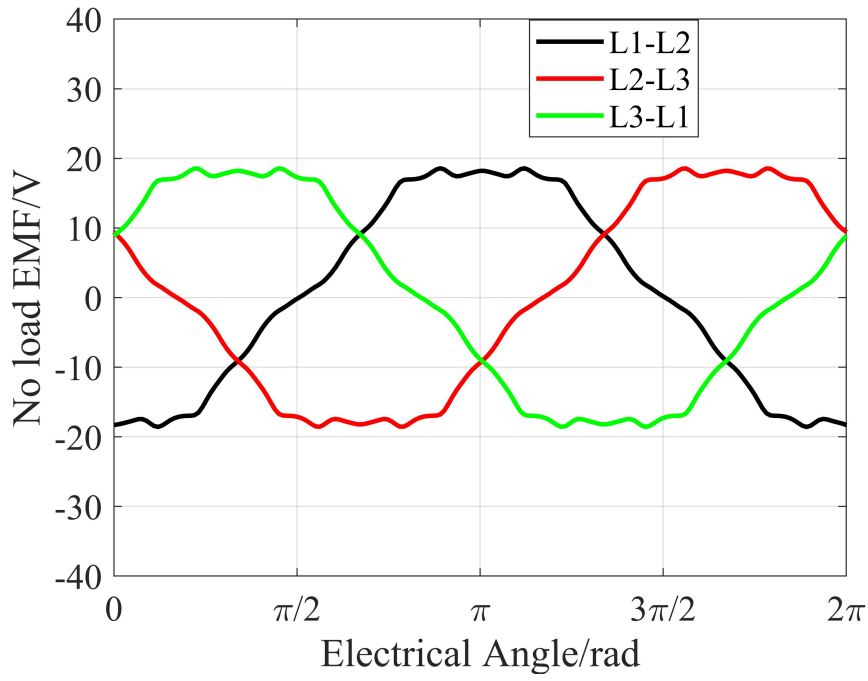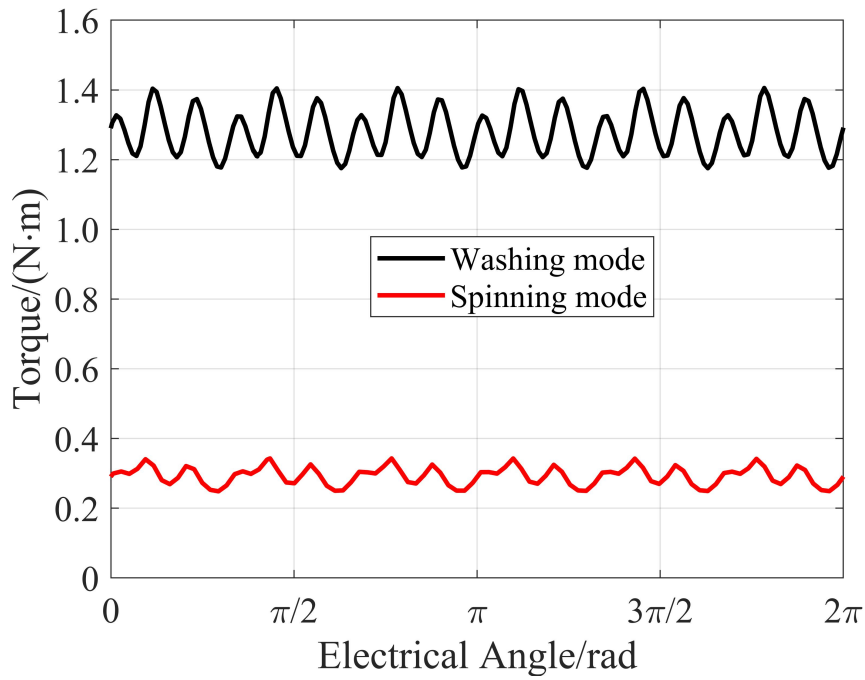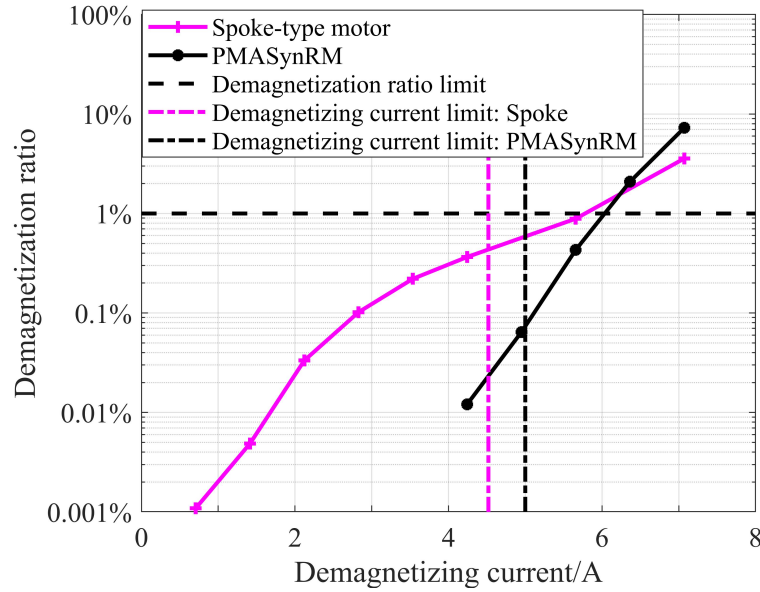ization. The explanation is that the magnets in this motor are surrounded by electrical steel, and they are not in direct contact with highly saturated bridges.

Fig. 5.7 Comparison of the demagnetization ratios of both motors.

5.5 Thermal Analysis

For a thermal analysis, the end turns are simplified to two copper rings considering their overlap. Other settings are the same as those presented in Section 4.6.3. Fig. 5.8 shows details of copper bars and end turns.

The analysis has been carried out during an operating time of 5 h. The detailed temperatures of various components are listed in Table 5.4. By comparing Tables 4.10 and 5.4, it can be observed that the temperatures in stator windings for both motors do not differ much. The reason is, that the PMASynRM has a larger size but simultaneously higher copper losses due to more turns of coils and longer end turns.

Table 5.4 Maximum temperatures of different components at steady state for an ambient temperature of 40 ℃

Component	Maximum temperature/°C	
	Washing mode	Spinning mode
Stator winding	85.5	91.4
Stator stack	83.9	90.5
Rotor	82.3	90.8
Case	79.8	87.2
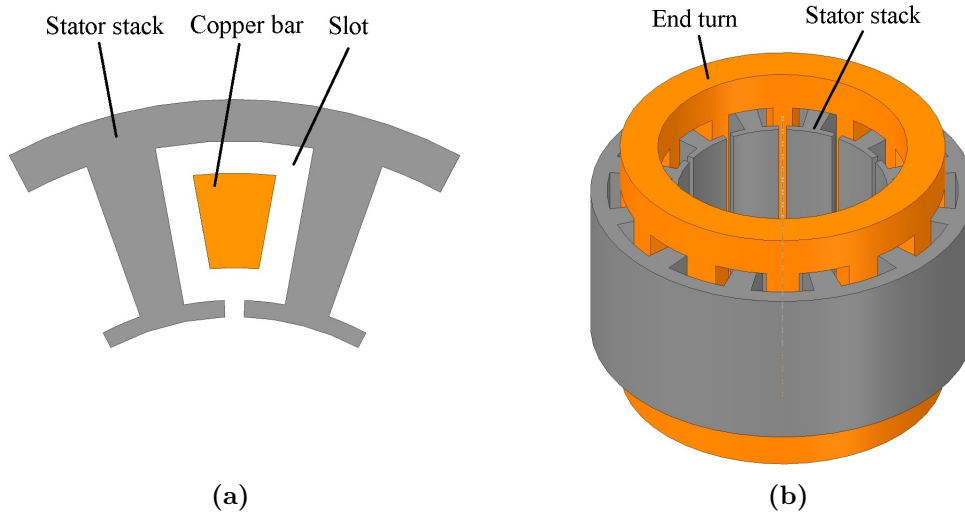
Fig. 5.8 Copper bars and rings representing stator winding in a slot and end turns. (a) Stator winding in a slot. (b) End turn.

5.6 Manufacturing of the Prototype Motor

According to the studies in this chapter, it can be concluded that the provided design satisfies the requirements in aspects of mechanical reliability, resilience against demagnetization, and thermal behaviour. Fig. 5.9 presents some pictures of the manufactured prototype.
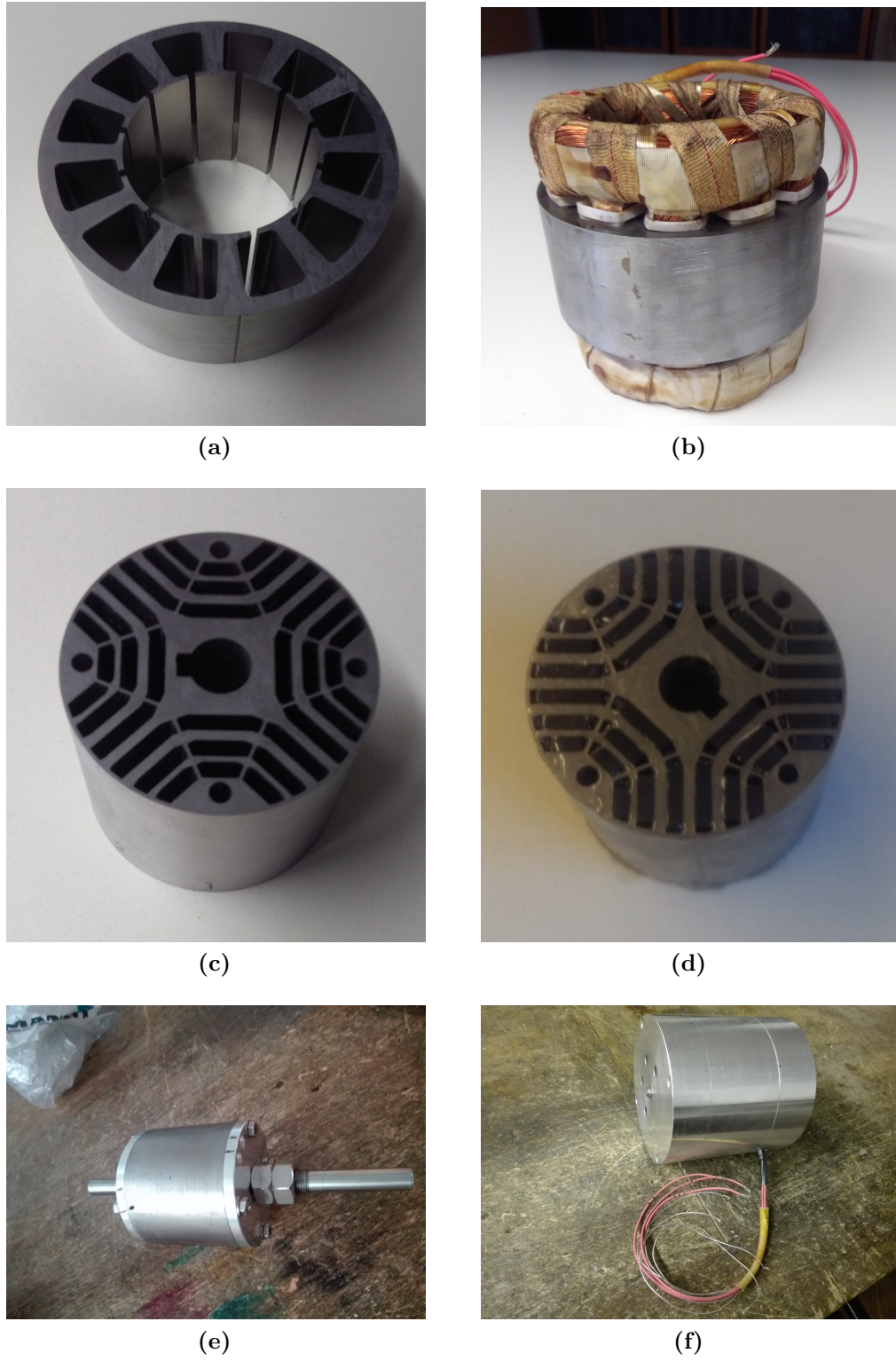
Fig. 5.9 Pictures of the prototype of PMASynRM. (a) Stator stack. (b) Stator stack with winding. (c) Rotor stack. (d) Rotor stack with permanent magnets. (e) Rotor assembled. (f) Motor assembled.

Experiments

In this chapter, the experimental results of both motors are presented. The tests were not completely finished. The test bench broke at about 10,000 min^{-1} due to unexpected vibrations. Section 6.1 describes the test bench. An angle measurement board has been designed to measure the rotor angle. Mechanical components have also been designed to fix the motors and the angle measurement board to the test bench. In Sections 6.2 and 6.3, the results of no load, short-circuit, and load tests are reported and compared with the results from FEM. Section 6.4 describes additional no load tests to make sure that there is no significant irreversible demagnetization. Section 6.5 presents the results of thermal tests. Finally, a summary is given in Section 6.6.

6.1   Introduction of the Test Bench

Fig. 6.1 illustrates the layout of the test bench. A separately excited DC motor is used as the prime mover, which has a maximum speed of 3,050 min^{-1} and a maximum power of 19.5 kW. A belt transmission is used in the system to increase the maximum speed of the load side.

PT100 sensors have been embedded in the motor winding to monitor the temperature. A rotating torque sensor is used to measure the torque. An angle sensor with giant magnetoresistance (GMR) elements is used to measure the mechanical angle. In order to provide the magnetic field for GMR sensor, a diametrically magnetized disc-shaped permanent magnet has been fixed to one end of the shaft of each motor.

6.1.1   Motor and Generator Modes

For the following tests, the test machine is driven by a prime mover and works in generator mode. As shown in Fig. 6.2, Y-connected adjustable resistors were selected as load of the test motor. A description of the relationship between motor mode and
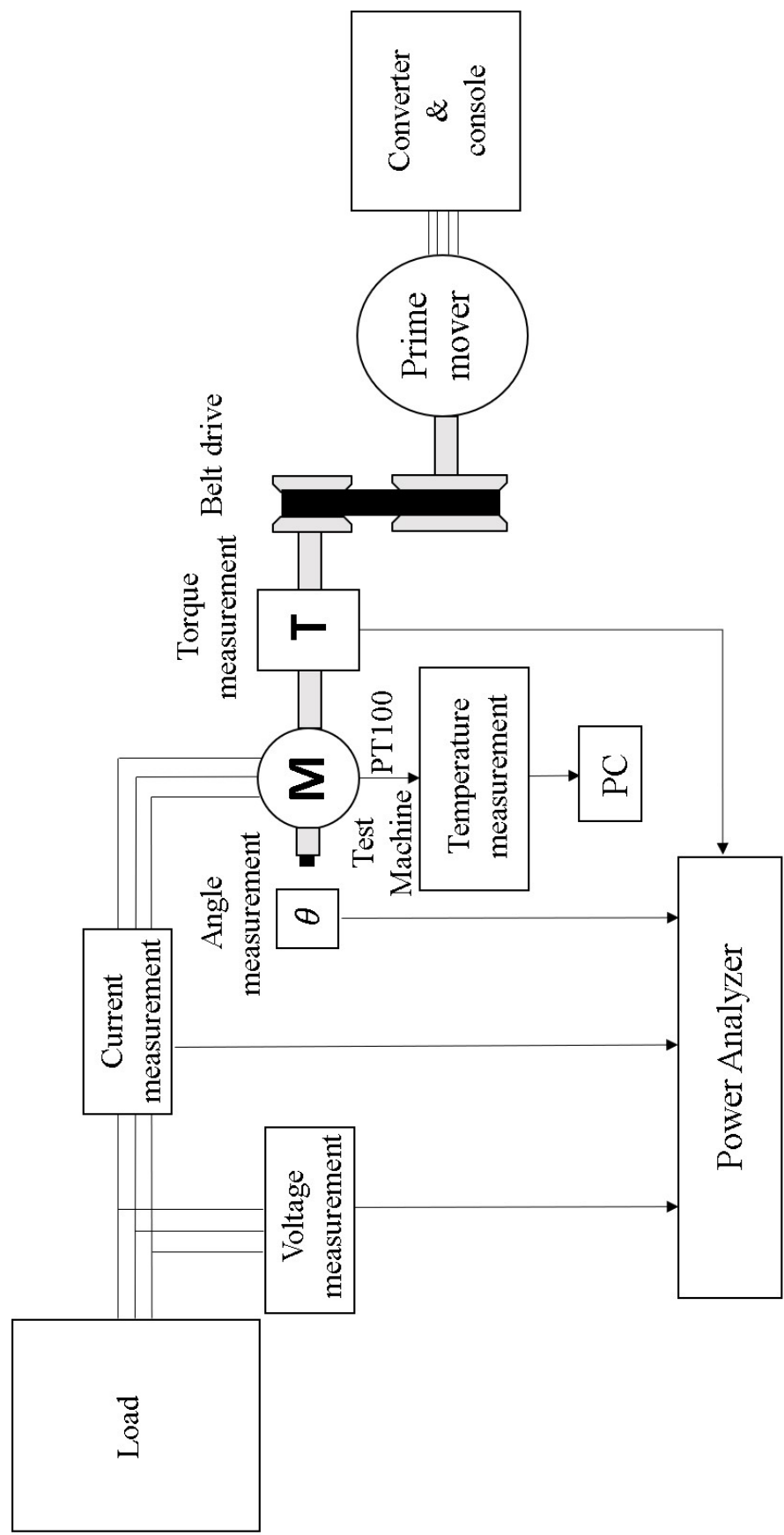
Fig. 6.1 Scheme of the test bench.

generator mode is given in Fig. 6.3. In motor mode, a positive I_q is applied, while it is negative in generator mode.
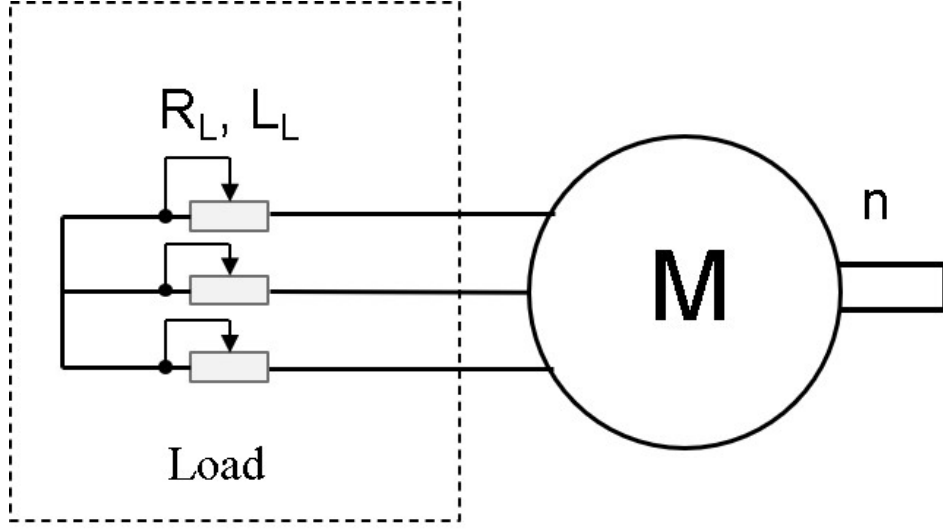
Fig. 6.2 Load of the test motor.
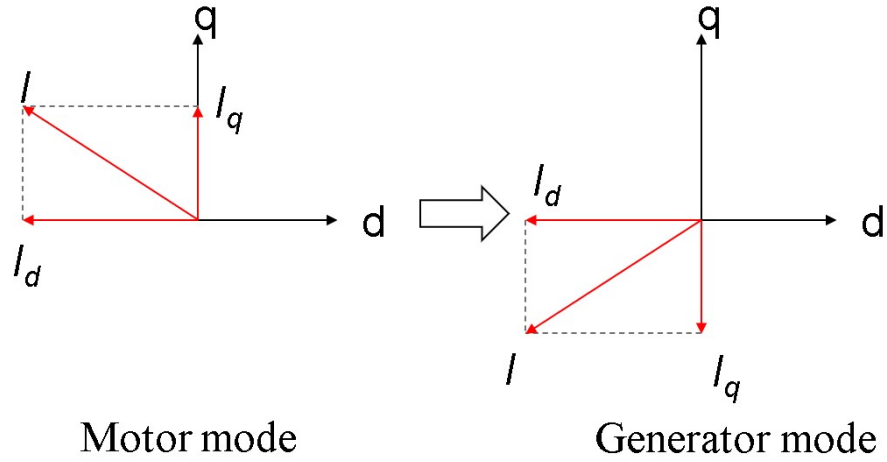
Fig. 6.3 The relationship between motor and generator modes.

6.1.2   Design of the Angle Measurement Board

The scheme of the angle measurement board is illustrated in Fig. 6.4. The printed circuit board (PCB) consists of three parts: angle sensor module, analog-to-digital converter (ADC) module, and reference voltage module.

An integrated circuit with GMR elements evaluates the field of the shaft mounted magnets and outputs the angle as analog signal [191]. Fig. 6.5 presents a photo of the board. In this thesis, the analog outputs are recorded by using a power analyzer for further data processing.
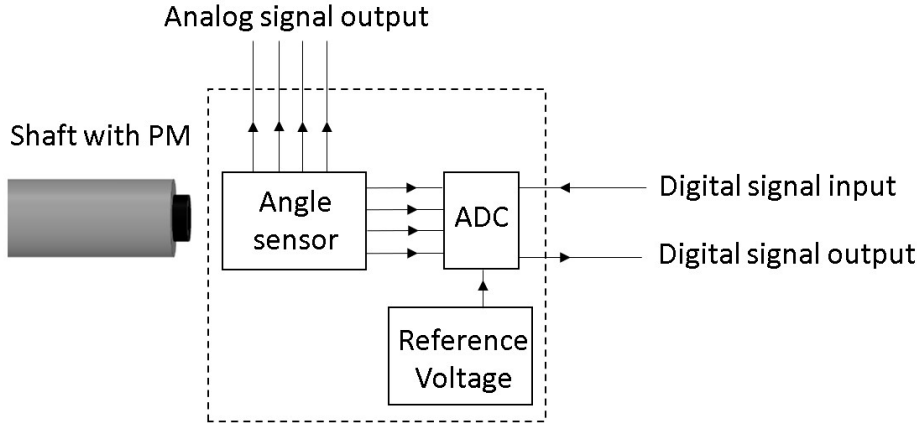
Fig. 6.4   Scheme of the angle measurement board.
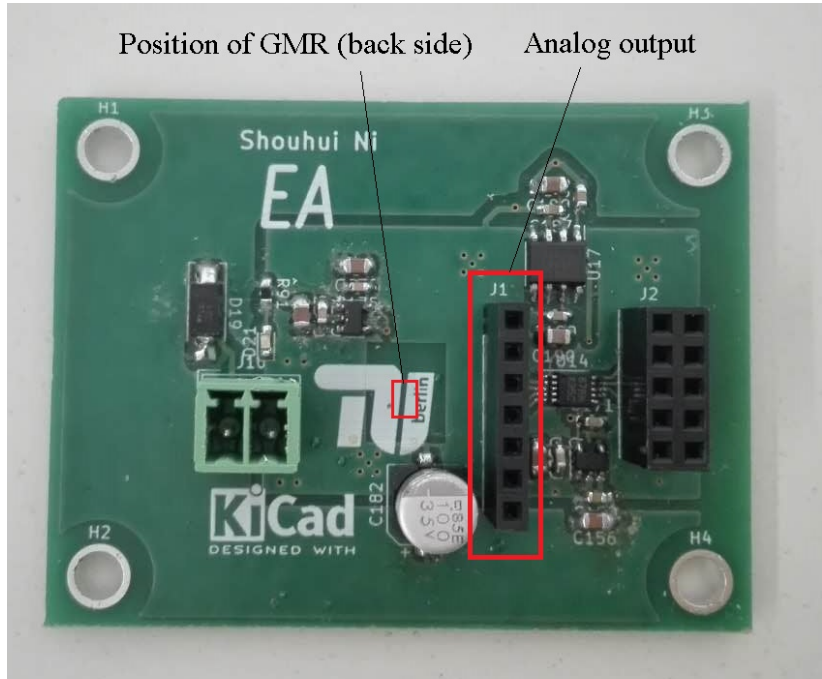
Fig. 6.5   Angle measurement board.

6.1.3   Mechanical Components

Fig. 6.6 shows the supports for the test motor and for the angle sensor board. The center area of the latter has been removed in order to avoid interference between support and electronic components on the PCB.

Since the GMR sensor only detects flux field components in the plane of the sensor (plane x-y), the relevant flux density B_{xy} results as:

$$B_{xy} = \sqrt{B_x^2 + B_y^2} \tag{6.1}$$
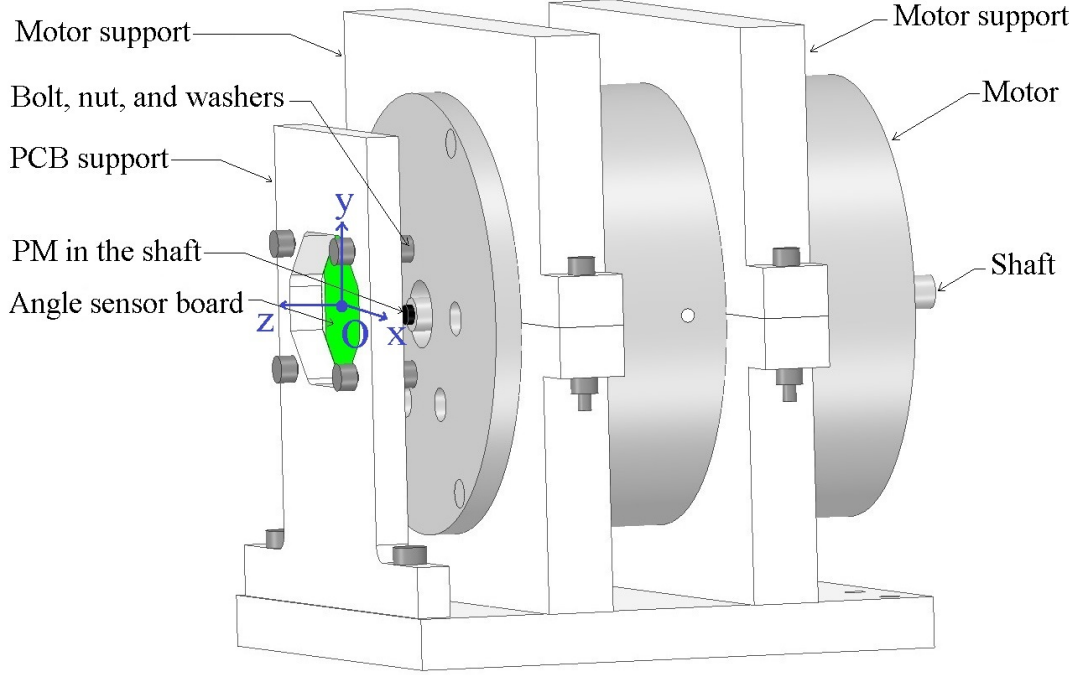
Fig. 6.6   Mechanical components to fix the motor and angle sensor board.

where B_x and B_y represent x and y components of flux density, respectively. As flux density B_{xy} for the GMR elements must be between 24 mT and 50 mT [191], the required distance between the angle sensor and the magnet should be calculated by 3D FEA.

A 3D model for FEA is illustrated in Fig. 6.7. The distance between angle sensor and magnet is labeled d_p. For each value of d_p, the maximum value of B_{xy} is calculated and labeled $B_{xy,max}$. Fig. 6.8 presents the results, and the allowed range for d_p lies between the two dotted lines.
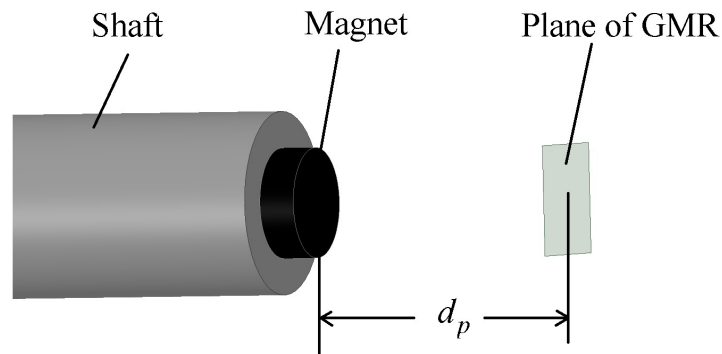
Fig. 6.7   The 3D FE model for the calculation of the distance.

The distance between the GMR sensor and magnet should therefore be set between 2 mm and 3 mm. In practice, the distance is adjusted by changing the number of washers.
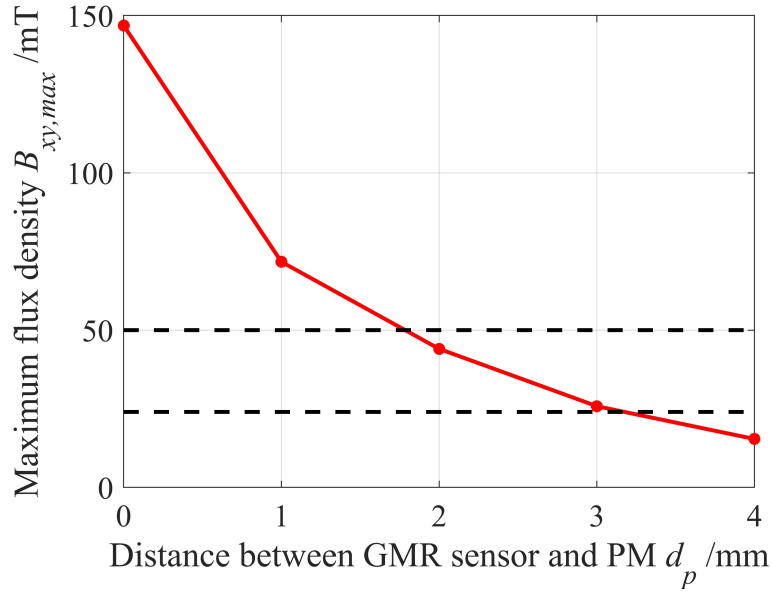
Fig. 6.8   The relationship between $B_{xy,max}$ and d_p.

6.2   No load Tests

The test bench for no load tests is shown in Fig. 6.9. For both motors, no load tests have been carried out at different speeds.
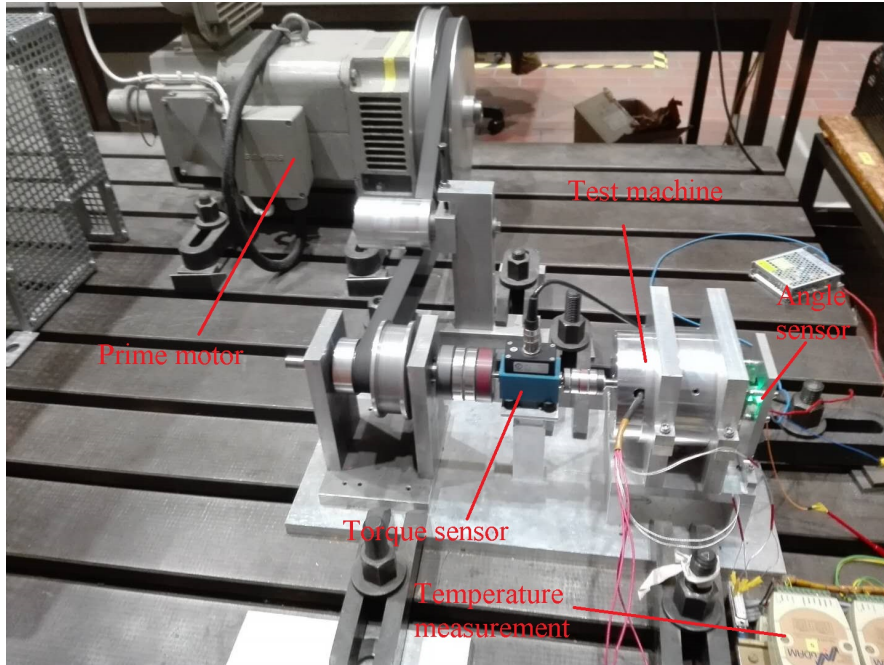
Fig. 6.9   Test bench for no load tests.

The angle measurement module has also been tested. The mechanical angle between rotor and the magnet on the shaft was unknown when assembling the latter to the shaft. To solve the problem, the relationship between the phase angle of no load EMF and the corresponding angle signal must be determined for further studies.

6.2.1 No load Test of the Spoke-type Motor

For the spoke-type motor, some damages occurred during manufacturing resulting in a reduction of rotor length. Considering the effects by the damages, a new FEA adapted to resulting modifications was carried out. As shown in Fig. 6.10, the no load EMF is reduced by about 10% compared to the original design. The waveform from experiment fits well with the one from modified FEA, which validates the correctness of the magnetic field calculation. The relationship between no load EMF and speed is presented in Fig. 6.11. The results of test and modified FEA fit well with a maximum difference of 2.0%.
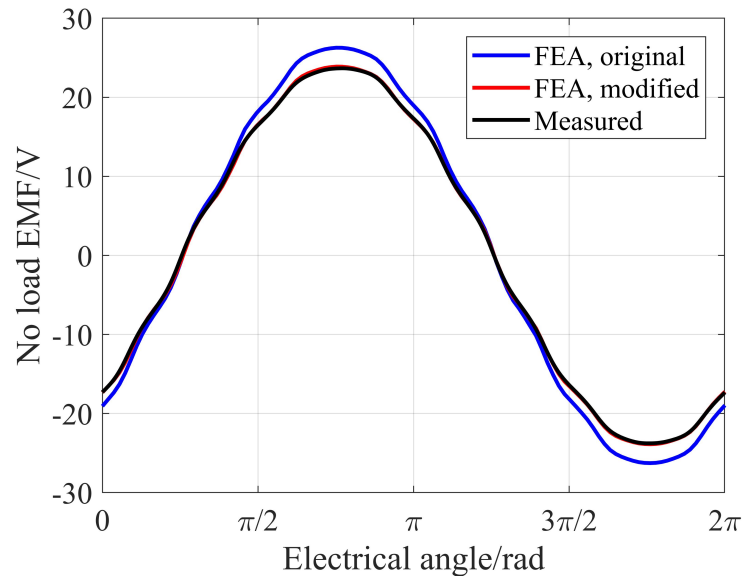
Fig. 6.10 The waveforms of no load line-to-line EMF of the spoke-type motor in one electrical cycle at $550\,\text{min}^{-1}$.
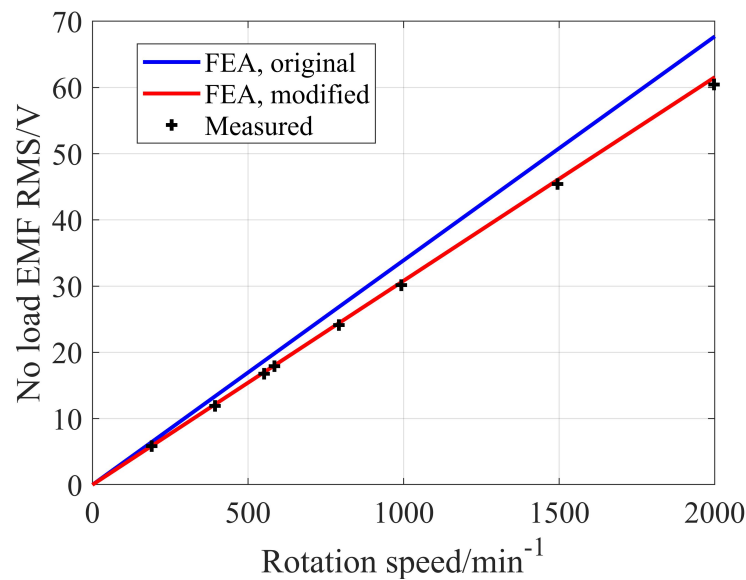
Fig. 6.11 RMS value of no load line-to-line EMF of the spoke-type motor at different speeds.

97

6.2.2 No load Test of the Permanent-magnet Assisted Synchronous Reluctance Motor

For the permanent-magnet assisted synchronous reluctance motor (PMASynRM), the waveforms of no load EMF and the relationship between no load EMF and speed are presented in Figs. 6.12 and 6.13, respectively.
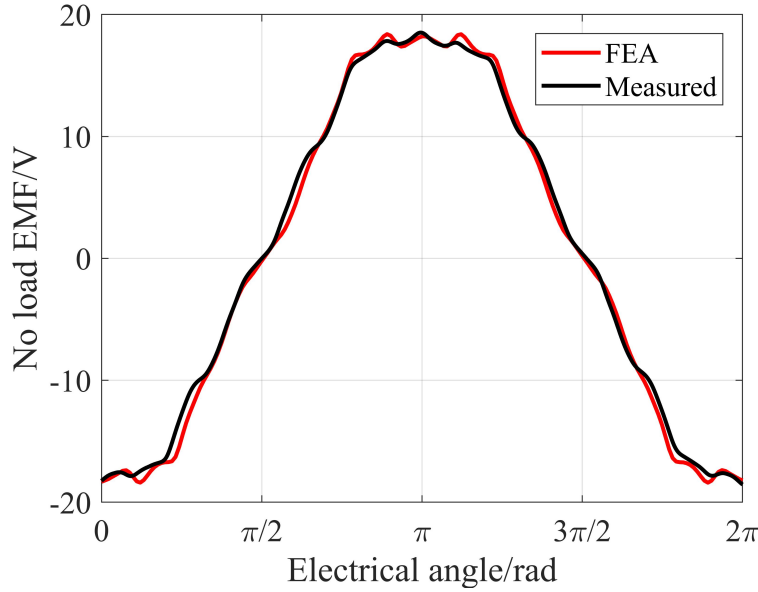
Fig. 6.12 The waveforms of no load line-to-line EMF of the PMASynRM in one electrical cycle at $550\,\text{min}^{-1}$.
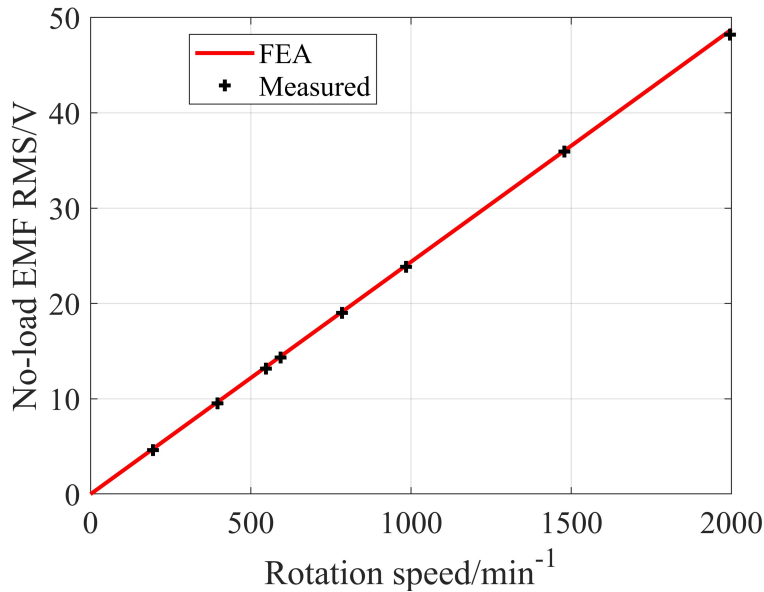
Fig. 6.13 RMS value of no load line-to-line EMF of the PMASynRM at different speeds.

In Fig. 6.12, both waveforms fit well in general but still have a slight difference. The explanation is, that the characteristics of the edges of steel sheets have changed during

manufacturing, which further changes the distribution of flux density in the air gap, especially near the highly saturated bridges. As shown in Fig. 6.13, the RMS values of both EMF waveforms at different speeds fit well with a maximum difference of 2.6%. The test validates the correctness of the magnetic field calculation for the PMASynRM.

6.2.3 Output of the Angle Sensor

In this thesis, the analog output of the angle measurement board is used. The waveforms in one mechanical cycle are presented in Fig. 6.14.
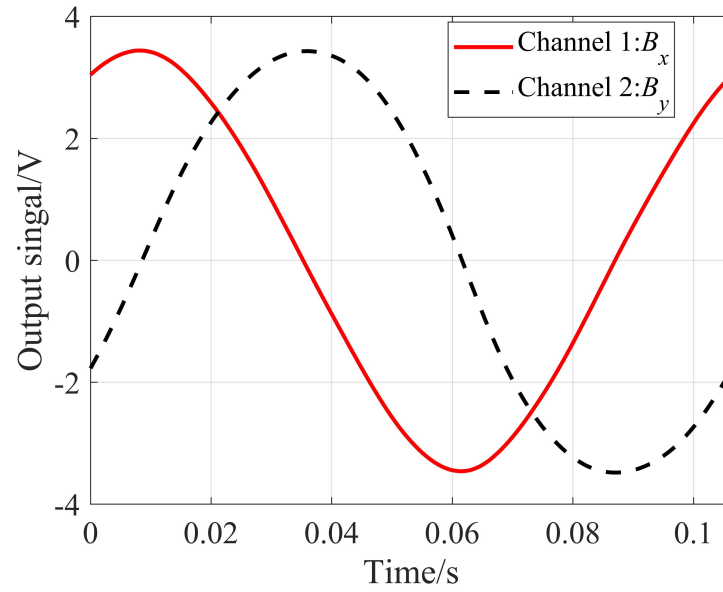
Fig. 6.14 Analog output of the angle measurement board.

After adjustment according to the calibration guideline in [191], the resulting angle is given in Fig. 6.15. The angle was solved by the four-quadrant inverse tangent of the quotient of B_y and B_x (function 'atan2' in MATLAB).

When the speed of the test machine is stable, the resulting angle should be linear in theory. In Fig. 6.15, it shows significant nonlinearity. Compared to a fitted linear curve, the maximum difference is about 0.083 rad, or 4.8°, which is much higher than 2.2° according to the overall angle error provided in [191]. Possible reasons are:

- The output signals of the angle sensor in Fig. 6.14 are not ideal sinusoidal waveforms.

- The speed of prime mover was not stable due to the precision of its control system. At low speed, this effect was more obvious. As shown in Fig. 6.16, the no load EMF was not stable.
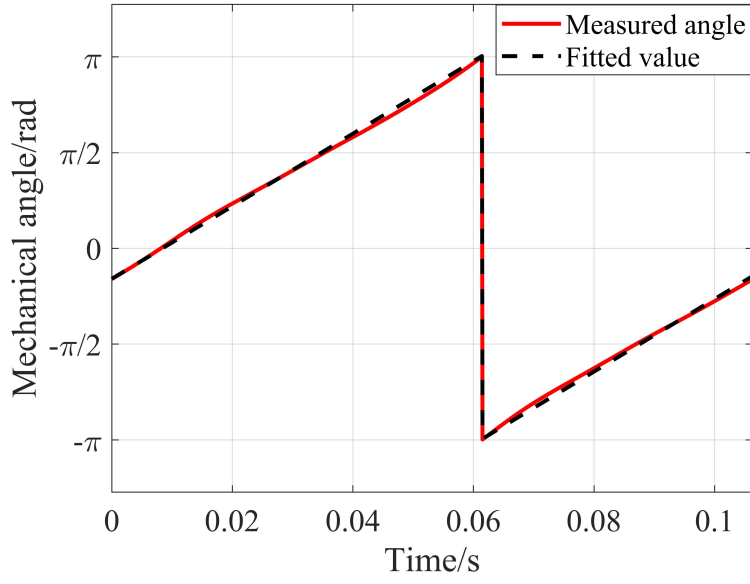
Fig. 6.15   Measured angle and fitted value.
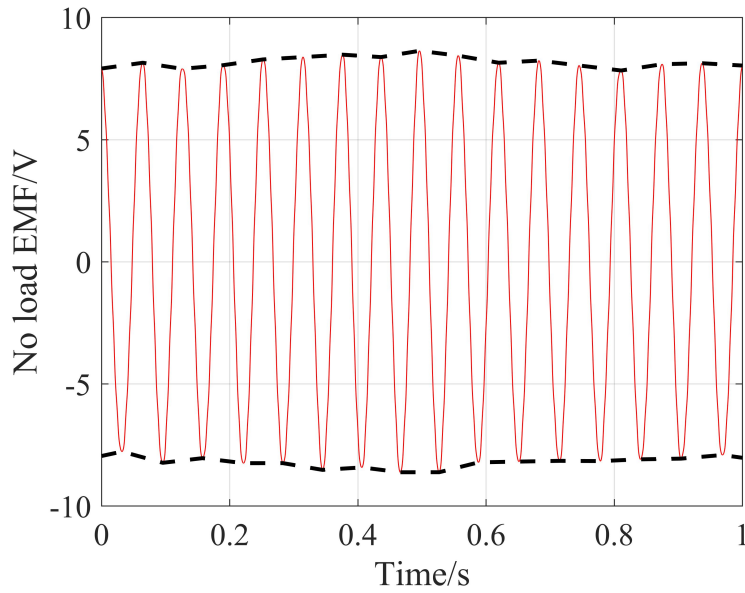
Fig. 6.16   The no load EMF of the spoke-type motor at $200\,\mathrm{min}^{-1}$ and its amplitude envelope.

In order to avoid the nonlinearity error and reduce the computation cost of data processing, the zero point of the angle signal corresponding to B_x is used as the reference point in practice. The electrical angle between the zero point of line-to-line no load EMF and the reference point was then measured for further studies. The results are presented in Fig. 6.17.
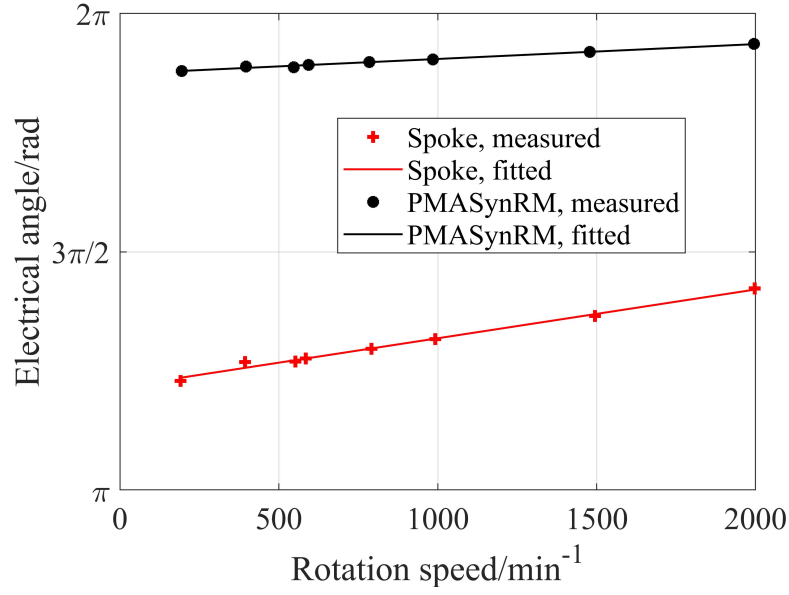
Fig. 6.17 The measured angle between line-to-line no load EMF and B_x vs. speed

The measured angle grows linearly with rotation speed for both motors. This can be explained by measurement and signal transmission delays and an additional magnetic field produced by the rotating magnet on the shaft and metal parts, i.e. the ground layer of the PCB and the motor case.

In further studies of this thesis, this effect is considered. For a better angle measurement by using the GMR sensor, the design of the PCB as well as the mechanical components must be improved.

6.3   Short-circuit and Load Tests

Both short-circuit and load tests have been carried out in generator mode. In short-circuit tests, the lead wires of three-phase winding were connected directly. In load tests, Y-connected adjustable resistors were used. For each motor, different resistor values have been used. The results are presented in Appendix A. The definition of current phase angle and its measurement will be presented later in this section.

6.3.1   Measurement of Current Phase Angle

In the tests, the definition of positive direction was kept consistent with the one presented in Section 3.2.2. Fig. 6.18 illustrates the relationships among different angles. $\underline{E}_{AO}$ represents the phasor of no load EMF of phase A. $\underline{E}_{AB}$, $\underline{I}_A$, and $\underline{U}_{sh}$ represent the phasors of line-to-line no load EMF of A-B, current of phase A, and output voltage of the angle sensor. θ_E, θ_I, and θ_s are the corresponding phase angles. θ_{Es} is the angle between $\underline{E}_{AB}$ and $\underline{U}_{sh}$. θ_{Is} is the angle between $\underline{I}_A$ and $\underline{U}_{sh}$.
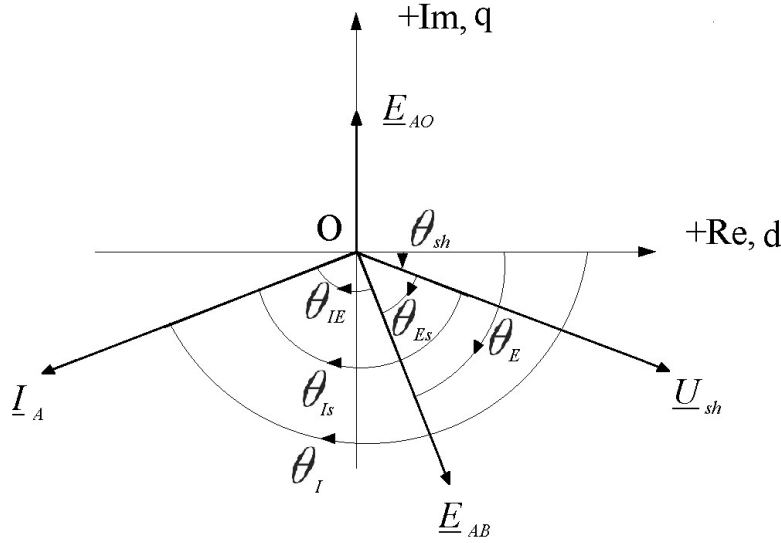
Fig. 6.18 Phasors and angles.

The phase angle of the stator current can be calculated as:

$$\begin{aligned}
\theta_I &= \theta_{IE} + \theta_E \\
&= \theta_{Is} - \theta_{Es} + \theta_E \\
&= \theta_{Is} - \theta_{Es} - \frac{\pi}{3}
\end{aligned} \tag{6.2}$$

where θ_{IE} is the angle between $\underline{I}_A$ and $\underline{E}_{AB}$.

θ_{Es} has been determined in no load test according to Fig. 6.17. θ_{Is} can be measured in short-circuit and load tests.

6.3.2   Calculation of Inductances

The voltages satisfy the following equations:

$$\begin{cases}
V_d = -I_d \cdot R_L + \omega \cdot I_q \cdot L_L \\
V_q = -I_q \cdot R_L - \omega \cdot I_d \cdot L_L
\end{cases} \tag{6.3}$$

where R_L and L_L are resistance and inductance of one phase of the adjustable resistors.

Stator currents can be expressed as:

$$\begin{cases}
I_d = I_s \cdot \cos \theta_I \\
I_q = I_s \cdot \sin \theta_I
\end{cases} \tag{6.4}$$

in which I_s is the RMS value of the stator current.

From (3.4), (6.3) and (6.4), the inductances can be found as:

$$
\begin{cases}
L_d = \dfrac{R_s + R_L}{\omega \cdot \tan \theta_I} - L_L \\
L_q = -\dfrac{\Psi_p}{\sqrt{2} \cdot I_s \cdot \cos \theta_I} - \dfrac{(R_s + R_L) \cdot \tan \theta_I}{\omega} - L_L
\end{cases}
\tag{6.5}
$$

According to (6.5), inductances can be figured out for each test point. Details of all test points are presented in Appendix B.

The average values of all test points have been calculated after eliminating those test points with a value more than 2 times or less than half of the corresponding average value. Table 6.1 lists the inductances calculated from test results and FEA.

Table 6.1   Inductances of both motors

Parameter	Spoke-type motor		PMASynRM	
	Experiment	FEA	Experiment	FEA
L_d/H	0.019	0.015	0.065	0.052
L_q/H	0.019	0.019	0.084	0.126

The results in Appendix B show large dispersion. In several test points, the values are more than twice larger than the corresponding average value. Compared to FEA results, the average value in Table 6.1 has a maximum deviation of about 33%. In general, the results are not satisfying. Possible explanations are:

- The speed of prime mover is not stable, especially at low speed.

- The error of angle measurement system is larger than expected.

- The current phase angle was not measured directly, leading to an even larger error.

- In (6.5), $\tan \theta_I$ is part of the denominator of the expression of L_d. When θ_I is close to $-\pi$, a small error can result in a large error in L_d.

- In (6.5), the effect of magnetic saturation was not considered.

6.4   Checking of Irreversible Demagnetization

Both motors have been designed to have high resilience to demagnetization. In this thesis, the highest achievable demagnetizing currents were provided by short-circuit tests. Thus, the no load EMFs of both motors have been checked again after these tests. From Figs. 6.19 and 6.20, it can be concluded that no significant irreversible demagnetization has taken place during the short-circuit tests, what meets expectations.
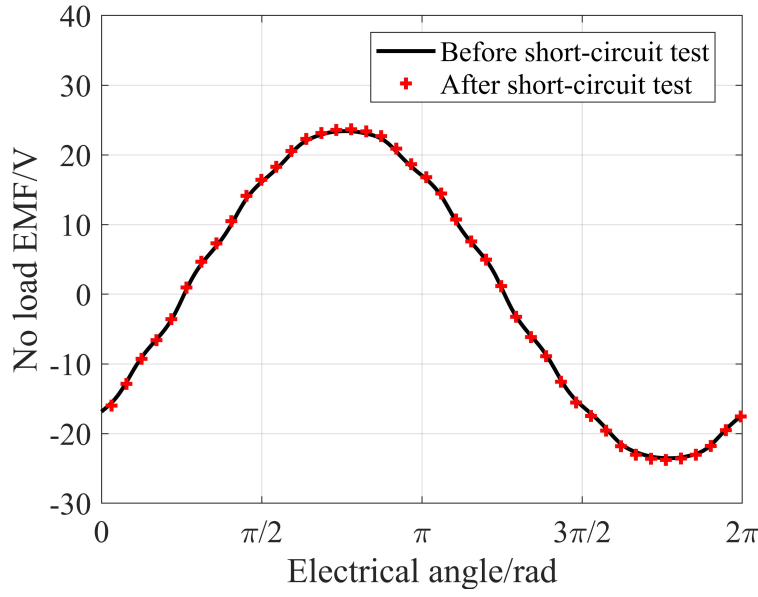
Fig. 6.19   No load EMF of the spoke-type motor before and after short-circuit test.
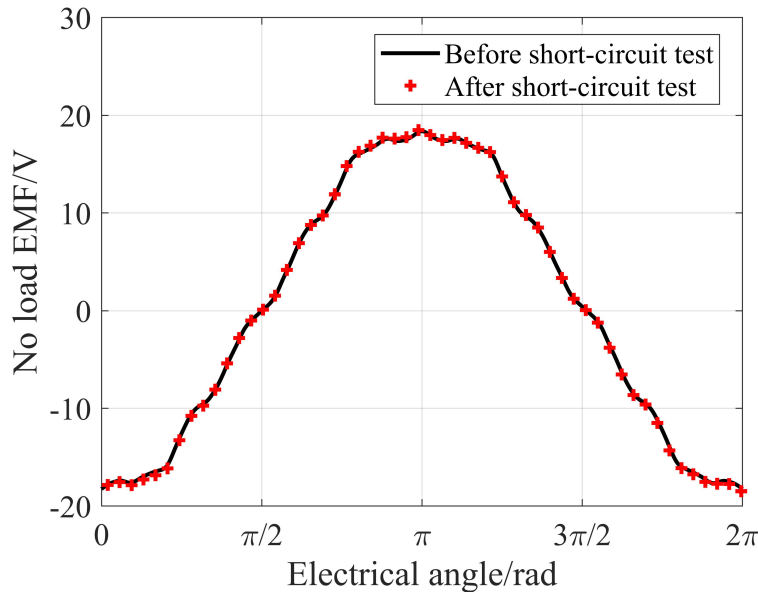
Fig. 6.20   No load EMF of the PMASynRM before and after short-circuit test.

According to Sections 4.3 and 5.4, both motors can withstand higher demagnetizing currents than those achieved in the tests. However, this has not been checked in this thesis with the absence of a matching inverter.

6.5   Thermal Tests

For the spoke-type motor, the thermal test was carried out with load resistors of $4\,\Omega$ at $550\,\mathrm{min}^{-1}$. For the PMASynRM, the values were $3\,\Omega$ and $550\,\mathrm{min}^{-1}$. The experimental results are shown in Fig. 6.21.
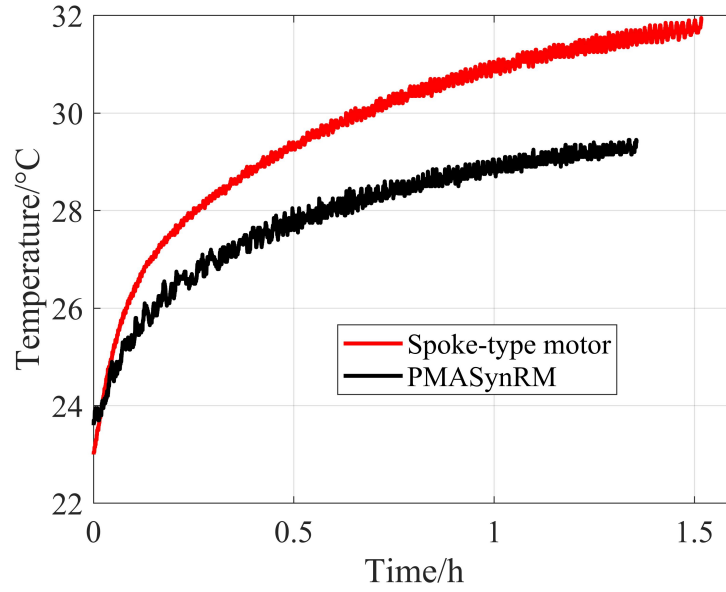
Fig. 6.21   Experimental results of thermal tests.

The temperature module had an error of $\pm 0.3\,\text{K}$ considering that the measured values were between $20\,°\text{C}$ and $40\,°\text{C}$. The recorded data had a precision of $0.1\,\text{K}$, which caused a truncation error of $\pm 0.05\,\text{K}$. By summing up both components, the total error of the measurement in Fig. 6.21 was then evaluated to be $\pm 0.35\,\text{K}$.

For both motors, the washing cycle operates in a continuous mode. The corresponding currents have been provided in Tables 4.6 and 5.3, which are different from those in thermal tests. Measures must be taken to estimate temperature rises in washing mode from experimental results.

First, the moving average method is used to eliminate noise in experimental results. The temperature rises can be regarded as proportional to the square of stator current with the following assumptions:

- Because the flux density of both motors in stator sheets were low, the iron losses were much lower than the copper losses at low speed. Therefore the iron part was neglected.

- The impact of temperature rise on the resistance of stator winding was ignored.

- Temperature rise is proportional to the value of the inner heat source when the effect of radiation is ignored.

The temperature rise ΔT_1 at the operating point 1 as defined in Table 3.1 can be estimated as:

$$\Delta T_1 = \Delta T_e \cdot \frac{I_{s,1}^2}{I_e^2} \tag{6.6}$$

where ΔT_e is the temperature rise in the thermal test, I_e is the RMS value of the corresponding stator current, and $I_{s,1}$ is the RMS value of the stator current at operating

point 1. ΔT_e is calculated as:

$$\Delta T_e = T_e - T_{e0} \tag{6.7}$$

in which T_e and T_{e0} represent the measured and the initial temperatures, respectively.

The error of ΔT_1 can be evaluated as:

$$mT_1 = 2 \cdot \sqrt{mT_e^2 \cdot \frac{I_{s,1}^2}{I_e^2} + mI_e^2 \cdot \Delta T_e^2 \cdot \frac{I_{s,1}^4}{I_e^6}} \tag{6.8}$$

where mT_1, mT_e, and mI_e are the errors of ΔT_1, T_e, and I_e, respectively. From (6.8), the tolerance of the measured temperature rise can be calculated.

Fig. 6.22 shows the experimental results including tolerances as well as the temperature rise calculated by FEA.
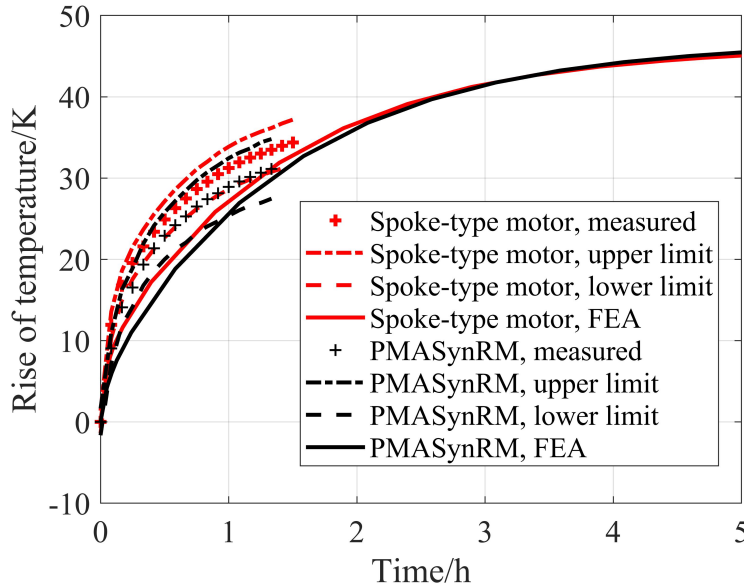
Fig. 6.22 Comparison of estimated temperature rises at operating point 1.

In Fig. 6.22, it can be summarized as:

- Taking into account the tolerances of measurement, both motors do not show significant differences in temperature rise at operating point 1.

- For a measurement with a better precision, the thermal tests must be carried out directly at given operating points. A matching inverter is then required.

- The 3D FEA in this thesis gave a rough estimation of temperature rise. A more sophisticated model is required for a better precision, e.g. a winding model with multiple layers of conductors and insulation.

6.6 Summary

The measured and calculted values for no load EMF coincide well when respecting a reduction of about 10% due to the damages during manufacturing for the spoke-type motor, which was taken into consideration by an adapted analysis. The no load tests validate the correctness of magnetic field calculation for both motors.

Short-circuit and load tests have also been carried out with adjustable resistors. The results are however not satisfying. The main reasons are, that the rotation speed of the prime mover was not stable, and that the error of the angle measurement system was higher than expected.

No load tests at $550 \, \text{min}^{-1}$ were repeated after the short-circuit tests: the results show that no significant irreversible demagnetization occurred during short-circuit test.

The results of thermal tests have been extrapolated and compared to those from FEA. The 3D thermal model gave a rough prediction of thermal behaviour for both motors. To improve the precision, a more sophisticated model is required.

In summary, the intended tests could not be carried out completely due to a damage of the test bench at high speed: the results of short-circuit and load tests are not satisfying with larger errors than expected, while those of other tests validate the analyses in this thesis.

7

Conclusions and Suggestions for Future work

7.1 Summary and Conclusions

7.1.1 Overview of Work in This Thesis

Nowadays, permanent magnet synchronous motors (PMSMs) with rare-earth magnets are widely used in the industry as this kind of motor can achieve satisfying performance in terms of e.g. high efficiency, torque density, and power density. The main problems of this kind of motor are high cost and unstable supply of rare-earth material as well as limited speed range due to poor field-weakening performance. This thesis investigated two variants of interior permanent-magnet synchronous motors (IPMSMs) with ferrite magnets: spoke-type synchronous motors and permanent-magnet assisted synchronous reluctance motors (PMASynRMs), which are potential candidates for replacing PMSMs with rare-earth magnets in applications, where high efficiency and wide speed range are required, such as home appliances and electric vehicles.

In Chapter 3, an automatic optimization procedure was set up by using parametric FE models and various optimization algorithms. For each design, two typical operating points were considered, representing low- and high-speed operation, respectively. A fitness function was then defined to evaluate the quality of each design. By using penalty functions, a list of constraints was taken into consideration, which were classified into several priority levels by different penalty coefficients. Three algorithms including genetic algorithms, the Nelder-Mead method, and the quasi-Newton method, as well as reasonable combinations were discussed. The combination of a genetic algorithm and the Nelder-Mead method was chosen as the final solution.

Chapter 4 was focused on design aspects of spoke-type synchronous motors. Different rotor layouts were investigated in aspects of mechanical reliability and resilience against demagnetization, based on which a design with one-piece sheets and flux barriers on both magnet sides in radial direction was finally selected. Differences between single- and double-layer configurations were also investigated with the conclusion that the latter had better resilience against demagnetization, which was caused by the reduction of 2-pole subharmonic component of stator MMF. Effects of axial rotor stack extension were also investigated.

Chapter 5 presented design aspects of PMASynRMs. For the final design, mechanical, and electromagnetic, and thermal analyses were carried out before the manufacturing.

A test bench was set up for both prototypes in Chapter 6. No load, short-circuit, load, and thermal tests were carried out, which validated feasibility of the design procedure and simulation methods of this thesis.

7.1.2 Conclusions

Following conclusions can be drawn from this thesis:

- A combination of a genetic algorithm for finding the region of global optimum followed with a Nelder-Mead method for finer search, and a continuation with a reduced set of variables after sufficient approach of integer parameters proved to be the best method of optimization.

- A double-layer winding in a 12/10 motor reduces significantly the 2-pole harmonic and thus contributes to better resilience against demagnetization.

- Due to more feasible poles, spoke-type motors achieve higher torque density, lower size, and less torque ripple at low speed. They however suffer from a relatively low power factor and require rather high frequency. Both motors have promising resilience against irreversible demagnetization.

- Both motors meet the requirements of the application in this thesis. Because a low torque ripple is essential for a washing machine, the spoke-type motor is more suitable.

- The temperature rises of both motors are about $45\,\mathrm{K}$. Even assuming a water temperature of $90\,°\mathrm{C}$ inside the washing machine, insulation class F155 leaves some reserve that can reduce the size of the slots.

- In general, the results of experiments and FEA validate the feasibility of the design procedure and simulation methods in this thesis, although the results of short-circuit and load tests are not satisfying.

7.2   Suggestions for Future Work

Future optimization procedures could cover more variables including mechanical and thermal issues at the expense of more computation capacity.

A design with wedged iron segments inserted into a non-magnetic ring would outperform the realized spoke-type motor.

The application of double-layer single-tooth windings for slot-pole combinations should be examined for more configurations even where this is not required, since this measure can suppress subharmonics efficiently.

Within mechanical limits, designs with axially extended rotor stacks also require more attention.

A reduction of torque ripple of the PMASynRM can be achieved by variation of the slope angle of the magnets at the outer side of poles for more sinusoidal field, by closing the stator slots, or by skewing stator or rotor by further optimization routines.

Lower size of the motor can be achieved by application of better grades of permanent magnet material, namely modern ferrites containing Lanthanium with better coercivity at low temperature.

Further applications can be considered, e.g. refrigerators with low noise, EVs with a wide speed range and high efficiency, and robots with low torque ripple.

A

Results of Short-circuit and Load Tests

A.1 Tests of the Spoke-type Motor

The results of short-circuit and load tests of the spoke motor are given in Figs. A.1, A.2, and A.3.
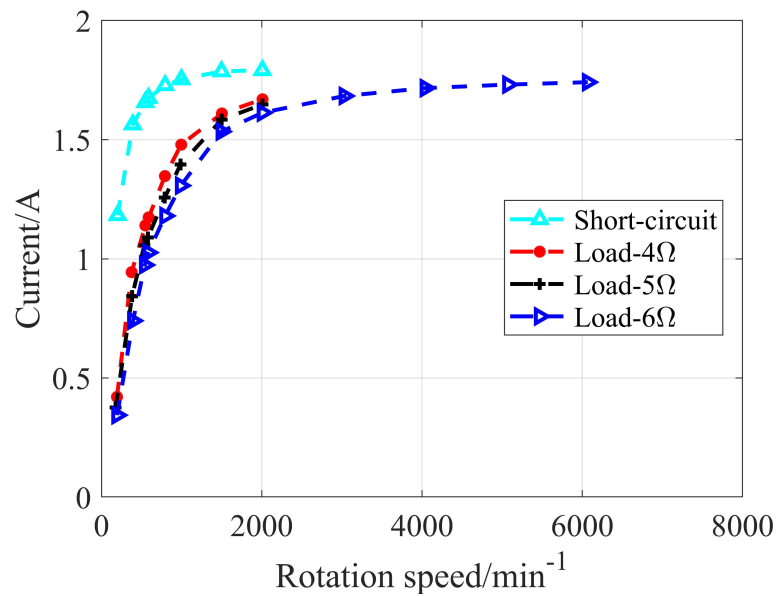
Fig. A.1 RMS value of stator current of the spoke-type motor at different speeds.
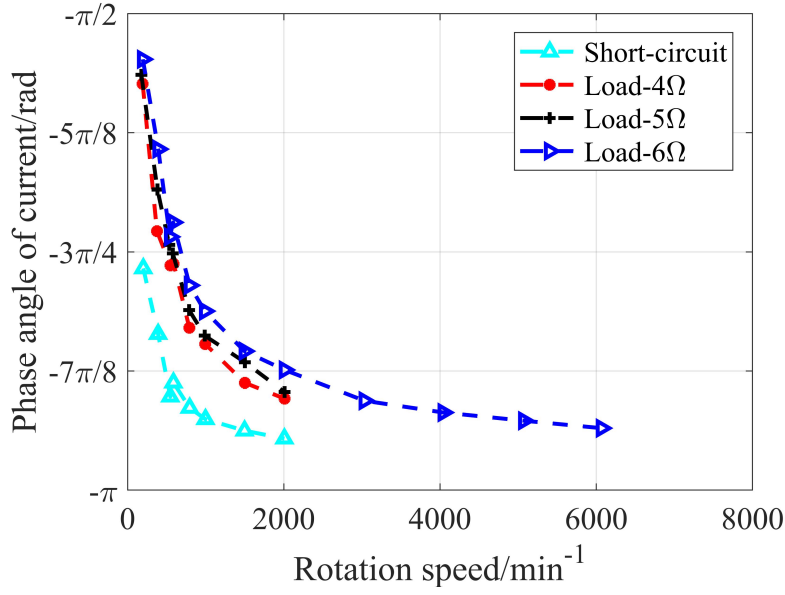
Fig. A.2 Phase angle of stator current of the spoke-type motor at different speeds.
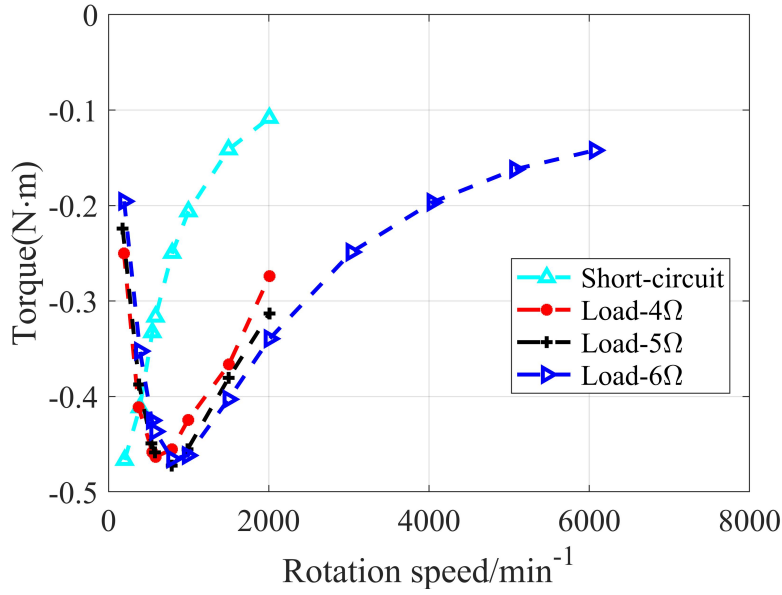
Fig. A.3 Torque of the spoke-type motor in short-circuit and load tests at different speeds.

A.2 Tests of the Permanent-magnet Assisted Synchronous Reluctance Motor

The results of short-circuit and load tests of the permanent-magnet assisted synchronous reluctance motor (PMASynRM) are given in Figs. A.4, A.5, and A.6.
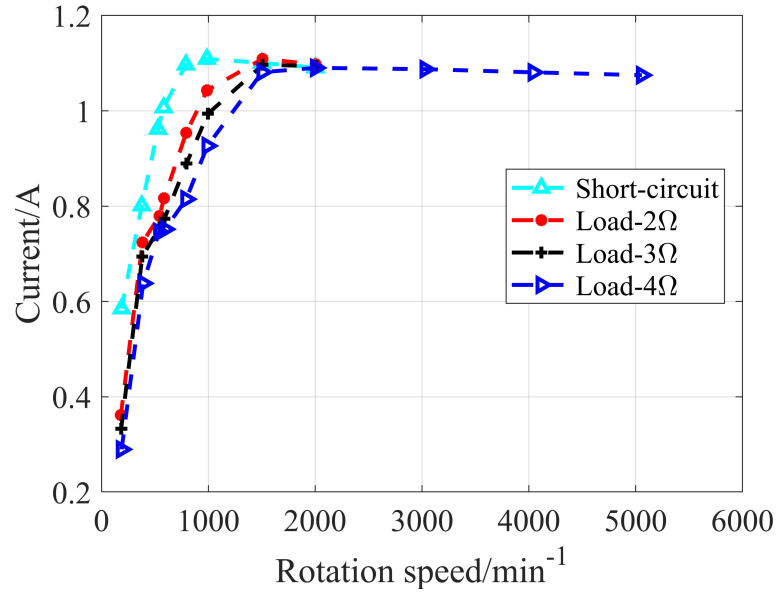
Fig. A.4 RMS value of stator current of the PMASynRM at different speeds.
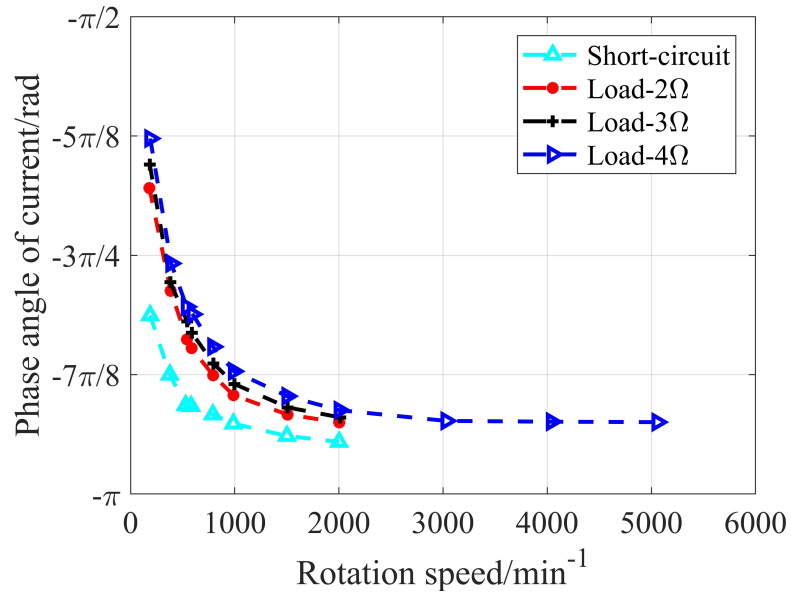
Fig. A.5 Phase angle of stator current of the PMASynRM at different speeds.
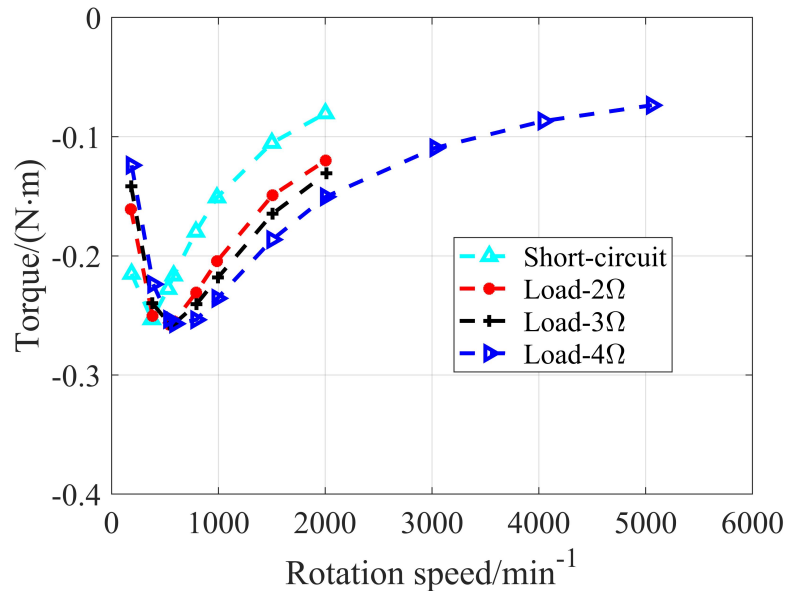
Fig. A.6 Torque of the PMASynRM in short-circuit and load tests at different speeds.

B

Results of Inductances

B.1 Results of the Spoke-type Motor

The inductances of the spoke-type motor calculated from test results are given in Figs. B.1 and B.2. Each point in the figures represents a test point.
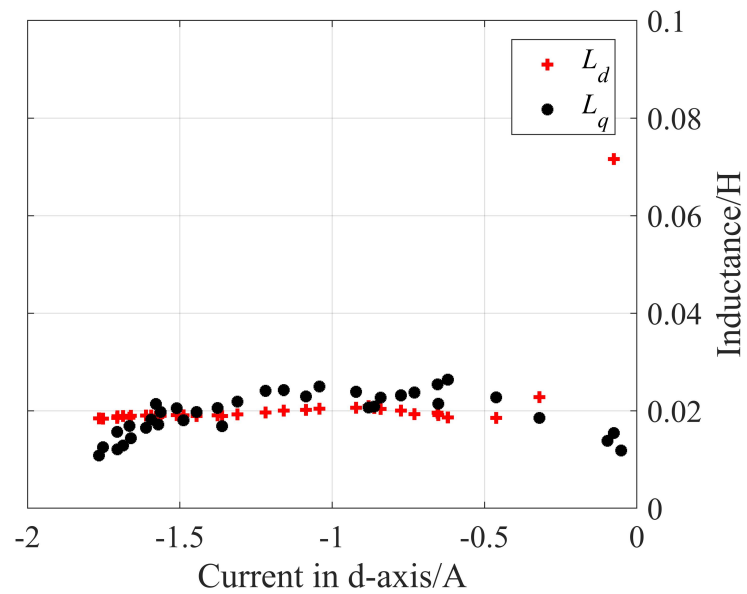
Fig. B.1 Inductances of the spoke-type motor vs. current in d-axis.
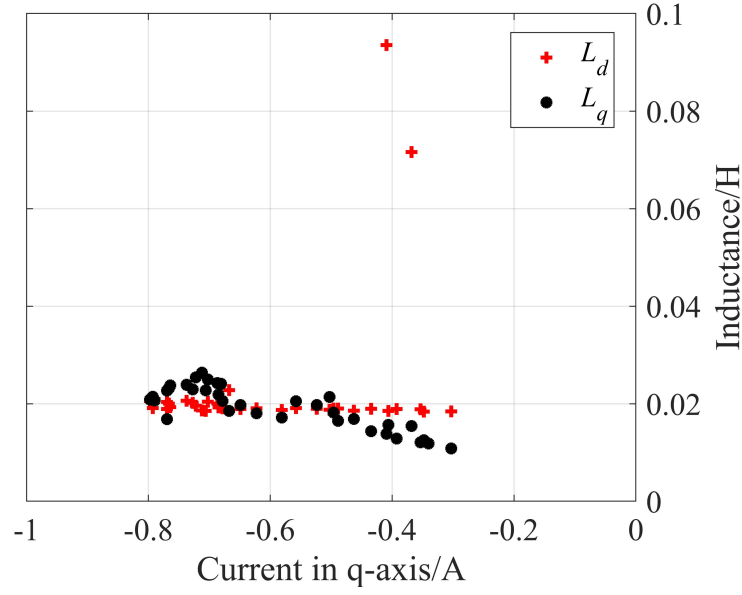
Fig. B.2 Inductances of the spoke-type motor vs. current in q-axis.

B.2 Results of the Permanent-magnet Assisted Synchronous Reluctance Motor

The inductances of the permanent-magnet assisted synchronous reluctance motor (PMASynRM) calculated from test results are given in Figs. B.3 and B.4. Each point in the figures represents a test point.
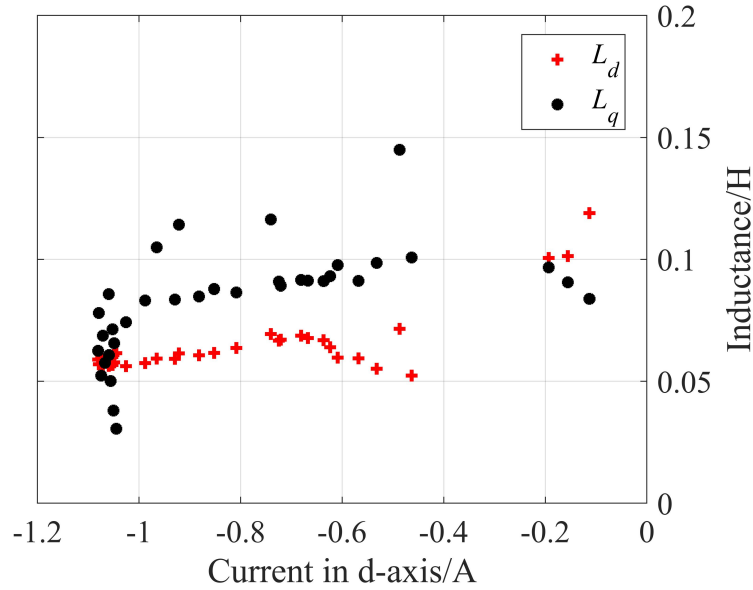
Fig. B.3 Inductances of the PMASynRM vs. current in d-axis.
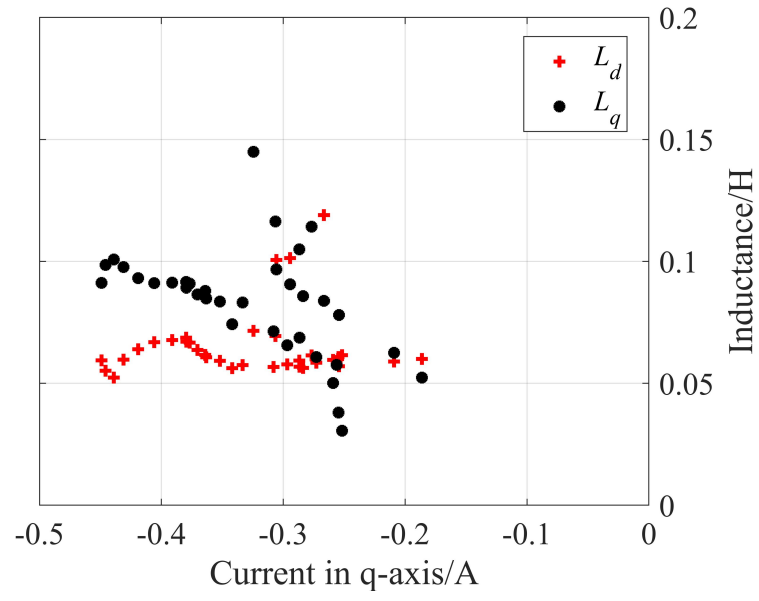
Fig. B.4 Inductances of the PMASynRM vs. current in q-axis.

References

[1] P. Pfister and Y. Perriard, "Very-high-speed slotless permanent-magnet motors: Analytical modeling, optimization, design, and torque measurement methods", *IEEE Transactions on Industrial Electronics*, vol. 57, no. 1, pp. 296–303, 2010.

[2] J. Pyrhonen, J. Nerg, P. Kurronen, and U. Lauber, "High-speed high-output solid-rotor induction-motor technology for gas compression", *IEEE Transactions on Industrial Electronics*, vol. 57, no. 1, pp. 272–280, 2010.

[3] F. Zhang, G. Du, T. Wang, F. Wang, W. Cao, and J. L. Kirtley, "Electromagnetic design and loss calculations of a 1.12-MW high-speed permanent-magnet motor for compressor applications", *IEEE Transactions on Energy Conversion*, vol. 31, no. 1, pp. 132–140, 2016.

[4] V. Mallard, G. Parent, C. Demian, J. Brudny, and A. Delamotte, "Increasing the energy efficiency of induction machines by the use of grain-oriented magnetic materials and die casting copper squirrel cage in the rotor", *IEEE Transactions on Industry Applications*, vol. 55, no. 2, pp. 1280–1289, 2019.

[5] A. T. De Almeida, F. J. T. E. Ferreira, and A. Q. Duarte, "Technical and economical considerations on super high-efficiency three-phase motors", *IEEE Transactions on Industry Applications*, vol. 50, no. 2, pp. 1274–1285, 2014.

[6] M. Popescu, J. Goss, D. A. Staton, D. Hawkins, Y. C. Chong, and A. Boglietti, "Electrical vehicles—practical solutions for power traction motor systems", *IEEE Transactions on Industry Applications*, vol. 54, no. 3, pp. 2751–2762, 2018.

[7] I. Boldea, L. Tutelea, and C. I. Pitic, "PM-assisted reluctance synchronous motor/generator (PM-RSM) for mild hybrid vehicles: Electromagnetic design", *IEEE Transactions on Industry Applications*, vol. 40, no. 2, pp. 492–498, 2004.

[8] M. Takeno, A. Chiba, N. Hoshi, S. Ogasawara, M. Takemoto, and M. A. Rahman, "Test results and torque improvement of the 50-kW switched reluctance motor designed for hybrid electric vehicles", *IEEE Transactions on Industry Applications*, vol. 48, no. 4, pp. 1327–1334, 2012.

[9] S. Morimoto, S. Ooi, Y. Inoue, and M. Sanada, "Experimental evaluation of a rare-earth-free PMASynRM with ferrite magnets for automotive applications", *IEEE Transactions on Industrial Electronics*, vol. 61, no. 10, pp. 5749–5756, 2014.

REFERENCES

[10] S. Kim, S. Park, T. Park, J. Cho, W. Kim, and S. Lim, "Investigation and experimental verification of a novel spoke-type ferrite-magnet motor for electric-vehicle traction drive applications", *IEEE Transactions on Industrial Electronics*, vol. 61, no. 10, pp. 5763–5770, 2014.

[11] A. Murray, M. Palma, and A. Husain, "Performance comparison of permanent magnet synchronous motors and controlled induction motors in washing machine applications using sensorless field oriented control", in *2008 IEEE Industry Applications Society Annual Meeting*, 2008, pp. 1–6.

[12] H. Ahn and D. Lee, "A new bumpless rotor-flux position estimation scheme for vector-controlled washing machine", *IEEE Transactions on Industrial Informatics*, vol. 12, no. 2, pp. 466–473, 2016.

[13] Z. Zhang, H. Xu, L. Xu, and L. E. Heilman, "Sensorless direct field-oriented control of three-phase induction motors based on "sliding mode"for washing-machine drive applications", *IEEE Transactions on Industry Applications*, vol. 42, no. 3, pp. 694–701, 2006.

[14] A. Yoo, S. Sul, D. Lee, and C. Jun, "Novel speed and rotor position estimation strategy using a dual observer for low-resolution position sensors", *IEEE Transactions on Power Electronics*, vol. 24, no. 12, pp. 2897–2906, 2009.

[15] A. Dianov and S. Lee, "Novel IPMSM drive for compact washing machine", in *INTELEC 2009 - 31st International Telecommunications Energy Conference*, 2009, pp. 1–7.

[16] W. Lee, S. Park, J. Lee, Y. Kim, and C. Won, "Control of IPMSM drive system for drum washing machine", in *2007 7th Internatonal Conference on Power Electronics*, 2007, pp. 930–935.

[17] R. Filka, P. Balazovic, and B. Dobrucky, "Transducerless speed control with initial position detection for low cost PMSM drives", in *2008 13th International Power Electronics and Motion Control Conference*, 2008, pp. 1402–1408.

[18] P. Guglielmi, M. Pastorelli, A. Carrer, A. Beato, D. D'Antonio, and L. Fagnano, "An IPM-PMASR motor for home appliance washing machines", in *IECON 2013 - 39th Annual Conference of the IEEE Industrial Electronics Society*, 2013, pp. 2608–2613.

[19] M. Kalkat, "Experimentally vibration and noise analysis of two types of washing machines with a proposed neural network predictor", *Measurement*, vol. 47, pp. 184–192, 2014.

[20] S. Chi, Z. Zhang, and L. Xu, "Sliding-mode sensorless control of direct-drive PM synchronous motors for washing machine applications", *IEEE Transactions on Industry Applications*, vol. 45, no. 2, pp. 582–590, 2009.

[21] A. Dianov, Nam Su Kim, and Seung Moo Lim, "Sensorless starting of horizontal axis washing machines with direct drive", in *2013 International Conference on Electrical Machines and Systems (ICEMS)*, 2013, pp. 1–6.

[22] C. Suciu, R. Campeanu, A. Campeanu, I. Margineanu, and A. Danila, "A virtual instrumentation-based on-line determination of a single/two phase induction motor drive characteristics at coarse start-up", in *2008 IEEE International Conference on Automation, Quality and Testing, Robotics*, vol. 3, 2008, pp. 440–443.

[23] A. Nied, J. de Oliveira, L. H. R. C. Stival, and H. B. Polli, "Improving washing machine performance using single-phase induction motor field-oriented control", in *IECON 2013 - 39th Annual Conference of the IEEE Industrial Electronics Society*, 2013, pp. 2917–2922.

[24] G. Schroder, J. Bekiesch, and H. Siebel, "AC-fed universal motor with open loop speed control and PFC", in *IECON'03. 29th Annual Conference of the IEEE Industrial Electronics Society*, vol. 1, 2003, 705–708 vol.1.

[25] H. S. Rajamani and R. A. McMahon, "Universal and high-speed, three phase induction motor drives for domestic appliances", in *Proceedings of IEEE. AFRICON '96*, vol. 1, 1996, 441–446 vol.1.

[26] J. S. Moghani and M. Heidari, "High efficient low cost induction motor drive for residential applications", in *International Symposium on Power Electronics, Electrical Drives, Automation and Motion, 2006. SPEEDAM 2006*, 2006, pp. 1399–1402.

[27] H. S. Rajamani and R. A. McMahon, "Induction motor drives for domestic appliances", *IEEE Industry Applications Magazine*, vol. 3, no. 3, pp. 21–26, 1997.

[28] N. Balkan Simsir and H. Bulent Ertan, "A comparison of torque capabilities of axial flux and radial flux type of brushless DC (BLDC) drives for wide speed range applications", in *Proceedings of the IEEE 1999 International Conference on Power Electronics and Drive Systems. PEDS'99*, vol. 2, 1999, 719–724 vol.2.

[29] D. Kamalakannan, V. Mariappan, V. Narayanan, and N. S. Ramanathan, "Energy efficient appliances in a residential building", in *2016 First International Conference on Sustainable Green Buildings and Communities (SGBC)*, 2016, pp. 1–6.

[30] C. Jin, D. Jung, K. Kim, Y. Chun, H. Lee, and J. Lee, "A study on improvement magnetic torque characteristics of IPMSM for direct drive washing machine", *IEEE Transactions on Magnetics*, vol. 45, no. 6, pp. 2811–2814, 2009.

[31] B. Kim and T. A. Lipo, "Design of a surface PM vernier motor for a practical variable speed application", in *2015 IEEE Energy Conversion Congress and Exposition (ECCE)*, 2015, pp. 776–783.

REFERENCES

[32] E. Armando, P. Guglielmi, M. Pastorelli, G. Pellegrino, and A. Vagati, "Performance of IPM-PMASR motors with ferrite injection for home appliance washing machine", in *2008 IEEE Industry Applications Society Annual Meeting*, 2008, pp. 1–6.

[33] Z. Q. Zhu and J. H. Leong, "Analysis and mitigation of torsional vibration of pm brushless AC/DC drives with direct torque controller", *IEEE Transactions on Industry Applications*, vol. 48, no. 4, pp. 1296–1306, 2012.

[34] G. Jeong, Z. Xu, and J. Ahn, "Design of SRM considering dual drive modes", in *2014 IEEE International Conference on Industrial Technology (ICIT)*, 2014, pp. 872–876.

[35] M. Asgar, E. Afjei, A. Behbahani, and A. Siadatan, "A 12/8 double-stator switched reluctance motor for washing machine application", in *The 6th Power Electronics, Drive Systems Technologies Conference (PEDSTC2015)*, 2015, pp. 168–172.

[36] S. M. Castano, R. Yang, C. Mak, B. Bilgin, and A. Emadi, "External-rotor switched reluctance motor for direct-drive home appliances", in *IECON 2018 - 44th Annual Conference of the IEEE Industrial Electronics Society*, 2018, pp. 514–521.

[37] R. Bojoi, B. He, F. Rosa, and F. Pegoraro, "Sensorless direct flux and torque control for direct drive washing machine applications", in *2011 IEEE Energy Conversion Congress and Exposition*, 2011, pp. 347–354.

[38] H. Kim, S. Yi, N. Kim, and R. D. Lorenz, "Using low resolution position sensors in bumpless position/speed estimation methods for low cost PMSM drives", in *Fourtieth IAS Annual Meeting. Conference Record of the 2005 Industry Applications Conference, 2005*, vol. 4, 2005, pp. 2518–2525.

[39] H. Kim, "On-line mechanical unbalance estimation for permanent magnet synchronous machine drives", *IET Electric Power Applications*, vol. 3, no. 3, pp. 178–186, 2009.

[40] T. M. Jahns, "Flux-weakening regime operation of an interior permanent-magnet synchronous motor drive", *IEEE Transactions on Industry Applications*, vol. IA-23, no. 4, pp. 681–689, 1987.

[41] E. Armando, P. Guglielmi, G. Pellegrino, M. Pastorelli, and A. Vagati, "Accurate modeling and performance analysis of IPM-PMASR motors", *IEEE Transactions on Industry Applications*, vol. 45, no. 1, pp. 123–130, 2009.

[42] Byoung-Kuk Lee, Gyu-Hong Kang, Jin Hur, and Dong-Wook You, "Design of spoke type BLDC motors with high power density for traction applications", in *Conference Record of the 2004 IEEE Industry Applications Conference, 2004. 39th IAS Annual Meeting*, vol. 2, 2004, pp. 1068–1074.

[43] J. S. Yoo, H. Jang, S. Cho, G. S. Lee, S. Ko, S. Bae, H. Lee, H. Liu, J. Lee, and H. So, "Design of rotor with novel barrier for power improvement of spoke-type permanent magnet synchronous motor", in *2018 21st International Conference on Electrical Machines and Systems (ICEMS)*, 2018, pp. 252–255.

[44] M. van der Giet, E. Lange, D. A. P. Corrêa, I. E. Chabu, S. I. Nabeta, and K. Hameyer, "Acoustic simulation of a special switched reluctance drive by means of field–circuit coupling and multiphysics simulation", *IEEE Transactions on Industrial Electronics*, vol. 57, no. 9, pp. 2946–2953, 2010.

[45] B. Bilgin, A. Emadi, and M. Krishnamurthy, "Design considerations for switched reluctance machines with a higher number of rotor poles", *IEEE Transactions on Industrial Electronics*, vol. 59, no. 10, pp. 3745–3756, 2012.

[46] A. T. de Almeida, F. J. T. E. Ferreira, J. A. C. Fong, and C. U. Brunner, "Electric motor standards, ecodesign and global market transformation", in *2008 IEEE/IAS Industrial and Commercial Power Systems Technical Conference*, 2008, pp. 1–9.

[47] A. T. de Almeida, F. J. T. E. Ferreira, and G. Baoming, "Beyond induction motors—technology trends to move up efficiency", *IEEE Transactions on Industry Applications*, vol. 50, no. 3, pp. 2103–2114, 2014.

[48] N. Bianchi, S. Bolognani, and A. Faggion, "A ringed-pole SPM motor for sensorless drives - electromagnetic analysis, prototyping and tests", in *2010 IEEE International Symposium on Industrial Electronics*, 2010, pp. 1193–1198.

[49] G. Pellegrino, A. Vagati, B. Boazzo, and P. Guglielmi, "Comparison of induction and PM synchronous motor drives for EV application including design examples", *IEEE Transactions on Industry Applications*, vol. 48, no. 6, pp. 2322–2332, 2012.

[50] R. Dutta, L. Chong, and M. F. Rahman, "Design and experimental verification of an 18-slot/14-pole fractional-slot concentrated winding interior permanent magnet machine", *IEEE Transactions on Energy Conversion*, vol. 28, no. 1, pp. 181–190, 2013.

[51] S. Chung, J. Kim, Y. Chun, B. Woo, and D. Hong, "Fractional slot concentrated winding PMSM with consequent pole rotor for a low-speed direct drive: Reduction of rare earth permanent magnet", *IEEE Transactions on Energy Conversion*, vol. 30, no. 1, pp. 103–109, 2015.

[52] P. Guglielmi, B. Boazzo, E. Armando, G. Pellegrino, and A. Vagati, "Permanent-magnet minimization in PM-assisted synchronous reluctance motors for wide speed range", *IEEE Transactions on Industry Applications*, vol. 49, no. 1, pp. 31–41, 2013.

REFERENCES

[53] O. Payza, Y. Demir, and M. Aydin, "Investigation of losses for a concentrated winding high-speed permanent magnet-assisted synchronous reluctance motor for washing machine application", *IEEE Transactions on Magnetics*, vol. 54, no. 11, pp. 1–5, 2018.

[54] N. Bianchi, S. Bolognani, E. Carraro, M. Castiello, and E. Fornasiero, "Electric vehicle traction based on synchronous reluctance motors", *IEEE Transactions on Industry Applications*, vol. 52, no. 6, pp. 4762–4769, 2016.

[55] A. Tap, L. Xheladini, M. Yilmaz, M. Imeryuz, T. Asan, and L. T. Ergene, "Comprehensive design and analysis of a PMaSynRM for washing machine applications", *IET Electric Power Applications*, vol. 12, no. 9, pp. 1311–1319, 2018.

[56] H. Chen and J. J. Gu, "Switched reluctance motor drive with external rotor for fan in air conditioner", *IEEE/ASME Transactions on Mechatronics*, vol. 18, no. 5, pp. 1448–1458, 2013.

[57] T. Jahns, "Getting rare-earth magnets out of EV traction machines: A review of the many approaches being pursued to minimize or eliminate rare-earth magnets from future EV drivetrains", *IEEE Electrification Magazine*, vol. 5, no. 1, pp. 6–18, 2017.

[58] J. Lee and B. Kwon, "Optimal rotor shape design of a concentrated flux IPM-type motor for improving efficiency and operation range", *IEEE Transactions on Magnetics*, vol. 49, no. 5, pp. 2205–2208, 2013.

[59] R. P. D. D. A. Staton W. L. Soong and T. J. E. Miller, "Unified theory of torque production in AC, DC and reluctance motors", in *Proceedings of 1994 IEEE Industry Applications Society Annual Meeting*, 1994, pp. 149–156.

[60] R. Belmans, D. Verdyck, and W. Geysen, "Optimization of permanent magnet machines with respect to torque and audible noise", in *1989 Fourth International Conference on Electrical Machines and Drives)*, 1989, pp. 80–84.

[61] W. Kakihara, M. Takemoto, and S. Ogasawara, "Rotor structure in 50 kW spoke-type interior permanent magnet synchronous motor with ferrite permanent magnets for automotive applications", in *2013 IEEE Energy Conversion Congress and Exposition*, 2013, pp. 606–613.

[62] X. Ge, Z. Q. Zhu, J. Li, and J. Chen, "A spoke-type IPM machine with novel alternate airspace barriers and reduction of unipolar leakage flux by step-staggered rotor", *IEEE Transactions on Industry Applications*, vol. 52, no. 6, pp. 4789–4797, 2016.

[63] S. Sashidhar and B. G. Fernandes, "A novel ferrite SMDS spoke-type BLDC motor for PV bore-well submersible water pumps", *IEEE Transactions on Industrial Electronics*, vol. 64, no. 1, pp. 104–114, 2017.

[64] X. Liu, H. Chen, J. Zhao, and A. Belahcen, "Research on the performances and parameters of interior PMSM used for electric vehicles", *IEEE Transactions on Industrial Electronics*, vol. 63, no. 6, pp. 3533–3545, 2016.

[65] W. Zhao, T. A. Lipo, and B. Kwon, "Comparative study on novel dual stator radial flux and axial flux permanent magnet motors with ferrite magnets for traction application", *IEEE Transactions on Magnetics*, vol. 50, no. 11, pp. 1–4, 2014.

[66] Z. S. Du and T. A. Lipo, "Torque performance comparison between a ferrite magnet vernier motor and an industrial interior permanent magnet machine", *IEEE Transactions on Industry Applications*, vol. 53, no. 3, pp. 2088–2097, 2017.

[67] M. Kimiabeigi, J. D. Widmer, R. Long, Y. Gao, J. Goss, R. Martin, T. Lisle, J. M. Soler Vizan, A. Michaelides, and B. Mecrow, "High-performance low-cost electric motor for electric vehicles using ferrite magnets", *IEEE Transactions on Industrial Electronics*, vol. 63, no. 1, pp. 113–122, 2016.

[68] M. Kimiabeigi, R. Long, J. D. Widmer, and Y. Gao, "Comparative assessment of single piece and fir-tree-based spoke type rotor designs for low-cost electric vehicle application", *IEEE Transactions on Energy Conversion*, vol. 32, no. 2, pp. 486–494, 2017.

[69] M. Si, X. Yu Yang, S. Wei Zhao, and S. Gong, "Design and analysis of a novel spoke-type permanent magnet synchronous motor", *IET Electric Power Applications*, vol. 10, no. 6, pp. 571–580, 2016.

[70] M. Ibrahim, L. Masisi, and P. Pillay, "Design of variable flux permanent-magnet machine for reduced inverter rating", *IEEE Transactions on Industry Applications*, vol. 51, no. 5, pp. 3666–3674, 2015.

[71] M. R. Mohammad, K. Kim, and J. Hur, "Design and analysis of a spoke type motor with segmented pushing permanent magnet for concentrating air-gap flux density", *IEEE Transactions on Magnetics*, vol. 49, no. 5, pp. 2397–2400, 2013.

[72] M. M. Rahman, K. Kim, and J. Hur, "Design and optimization of neodymium-free spoke-type motor with segmented wing-shaped PM", *IEEE Transactions on Magnetics*, vol. 50, no. 2, pp. 865–868, 2014.

[73] X. Zhu, X. Wang, C. Zhang, L. Wang, and W. Wu, "Design and analysis of a spoke-type hybrid permanent magnet motor for electric vehicles", *IEEE Transactions on Magnetics*, vol. 53, no. 11, pp. 1–4, 2017.

[74] Q. Chen, G. Xu, F. Zhai, and G. Liu, "A novel spoke-type PM motor with auxiliary salient poles for low torque pulsation", *IEEE Transactions on Industrial Electronics*, vol. 67, no. 6, pp. 4762–4773, 2020.

REFERENCES

[75] A. Tessarolo, M. Mezzarobba, and R. Menis, "Modeling, analysis, and testing of a novel spoke-type interior permanent magnet motor with improved flux weakening capability", *IEEE Transactions on Magnetics*, vol. 51, no. 4, pp. 1–10, 2015.

[76] S. Kim, J. Cho, S. Park, T. Park, and S. Lim, "Characteristics comparison of a conventional and modified spoke-type ferrite magnet motor for traction drives of low-speed electric vehicles", *IEEE Transactions on Industry Applications*, vol. 49, no. 6, pp. 2516–2523, 2013.

[77] P. Liang, F. Chai, Y. Yu, and L. Chen, "Analytical model of a spoke-type permanent magnet synchronous in-wheel motor with trapezoid magnet accounting for tooth saturation", *IEEE Transactions on Industrial Electronics*, vol. 66, no. 2, pp. 1162–1171, 2019.

[78] K. Boughrara, R. Ibtiouen, and T. Lubin, "Analytical prediction of magnetic field in parallel double excitation and spoke-type permanent-magnet machines accounting for tooth-tips and shape of polar pieces", *IEEE Transactions on Magnetics*, vol. 48, no. 7, pp. 2121–2137, 2012.

[79] Q. Chen, G. Liu, W. Zhao, and M. Shao, "Nonlinear adaptive lumped parameter magnetic circuit analysis for spoke-type fault-tolerant permanent-magnet motors", *IEEE Transactions on Magnetics*, vol. 49, no. 9, pp. 5150–5157, 2013.

[80] S. G. Lee, J. Lee, and W. Kim, "A study on correcting the nonlinearity between stack length and back electromotive force in spoke type ferrite magnet motors", *IEEE Transactions on Magnetics*, vol. 53, no. 6, pp. 1–4, 2017.

[81] J. Song, J. H. Lee, Y. Kim, and S. Jung, "Computational method of effective remanence flux density to consider PM overhang effect for spoke-type PM motor with 2-D analysis using magnetic energy", *IEEE Transactions on Magnetics*, vol. 52, no. 3, pp. 1–4, 2016.

[82] H. Kim, K. Kim, Y. Jo, and J. Hur, "Optimization methods of torque density for developing the neodymium free spoke-type BLDC motor", *IEEE Transactions on Magnetics*, vol. 49, no. 5, pp. 2173–2176, 2013.

[83] K. Hwang, S. Rhee, B. Yang, and B. Kwon, "Rotor pole design in spoke-type brushless DC motor by response surface method", *IEEE Transactions on Magnetics*, vol. 43, no. 4, pp. 1833–1836, 2007.

[84] K. Y. Hwang, J. H. Jo, and B. I. Kwon, "A study on optimal pole design of spoke-type IPMSM with concentrated winding for reducing the torque ripple by experiment design method", *IEEE Transactions on Magnetics*, vol. 45, no. 10, pp. 4712–4715, 2009.

[85] W. Zhao, J. Kwon, X. Wang, T. A. Lipo, and B. Kwon, "Optimal design of a spoke-type permanent magnet motor with phase-group concentrated-coil windings to minimize torque pulsations", *IEEE Transactions on Magnetics*, vol. 53, no. 6, pp. 1–4, 2017.

[86] P. Zhang, G. Y. Sizov, D. M. Ionel, and N. A. O. Demerdash, "Establishing the relative merits of interior and spoke-type permanent-magnet machines with ferrite or NdFeB through systematic design optimization", *IEEE Transactions on Industry Applications*, vol. 51, no. 4, pp. 2940–2948, 2015.

[87] P. Zhang, G. Y. Sizov, D. M. Ionel, and N. A. O. Demerdash, "Design optimization of spoke-type ferrite magnet machines by combined design of experiments and differential evolution algorithms", in *2013 International Electric Machines Drives Conference*, 2013, pp. 892–898.

[88] D. Y. Kim, J. K. Nam, and G. H. Jang, "Reduction of magnetically induced vibration of a spoke-type IPM motor using magnetomechanical coupled analysis and optimization", *IEEE Transactions on Magnetics*, vol. 49, no. 9, pp. 5097–5105, 2013.

[89] S. J. Galioto, P. B. Reddy, A. M. EL-Refaie, and J. P. Alexander, "Effect of magnet types on performance of high-speed spoke interior-permanent-magnet machines designed for traction applications", *IEEE Transactions on Industry Applications*, vol. 51, no. 3, pp. 2148–2160, 2015.

[90] M. Kimiabeigi, J. D. Widmer, R. S. Sheridan, A. Walton, and R. Harris, "Design of high performance traction motors using cheaper grade of materials", in *8th IET International Conference on Power Electronics, Machines and Drives (PEMD 2016)*, 2016, pp. 1–7.

[91] M. Ibrahim, L. Masisi, and P. Pillay, "Design of variable-flux permanent-magnet machines using alnico magnets", *IEEE Transactions on Industry Applications*, vol. 51, no. 6, pp. 4482–4491, 2015.

[92] M. Kimiabeigi, J. D. Widmer, R. Long, Y. Gao, J. Goss, R. Martin, T. Lisle, J. M. S. Vizan, A. Michaelides, and B. C. Mecrow, "On selection of rotor support material for a ferrite magnet spoke-type traction motor", *IEEE Transactions on Industry Applications*, vol. 52, no. 3, pp. 2224–2233, 2016.

[93] C. Jun and B. Kwon, "Performance comparison of a spoke-type PM motor with different permanent magnet shapes and the same magnet volume", *IET Electric Power Applications*, vol. 11, no. 7, pp. 1196–1204, 2017.

[94] E. Carraro, N. Bianchi, S. Zhang, and M. Koch, "Design and performance comparison of fractional slot concentrated winding spoke type synchronous motors with different slot-pole combinations", *IEEE Transactions on Industry Applications*, vol. 54, no. 3, pp. 2276–2284, 2018.

REFERENCES

[95] M. Popescu and D. G. Dorrell, "Proximity losses in the windings of high speed brushless permanent magnet AC motors with single tooth windings and parallel paths", *IEEE Transactions on Magnetics*, vol. 49, no. 7, pp. 3913–3916, 2013.

[96] P. Liang, Y. Tang, F. Chai, K. Shen, and W. Liu, "Calculation of the iron losses in a spoke-type permanent magnet synchronous in-wheel motor for electric vehicles by utilizing the bertotti model", *IEEE Transactions on Magnetics*, vol. 55, no. 7, pp. 1–7, 2019.

[97] W. Zhao, T. A. Lipo, and B. Kwon, "Torque pulsation minimization in spoke-type interior permanent magnet motors with skewing and sinusoidal permanent magnet configurations", *IEEE Transactions on Magnetics*, vol. 51, no. 11, pp. 1–4, 2015.

[98] D. G. Dorrell, A. M. Knight, L. Evans, and M. Popescu, "Analysis and design techniques applied to hybrid vehicle drive machines—assessment of alternative IPM and induction motor topologies", *IEEE Transactions on Industrial Electronics*, vol. 59, no. 10, pp. 3690–3699, 2012.

[99] S. Cho, H. Ahn, H. c. Liu, H. Hong, J. Lee, and S. Go, "Analysis of inductance according to the applied current in spoke-type PMSM and suggestion of driving mode", *IEEE Transactions on Magnetics*, vol. 53, no. 6, pp. 1–4, 2017.

[100] M. Barcaro, M. Morandin, T. Pradella, N. Bianchi, and I. Furlan, "Iron saturation impact on high-frequency sensorless control of synchronous permanent-magnet motor", *IEEE Transactions on Industry Applications*, vol. 53, no. 6, pp. 5470–5478, 2017.

[101] Y. Burkhardt, A. Spagnolo, P. Lucas, M. Zavesky, and P. Brockerhoff, "Design and analysis of a highly integrated 9-phase drivetrain for EV applications", in *2014 International Conference on Electrical Machines (ICEM)*, 2014, pp. 450–456.

[102] M. Aydin and M. Gulec, "A new coreless axial flux interior permanent magnet synchronous motor with sinusoidal rotor segments", *IEEE Transactions on Magnetics*, vol. 52, no. 7, pp. 1–4, 2016.

[103] W. Zhao, T. A. Lipo, and B. Kwon, "A novel dual-rotor, axial field, fault-tolerant flux-switching permanent magnet machine with high-torque performance", *IEEE Transactions on Magnetics*, vol. 51, no. 11, pp. 1–4, 2015.

[104] F. Zhao, T. A. Lipo, and B. Kwon, "A novel dual-stator axial-flux spoke-type permanent magnet vernier machine for direct-drive applications", *IEEE Transactions on Magnetics*, vol. 50, no. 11, pp. 1–4, 2014.

[105] Z. S. Du and T. A. Lipo, "High torque density ferrite permanent magnet vernier motor analysis and design with demagnetization consideration", in *2015 IEEE Energy Conversion Congress and Exposition (ECCE)*, 2015, pp. 6082–6089.

[106] M. Raza, W. Zhao, T. A. Lipo, and B. Kwon, "Performance comparison of dual airgap and single airgap spoke-type permanent-magnet vernier machines", *IEEE Transactions on Magnetics*, vol. 53, no. 6, pp. 1–4, 2017.

[107] T. Zou, D. Li, R. Qu, and D. Jiang, "Performance comparison of surface and spoke-type flux-modulation machines with different pole ratios", *IEEE Transactions on Magnetics*, vol. 53, no. 6, pp. 1–5, 2017.

[108] M. Tsai and L. Ku, "3-D printing-based design of axial flux magnetic gear for high torque density", *IEEE Transactions on Magnetics*, vol. 51, no. 11, pp. 1–4, 2015.

[109] X. Zhang, X. Liu, and Z. Chen, "A novel dual-flux-modulator coaxial magnetic gear for high torque capability", *IEEE Transactions on Energy Conversion*, vol. 33, no. 2, pp. 682–691, 2018.

[110] K. K. Uppalapati, J. Z. Bird, D. Jia, J. Garner, and A. Zhou, "Performance of a magnetic gear using ferrite magnets for low speed ocean power generation", in *2012 IEEE Energy Conversion Congress and Exposition (ECCE)*, 2012, pp. 3348–3355.

[111] N. Baloch, S. Khaliq, and B. Kwon, "HTS dual-stator spoke-type linear vernier machine for leakage flux reduction", *IEEE Transactions on Magnetics*, vol. 53, no. 11, pp. 1–4, 2017.

[112] Q. Chen, G. Liu, W. Zhao, L. Sun, M. Shao, and Z. Liu, "Design and comparison of two fault-tolerant interior-permanent-magnet motors", *IEEE Transactions on Industrial Electronics*, vol. 61, no. 12, pp. 6615–6623, 2014.

[113] W. Zhao, T. A. Lipo, and B. Kwon, "Dual-stator two-phase permanent magnet machines with phase-group concentrated-coil windings for torque enhancement", *IEEE Transactions on Magnetics*, vol. 51, no. 11, pp. 1–4, 2015.

[114] S. Morimoto, M. Sanada, and Y. Takeda, "Performance of PM assisted synchronous reluctance motor for high efficiency and wide constant power operation", in *Conference Record of the 2000 IEEE Industry Applications Conference. Thirty-Fifth IAS Annual Meeting and World Conference on Industrial Applications of Electrical Energy*, vol. 1, 2000, pp. 509–514.

[115] T. M. Jahns and V. Caliskan, "Uncontrolled generator operation of interior PM synchronous machines following high-speed inverter shutdown", *IEEE Transactions on Industry Applications*, vol. 35, no. 6, pp. 1347–1357, 1999.

[116] D. A. Staton, T. J. E. Miller, and S. E. Wood, "Maximising the saliency ratio of the synchronous reluctance motor", *IEE Proceedings B - Electric Power Applications*, vol. 140, no. 4, pp. 249–259, 1993.

[117] A. Fratta, A. Vagati, and F. Villata, "On the evolution of AC machines for spindle drive applications", in *Conference Record of the IEEE Industry Applications Society Annual Meeting*, vol. 1, 1989, pp. 699–704.

REFERENCES

[118] W. L. Soong, D. A. Staton, and T. J. E. Miller, "Design of a new axially-laminated interior permanent magnet motor", *IEEE Transactions on Industry Applications*, vol. 31, no. 2, pp. 358–367, 1995.

[119] J. H. Lee and D. S. Hyun, "Hysteresis analysis for the permanent magnet assisted synchronous reluctance motor by coupled FEM and preisach modelling", *IEEE Transactions on Magnetics*, vol. 35, no. 3, pp. 1203–1206, 1999.

[120] N. Bianchi and S. Bolognani, "Interior PM synchronous motor for high performance applications", in *Proceedings of the Power Conversion Conference-Osaka 2002*, vol. 1, 2002, pp. 148–153.

[121] S. E. Sibande, M. J. Kamper, R. Wang, and E. T. Rakgati, "Optimal design of a PM-assisted rotor of a 110 kW reluctance synchronous machine", in *2004 IEEE Africon. 7th Africon Conference in Africa*, vol. 2, 2004, pp. 793–797.

[122] J. Shen, S. Cai, H. Shao, and H. Hao, "Evaluation of low-cost high-performance synchronous motors for ventilation application", in *2015 International Conference on Sustainable Mobility Applications, Renewables and Technology (SMART)*, 2015, pp. 1–6.

[123] I. Boldea, L. N. Tutelea, L. Parsa, and D. Dorrell, "Automotive electric propulsion systems with reduced or no permanent magnets: An overview", *IEEE Transactions on Industrial Electronics*, vol. 61, no. 10, pp. 5696–5711, 2014.

[124] M. Obata, M. Shigeo, M. Sanada, and Y. Inoue, "High-performance PMASynRM with ferrite magnet for EV/HEV applications", in *2013 15th European Conference on Power Electronics and Applications (EPE)*, 2013, pp. 1–9.

[125] P. Guglielmi, G. Giraudo, G. M. Pellegrino, and A. Vagati, "P.M. assisted synchronous reluctance drive for minimal hybrid application", in *Conference Record of the 2004 IEEE Industry Applications Conference, 2004. 39th IAS Annual Meeting*, vol. 1, 2004, p. 306.

[126] C. Lu, S. Ferrari, and G. Pellegrino, "Two design procedures for PM synchronous machines for electric powertrains", *IEEE Transactions on Transportation Electrification*, vol. 3, no. 1, pp. 98–107, 2017.

[127] M. Ferrari, N. Bianchi, and E. Fornasiero, "Analysis of rotor saturation in synchronous reluctance and PM-assisted reluctance motors", *IEEE Transactions on Industry Applications*, vol. 51, no. 1, pp. 169–177, 2015.

[128] N. Bianchi, E. Fornasiero, M. Ferrari, and M. Castiello, "Experimental comparison of PM-assisted synchronous reluctance motors", *IEEE Transactions on Industry Applications*, vol. 52, no. 1, pp. 163–171, 2016.

[129] T. A. Huynh and M. Hsieh, "Comparative study of PM-assisted SynRM and IPMSM on constant power speed range for EV applications", *IEEE Transactions on Magnetics*, vol. 53, no. 11, pp. 1–6, 2017.

[130] H. Cai, B. Guan, and L. Xu, "Low-cost ferrite PM-assisted synchronous reluctance machine for electric vehicles", *IEEE Transactions on Industrial Electronics*, vol. 61, no. 10, pp. 5741–5748, 2014.

[131] W. L. Soong and N. Ertugrul, "Field-weakening performance of interior permanent-magnet motors", *IEEE Transactions on Industry Applications*, vol. 38, no. 5, pp. 1251–1258, 2002.

[132] D. Ngo, M. Hsieh, and T. A. Huynh, "Torque enhancement for a novel flux intensifying PMa-SynRM using surface-inset permanent magnet", *IEEE Transactions on Magnetics*, vol. 55, no. 7, pp. 1–8, 2019.

[133] F. Xing, W. Zhao, and B. Kwon, "Design and optimisation of a novel asymmetric rotor structure for a PM-assisted synchronous reluctance machine", *IET Electric Power Applications*, vol. 13, no. 5, pp. 573–580, 2019.

[134] W. Zhao, F. Xing, X. Wang, T. A. Lipo, and B. Kwon, "Design and analysis of a novel PM-assisted synchronous reluctance machine with axially integrated magnets by the finite-element method", *IEEE Transactions on Magnetics*, vol. 53, no. 6, pp. 1–4, 2017.

[135] N. Bianchi and H. Mahmoud, "An analytical approach to design the PM in PMAREL motors robust toward the demagnetization", *IEEE Transactions on Energy Conversion*, vol. 31, no. 2, pp. 800–809, 2016.

[136] N. Bianchi, H. Mahmoud, and S. Bolognani, "Fast synthesis of permanent magnet assisted synchronous reluctance motors", *IET Electric Power Applications*, vol. 10, no. 5, pp. 312–318, 2016.

[137] H. Huang, Y. Hu, Y. Xiao, and H. Lyu, "Research of parameters and antidemagnetization of rare-earth-less permanent magnet-assisted synchronous reluctance motor", *IEEE Transactions on Magnetics*, vol. 51, no. 11, pp. 1–4, 2015.

[138] N. Bianchi, S. Bolognani, D. Bon, and M. Dai Pre, "Rotor flux-barrier design for torque ripple reduction in synchronous reluctance and PM-assisted synchronous reluctance motors", *IEEE Transactions on Industry Applications*, vol. 45, no. 3, pp. 921–928, 2009.

[139] P. Alotto, M. Barcaro, N. Bianchi, and M. Guarnieri, "Optimization of interior PM motors with machaon rotor flux barriers", *IEEE Transactions on Magnetics*, vol. 47, no. 5, pp. 958–961, 2011.

[140] S. S. R. Bonthu, A. Arafat, and S. Choi, "Comparisons of rare-earth and rare-earth-free external rotor permanent magnet assisted synchronous reluctance motors", *IEEE Transactions on Industrial Electronics*, vol. 64, no. 12, pp. 9729–9738, 2017.

REFERENCES

[141] Y. Wang, D. M. Ionel, M. Jiang, and S. J. Stretz, "Establishing the relative merits of synchronous reluctance and PM-assisted technology through systematic design optimization", *IEEE Transactions on Industry Applications*, vol. 52, no. 4, pp. 2971–2978, 2016.

[142] M. Degano, E. Carraro, and N. Bianchi, "Selection criteria and robust optimization of a traction PM-assisted synchronous reluctance motor", *IEEE Transactions on Industry Applications*, vol. 51, no. 6, pp. 4383–4391, 2015.

[143] E. Carraro, M. Morandin, and N. Bianchi, "Traction PMASR motor optimization according to a given driving cycle", *IEEE Transactions on Industry Applications*, vol. 52, no. 1, pp. 209–216, 2016.

[144] N. Bianchi, M. Degano, and E. Fornasiero, "Sensitivity analysis of torque ripple reduction of synchronous reluctance and interior PM motors", *IEEE Transactions on Industry Applications*, vol. 51, no. 1, pp. 187–195, 2015.

[145] M. Barcaro and N. Bianchi, "Torque ripple reduction in fractional-slot interior PM machines optimizing the flux-barrier geometries", in *2012 XXth International Conference on Electrical Machines*, 2012, pp. 1496–1502.

[146] N. Bianchi, S. Bolognani, D. Bon, and M. D. PrÉ, "Torque harmonic compensation in a synchronous reluctance motor", *IEEE Transactions on Energy Conversion*, vol. 23, no. 2, pp. 466–473, 2008.

[147] T. Tokuda, M. Sanada, and S. Morimoto, "Influence of rotor structure on performance of permanent magnet assisted synchronous reluctance motor", in *2009 International Conference on Electrical Machines and Systems*, 2009, pp. 1–6.

[148] M. Gamba, G. Pellegrino, and A. Vagati, "A new PM-assisted synchronous reluctance machine with a nonconventional fractional slot per pole combination", in *2014 International Conference on Optimization of Electrical and Electronic Equipment (OPTIM)*, 2014, pp. 268–275.

[149] X. Chen, J. Wang, P. Lazari, and L. Chen, "Permanent magnet assisted synchronous reluctance machine with fractional-slot winding configurations", in *2013 International Electric Machines Drives Conference*, 2013, pp. 374–381.

[150] N. Bianchi, E. Fornasiero, and W. Soong, "Selection of PM flux linkage for maximum low-speed torque rating in a PM-assisted synchronous reluctance machine", *IEEE Transactions on Industry Applications*, vol. 51, no. 5, pp. 3600–3608, 2015.

[151] G. Pellegrino, A. Vagati, and P. Guglielmi, "Design tradeoffs between constant power speed range, uncontrolled generator operation, and rated current of IPM motor drives", *IEEE Transactions on Industry Applications*, vol. 47, no. 5, pp. 1995–2003, 2011.

[152] S. Nategh, "Thermal analysis and management of high-performance electrical machines", Ph.D. dissertation, KTH Royal Institute of Technology, 2013.

[153] P. Niazi and H. A. Toliyat, "Robust maximum torque per amp (MTPA) control of PM-assisted synchronous reluctance motor", in *Twenty-First Annual IEEE Applied Power Electronics Conference and Exposition, 2006. APEC '06*, 2006, pp. 685–692.

[154] B. Boazzo and G. Pellegrino, "Model-based direct flux vector control of permanent-magnet synchronous motor drives", *IEEE Transactions on Industry Applications*, vol. 51, no. 4, pp. 3126–3136, 2015.

[155] A. K. Chakali, "Sensorless speed control of permanent magnet-assisted synchronous reluctance motor (PMa-SynRM)", M.S. thesis, Texas A & M University, 2011.

[156] I. Boldea, C. I. Pitic, C. Lascu, G. Andreescu, L. Tutelea, F. Blaabjerg, and P. Sandholdt, "DTFC-SVM motion-sensorless control of a PM-assisted reluctance synchronous machine as starter-alternator for hybrid electric vehicles", *IEEE Transactions on Power Electronics*, vol. 21, no. 3, pp. 711–719, 2006.

[157] P. Guglielmi, M. Pastorelli, and A. Vagati, "Cross-saturation effects in IPM motors and related impact on sensorless control", *IEEE Transactions on Industry Applications*, vol. 42, no. 6, pp. 1516–1522, 2006.

[158] S. Zhao, "Analysis and control aspects of a PMSynRel drive in a hybrid electric vehicle application", Ph.D. dissertation, KTH Royal Institute of Technology, 2013.

[159] Z. Zhang, "Analysis of a rare earth-free dual mechanical port machine with PM-assisted reluctance rotor for hybrid electric vehicles", in *2019 IEEE International Electric Machines Drives Conference (IEMDC)*, 2019, pp. 965–969.

[160] B. Wang, J. Wang, A. Griffo, and B. Sen, "Experimental assessments of a triple redundant nine-phase fault-tolerant PMA SynRM drive", *IEEE Transactions on Industrial Electronics*, vol. 66, no. 1, pp. 772–783, 2019.

[161] S. S. R. Bonthu, "Optimal design and comparative analysis of multi-phase permanent magnet assisted synchronous reluctance machines", M.S. thesis, University of Akron, 2015.

[162] Ansys, Inc., *Ansys Electronics online help*, `https://ansyshelp.ansys.com/account/secured?returnurl=/Views/Secured/Electronics/v181/home.htm%23`, 2020.

[163] E. Bilgen and R. Boulos, "Functional dependence of torque coefficient of coaxial cylinders on gap width and reynolds numbers", *Journal of Fluids Engineering, ASME*, vol. 95, no. 1, pp. 122–126, 1973.

REFERENCES

[164] D. Bernhardt and J. F. Reilley II, *Mineral commodity summaries 2020*, `https://pubs.usgs.gov/periodicals/mcs2020/mcs2020.pdf`, U.S. Geological Survey, 2020.

[165] Asian Metal, *Prices of stainless and special*, `http://www.asianmetal.com/price/initPriceListEn.am?priceFlag=13&isProduct=null`, 2020.

[166] FIRST4MAGNETS, *Prices of ferrite rectangular magnets*, `https://www.first4magnets.com/rectangular-c35/ferrite-magnets-t138`, 2020.

[167] Asian Metal, *Prices of base metals*, `http://www.asianmetal.com/price/initPriceListEn.am?priceFlag=4&isProduct=null`, 2020.

[168] X. Jannot, J. Vannier, C. Marchand, M. Gabsi, J. Saint-Michel, and D. Sadarnac, "Multiphysic modeling of a high-speed interior permanent-magnet synchronous machine for a multiobjective optimal design", *IEEE Transactions on Energy Conversion*, vol. 26, no. 2, pp. 457–467, 2011.

[169] C. Boccaletti, S. Elia, and E. Nistico, "Deterministic and stochastic optimisation algorithms in conventional design of axial flux PM machines", in *International Symposium on Power Electronics, Electrical Drives, Automation and Motion, 2006. SPEEDAM 2006*, 2006, pp. 111–115.

[170] Y. Duan and D. M. Ionel, "A review of recent developments in electrical machine design optimization methods with a permanent-magnet synchronous motor benchmark study", *IEEE Transactions on Industry Applications*, vol. 49, no. 3, pp. 1268–1275, 2013.

[171] R. W. Lewis, V. Torczon, and M. W. Trosset, "Direct search methods: Then and now", *Journal of computational and Applied Mathematics*, vol. 124, no. 1-2, p. 2000, 2000.

[172] R. Wrobel and P. H. Mellor, "The use of a genetic algorithm in the design optimisation of a brushless DC permanent magnet machine rotor", in *Second International Conference on Power Electronics, Machines and Drives (PEMD 2004)*, vol. 2, 2004, pp. 823–827.

[173] T. Nakata, M. Sanada, S. Morimoto, and Y. Inoue, "Automatic design of IPMSMs using a genetic algorithm combined with the coarse-mesh FEM for enlarging the high-efficiency operation area", *IEEE Transactions on Industrial Electronics*, vol. 64, no. 12, pp. 9721–9728, 2017.

[174] J. B. Kim, K. Y. Hwang, and B. I. Kwon, "Optimization of two-phase in-wheel IPMSM for wide speed range by using the kriging model based on latin hypercube sampling", *IEEE Transactions on Magnetics*, vol. 47, no. 5, pp. 1078–1081, 2011.

[175] A. Mahmoudi, S. Kahourzade, N. A. Rahim, and W. P. Hew, "Design, analysis, and prototyping of an axial-flux permanent magnet motor based on genetic algorithm and finite-element analysis", *IEEE Transactions on Magnetics*, vol. 49, no. 4, pp. 1479–1492, 2013.

[176] S. Singer and J. Nelder, "Nelder-mead algorithm", *Scholarpedia*, vol. 4, no. 7, p. 2928, 2009.

[177] J. A. Nelder and R. Mead, "A simplex method for function minimization", *The computer journal*, vol. 7, no. 4, pp. 308–313, 1965.

[178] Gemmel Metalle, *Legierungsbeschreibung AlZnMgCu1,5*, `https://www.gemmel-metalle.de/aluminium/rund/7075/1.html`, 2020.

[179] Bunting Magnetics Europe, *Ferrite/ceramic data sheet*, `https://www.buntingeurope.com/wp-content/uploads/2018/07/BME_Ferrite_Ceramic_data_sheet.pdf`, 2018.

[180] OVAKO, *Datasheet of S235JR*, `https://steelnavigator.ovako.com/steel-grades/s235/`, 2020.

[181] Cogent, *Typical data for SURA®M270-35A*, `https://www.tatasteeleurope.com/ts/sites/default/files/m270-35a_1.pdf`, 2021.

[182] isovac, *Datasheet of isovac 270-35 a*, `https://www.voestalpine.com/stahl/content/download/4576/file/voestalpine_datasheet_isovac_270-35A_EN_20180601.pdf?inLanguage=eng-GB`, 2018.

[183] N. Nishiyama, H. Uemura, and Y. Honda, "Highly demagnetization performance IPMSM under hot environments", *IEEE Transactions on Industry Applications*, vol. 55, no. 1, pp. 265–272, 2019.

[184] A. M. EL-Refaie, "Fractional-slot concentrated-windings synchronous permanent magnet machines: Opportunities and challenges", *IEEE Transactions on Industrial Electronics*, vol. 57, no. 1, pp. 107–121, 2010.

[185] D. Ishak, Z. Q. Zhu, and D. Howe, "Comparison of PM brushless motors, having either all teeth or alternate teeth wound", *IEEE Transactions on Energy Conversion*, vol. 21, no. 1, pp. 95–103, 2006.

[186] D. Staton, A. Boglietti, and A. Cavagnino, "Solving the more difficult aspects of electric motor thermal analysis in small and medium size industrial induction motors", *IEEE Transactions on Energy Conversion*, vol. 20, no. 3, pp. 620–628, 2005.

[187] K. M. Becker and J. Kaye, "Measurement of a diabatic flow in an annulus with an inner rotating cylinder", *Journal of Heat Transfer*, vol. 84, no. 2, pp. 97–104, 1962.

REFERENCES

[188] M. Centner, "Entwurf und erprobung schnelldrehender asynchronmaschinen unter besonderer berücksichtigung der magnetisch aktiven materialien", Ph.D. dissertation, Technische Universität Berlin, 2009.

[189] Hitachi Metals, Ltd., *High-performance ferrite magnet NMF series*, `http://www.hitachi-metals.co.jp/e/products/auto/el/pdf/nmf_a.pdf`, 2020.

[190] A. Vagati, B. Boazzo, P. Guglielmi, and G. Pellegrino, "Design of ferrite-assisted synchronous reluctance machines robust toward demagnetization", *IEEE Transactions on Industry Applications*, vol. 50, no. 3, pp. 1768–1779, 2014.

[191] Infineon Technologies, *Angle sensor TLE5009 data sheet, rev. 1.1*, `https://www.infineon.com/dgdl/Infineon-TLE5009_FDS-DataSheet-v01_01-en.pdf?fileId=db3a304330f686060131421d8ddd56b0`, 2012.